Mechanisms for Kink Band Evolution in Polymer Matrix Composites:

A Digital Image Correlation and Finite Element Study

by

Jay Patel

A Dissertation Presented in Partial Fulfillment
of the Requirements for the Degree
Doctor of Philosophy

Approved April 2016 by the
Graduate Supervisory Committee:

Pedro Peralta, Chair
Jay Oswald
Hanqing Jiang
Kiran Solanki
Adarsh Ayyar

ARIZONA STATE UNIVERSITY

May 2016

ABSTRACT

Polymer matrix composites (PMCs) are attractive structural materials due to their high stiffness to low weight ratio. However, unidirectional PMCs have low shear strength and failure can occur along kink bands that develop on compression due to plastic microbuckling that carry strains large enough to induce nonlinear matrix deformation. Reviewing the literature, a large fraction of the existing work is for uniaxial compression, and the effects of stress gradients, such as those present during bending, have not been as well explored, and these effects are bound to make difference in terms of kink band nucleation and growth. Furthermore, reports on experimental measurements of strain fields leading to and developing inside these bands in the presence of stress gradients are also scarce and need to be addressed to gain a full understanding of their behavior when UDCs are used under bending and other spatially complex stress states.

In a light to bridge the aforementioned gaps, the primary focus of this work is to understand mechanisms for kink band evolution under an influence of stress-gradients induced during bending. Digital image correlation (DIC) is used to measure strains inside and around the kink bands during 3-point bending of samples with 0°/90° stacking made of Ultra-High Molecular Weight Polyethylene Fibers. Measurements indicate bands nucleate at the compression side and propagate into the sample carrying a mixture of large shear and normal strains (~33%), while also decreasing its bending stiffness. Failure was produced by a combination of plastic microbuckling and axial splitting. The microstructure of the kink bands was studied and used in a microstructurally explicit finite element model (FEM) to analyze stresses and strains at ply level in the samples during

kink band evolution, using cohesive zone elements to represent the interfaces between plies. Cohesive element properties were deduced by a combination of delamination, fracture and three-point bending tests used to calibrate the FEMs. Modeling results show that the band morphology is sensitive to the shear and opening properties of the interfaces between the plies.

ACKNOWLEDGMENTS

I would like to take this opportunity to express my gratitude towards my research advisor, Dr. Pedro Peralta, for his continuous support in answering all my questions and guiding me in right direction. In addition to his educational advising, I was also taught the principles of the life. I genuinely do not have enough words to express my feelings for him. Special thanks to my coworkers Vipin Vijaykumaran, Andrew Brown, Harn Lim, Karin Rudman and Robert McDonald for their support. I would also like to thank my parents and most importantly, my wife Dharitri for giving me courage to meet my goals.

I would also like to thank BAE systems for their support providing composite samples for my research.

A special thanks to Athletics Research Grant (ARG), operated by the GPSA at ASU, for providing grant for terminal research to carry out finite element simulations.

My heartiest thanks to SEMTE for continuously supporting me through teaching assistantships for all these years!

TABLE OF CONTENTS

Page

CHAPTER Page

CHAPTER Page

LIST OF TABLES

LIST OF FIGURES

Figure Page

Figure Page

Figure Page

Figure Page

Figure Page

Figure Page

Figure Page

Figure Page

Figure Page

1. INTRODUCTION

The word composite means consisting of two or more distinct constituent materials or phases. The classification of certain materials as composites often is based on cases where significant property changes occur as a result of the combination of constituents, e.g., fiber and matrix. Composites with long fibers are called continuous–fiber-reinforced composites. The continuous fibers in a "single – layer" composite are aligned in one direction to form a unidirectional (UD) composite [65-67].

Unidirectional composites (UDCs) are fabricated by laying the fibers parallel and saturating them with resinous material such as polyester or epoxy resin, that holds the fibers in position and serves as the matrix material. Such forms of preimpregnated fibers are called pre-pregs. The resulting unidirectional composites are very strong in fiber direction, but generally weak in the direction perpendicular to the fibers. Therefore, unidirectional pre-pregs are stacked together in various orientations to form laminates usable in engineering applications [65, 67].

The continuous reinforcement in a single layer also may be provided in a second direction to achieve more balanced properties. The bidirectional reinforcement may be provided in a single layer in mutually perpendicular directions as in a woven fabric. The bidirectional reinforcement may be such that the strengths in two perpendicular directions are approximately equal. In some applications, a minimum of reinforcement perpendicular to the primary direction is provided only to prevent damage and fiber separation in handling owing to the poor strength in the transverse direction. However, this can be controlled via different manufacturing conditions [65, 67].

Fiber laminated composites, in general, and Polymer Matrix Composites (PMCs), in particular, are attractive materials in defense, aerospace and automobile industry due to their high strength-weight ratio and controlled anisotropy. The controlled anisotropy means that the ratio of property values in different directions can be varied or controlled. For example, in a unidirectional composite, the longitudinal strength-transverse strength ratio can be changed easily by changing fiber volume fraction. Similarly, altering the material and manufacturing variables can alter other properties to use these laminated composites for more specific applications [65-67].

The work presented here has been documented in a total of 6 chapters. Chapter 1 covers an introduction to polymer matrix composites, background and motivation of the current research. Chapter 2 focuses on a literature review on the failure mechanisms in general, and polymer matrix composites in particular. It includes a review of experimental observations of kink band formation under different loading conditions and modeling techniques of kink band and microbuckling. Moreover, it also covers a review of cohesive zone modeling techniques to model Mode I and Mode II inter-laminar fracture.

Chapter 3 discusses experimental and modeling objectives of the current research. Chapter 4 focuses on experimental procedures used to perform three-point bending tests, digital image correlation (DIC) measurements, as well as and Mode I and Mode II inter-laminar fracture tests. In addition to experimental procedures, the chapter also sheds light on modeling techniques to capture microbuckling and kink band formation, in addition to cohesive zone modeling (CZM) of Mode I and Mode II inter-laminar fracture tests. Chapter 5 covers results of this research, discussing all topics (experimental and numerical

simulations) outlined in chapter 4. Finally, chapter 6 has concluding remarks for the entire research and possible future work.

The investigation in this research is focused on two PMCs.

1. Dyneema HB80 – Trademark of DSM Dyneema, NL.
2. Spectra Shield – Trademark of Honeywell, Inc.

The above-mentioned composites are made of ultra-high molecular weight polyethylene (UHMWPE) fibers, 83% by volume and polyurethane (PU) matrix, 17 % by volume. The combination of these constituents is exploited to achieve superior impact resistance and hence they are used mainly in personal armor application like bulletproof vests and helmets [65].

The manufacturing steps employed by DSM to make composites with the [0°/90°] stacking layup and a polyurethane matrix, were detailed in Russell et al. [50]. These steps are applicable to most of the [0°/90°] grades.

Similar constituents have been used to construct Spectra Shield laminates (the details are proprietary to Honeywell) with different processing/manufacturing conditions. The matrix may be strong or weak as compared to Dyneema HB80. This requires justification through interlaminar fracture tests, which is a part of one of the experimental objectives of the current research. Results obtain here show clear distinction between the two laminates in terms of ply thickness, cross-section of fibers and their arrangement, which will be discussed in later sections of this report.

The use of PMCs in demanding and critical applications in aerospace and defense industries makes it essential to understand their complex failure mechanisms under compression and bending. Many of these materials have been used as compression carrying members and most of the members are usually beams and plates, which are slender. Many researchers have studied the failure mechanisms since 1960 as indicated in references [1-5, 8, 11-17, 20, 22, 24, 25, 28, 34, 35], leading to a significant body of work by the research community that has provided significant insight into the complex physics behind PMC behavior. These materials have low shear strength and deformation is localized under this load, leading to a shear instability that occurs at sufficiently large strains for the matrix to deform non-linearly. This phenomenon has been reported abundantly in the open literature [3-5, 14, 15] and has been recognized as a form of plastic microbuckling. The deformation is localized in a kink band within which fibers have large amount of rotation and the matrix undergoes large shear deformation. This makes plastic microbuckling a key strength-limiting factor in modern polymer matrix composites.

Unidirectional composites under compression exhibit similar behavior to that described above. However, these composites have a distinct behavior in bending as compared to pure uniaxial compression [68, 69]. The driving mechanism of plastic microbuckling under bending is different than under pure compression, since there is a stress gradient under bending. It is known that the compressive strength of the composites changes under the presence of stress-gradients [46, 68, 69]. The present study is to focus on mechanisms for kink band evolution under stress-gradients, through the use of 3-point bending experiments and simulations. Under bending, a kink band propagates through the

material's thickness from the compression to the tension side of the beam and induces large stresses (combination of axial compression and shear) far beyond the elastic limit, resulting in plasticity [6, 28]. The kink band development is a complicated phenomenon that is governed by factors such as fiber failure, matrix failure, fiber-matrix interfacial strength, microstructure and geometric imperfections during manufacturing on a microscopic scale.

The study of plastic kinking, particularly the quantification of the large strains present in the kink bands, from nucleation to final failure becomes extremely important as it can provide better insight into the state of stress that triggers kink bands, and, in turn, can also lead to strategies on how to improve a material's capacity to withstand high bending and compressive loads. Furthermore, the study of buckling of elastic-plastic and elastic-visco-plastic materials with finite strains at a length scale commensurate with a kink band and the effect of local microstructure on this phenomenon is of paramount importance to develop reliable computational models that account for the statistical nature of PMC failure, particularly when it is triggered by a kink band.

Most of the research to date has focused on studying failure mechanisms under compression, developing equations to predict compressive strength, determination of kink band angle, studying the effect of the geometric imperfection that triggers one or more damage mechanisms [4-8, 12-16, 24-26, 28]. Moreover, many of these issues were studied and observed through experimental techniques as well. Wisnom [46, 68, 69] studied size effects in fiber-composites under bending in addition to the effect of fiber waviness on relationship between compressive and flexure strengths of UDCs. It was observed that

compressive failure in bending is believed to be mainly due to the stress gradient through the thickness. But, unfortunately, the work did not explore in detail specific damage mechanisms and how they relate to kink band evolution under the presence of stress-gradients, particularly in terms and how kink bands propagate through the plies and how this leads to failure via delamination.

Moreover, the experimental work and simulations done by Liu et al. [27, 63] on collapse of UHMWPE composites under bending does not shed light on morphology of kink band during its evolution under stress gradients. The primary focus of Liu's work [27] was to identify the collapse mode for short and long beams under cantilever configuration. But, unfortunately, the study did not cover any quantitative analysis of how the developed wedge shaped kink band led to delamination failure in long beams, since there was a lot of constraint near the built- in end. This constraint does affect the nucleation and evolution of the kink band during the test in cantilever configuration. Testing under stress gradients with lower constraints, such as those present during 3-point bending, would provide a simpler stress condition, which, in turn, would facilitate both experimental characterization and modeling of kink band nucleation and evolution, as well as the mechanisms of damage initiation at these kink bands.

In addition to the aforementioned limitation, there is another gap of knowledge identified in [27]. During the bending test performed on long beams, the load-displacement profile (figure 11a in chapter 2, literature review) showed some load oscillations with increasing displacement. However, there is no explanation offered in [27] for these load oscillations during kink band evolution.

The extended work of Liu [63] identified the sensitivity of microbuckling response to overall effective shear modulus and interlaminar shear strength of long composite beams. However, the study did not emphasize on the sensitivity of kink band morphology in particular; addressing width of the kink band, band inclination angle and band rotation angle.

In summary, there is a gap of knowledge in elucidating kink band characteristics during its evolution. This can be bridged, experimentally, by using high-resolution DIC, which can facilitate the quantitative assessment of the evolution of displacement and strain fields inside the kink band in the presence of stress-gradients. Moreover, the combination of experimental results with quantitative analysis from finite element simulations can give additional insight into the damage mechanisms of individual plies during bending tests, as driven by plastic microbuckling. A parametric study can also be performed through simulations that can also elucidate how key material and geometric parameters influence the mechanical response and kink band morphology in fiber-reinforced UDCs.

2. LITERATURE REVIEW

The most frequently considered failure modes in unidirectional laminates are microbuckling, kinking, fiber failure and longitudinal cracking (synonymous with delamination failure in general laminates) [3, 4, 14]. Obviously, these failure modes may combine in any one specimen, or a given mode may dominate for the same composite material tested under different conditions.

It is established that the compressive strength of PMC's is generally lower than the tensile strength [4]; this relative weakness in compression is often the limiting factor in the application of composite materials. In order to design a composite structure to operate efficiently and safely under compressive loading, it is necessary to predict accurately the compressive strength of that structure, taking into account the possible failure modes of the structure under different conditions. A significant number of previous experimental results have revealed that material failure (usually at the microstructural level) such as fiber microbuckling or kinking in lamina where the fibers are aligned with the loading axis are the initiating mechanisms of compressive failure that lead to global instability in composite structures, e.g., see the work by Sohi [1], and Soutis [2].

The reviews by Waas and Schultheisz [3] and Fleck [4] examined the issues related to compressive failure rather exhaustively. The papers by Budiansky and Fleck [5] and Kyriakides et al. [8] provide a thorough treatment of plastic microbuckling and the initiation and localization of deformation into kink bands, respectively. Sun and Jun [6], who used a lamina level plasticity formulation and Schapery [7] who examines time dependent microbuckling failure have also contributed to the topic. In addition, Shu and

Fleck [4] have used a couple stress theory to examine microbuckling, while the effects of other plies on the zero ply microbuckling strength of laminates have been examined by Swanson [9] and Drapier et al. [10]. Narayan and Schadler [11], proposed a new mechanism for the initiation of kink banding based on experiments with unidirectional composites in conjunction with Raman spectroscopy. They propose a model based on the development of a distributed damage zone due to fiber end effects.

Microbuckling has also been observed in carbon-carbon composites by Evans and Adler [12] and Chatterjee and McLaughlin [13]. They showed plastic microbuckling as an operative mechanism in unidirectional composites. Plastic microbuckling leads to kink band formation.

Wisnom [46, 68, and 69] studied the size effects of fiber-composites under bending in addition to the effect of fiber waviness on relationship between compressive and flexure strengths of UDCs. It was observed that compressive failure in bending is believed to be mainly due to the stress gradient through the thickness and the effect is more pronounced in thin beams as compared to thick beams. Finite element modelling studies have shown that in bending, the surface fibers are supported against buckling by the less highly loaded adjacent fibers [68]. The compressive stress at which instability occurs is therefore higher in bending than in compression, and increases as the thickness decreases. This also explains the tendency of flexural failures to switch from tension to compression as the specimen size increases [70], because the constraint due to the stress gradient decreases as the specimen becomes thicker. Similar effects have been predicted in other studies [71] and [72]. An effect of stress gradient on compressive failure has also been

found experimentally in pin-ended buckling tests on specimens of the same thickness with different ratios of compressive to bending stress [69].

But, unfortunately, the aforementioned work did not explore in detail about the specific damage mechanisms and how they relate to kink band evolution under the presence of stress-gradients, particularly in terms and how kink bands propagate through the plies and how this leads to failure via delamination. Therefore, it is important to understand the details of kink band nucleation and evolution up to the overall failure of composite under bending, as this is an important loading mode for composites used in practical applications where stress-gradients can play an important role.

2.1 Failure Mechanisms in Unidirectional Composites Under Compression

Various failure mechanisms of unidirectional composites under compression have been reported in the literature, e.g., work by Fleck [4], Waas and Schultheisz [3] and Argon [14], among others. These failure mechanisms include elastic microbuckling, plastic microbuckling, fiber crushing, matrix cracking, longitudinal splitting, and shear band formation. Many of these mechanisms are shown in figure 1 [4], and can be briefly described as follows:

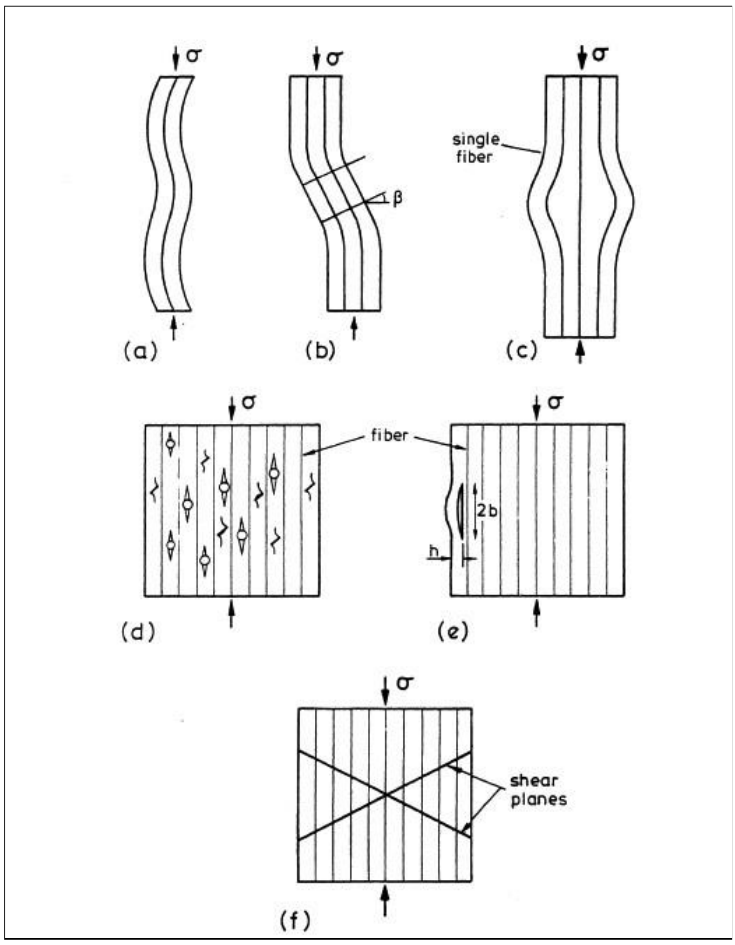

Figure 1. The Main Competing Failure Modes in UDCs – (a) Elastic Microbuckling, (b) Plastic Microbuckling, (c) Fiber Crushing, (d) Matrix Splitting, (e) Buckle Delamination of a Surface Layer, (f) Shear Band Formation, After [4].

(a) Elastic microbuckling: This is a shear buckling instability in which the matrix deforms in simple shear.

(b) Plastic microbuckling: This is a shear buckling instability; which occurs at sufficient amount of large strains for the matrix to deform in a non-linear manner. This is the most common deformation/failure mode in polymer matrix composites that induces kink band within the plies.

(c) Fiber crushing: It occurs at the fiber level due to the buckling (shear instability) within the fiber. It is mostly associated with the wavy fibers embedded in a soft matrix.

(d) Matrix Splitting: This occurs due to low toughness of the matrix; the matrix cracks parallel to the main axial fiber direction.

(e) Buckle delamination: This phenomenon is common in ceramic and polymer matrix composites and described as a buckling debonding between the surface layer and a sub-surface. The large sub-surface flaw and the low matrix toughness cause the buckle delamination.

(f) Shear Band: This occurs due to matrix yielding and fracture occurs in a band oriented at about 45° with respect to the loading axis as shown in figure.

2.2 Analytical Models of Plastic Microbuckling

Among all the aforementioned failure modes, plastic microbuckling is an area of focus for this work. Researchers have addressed the plastic microbuckling phenomenon as a dominant deformation/failure mechanism under compression; which is controlled by fiber misalignment along with plastic shear deformation in the matrix [4, 5].

Rosen [15] initiated the study of predicting compressive strength in fiber-reinforced composites by introducing the microbuckling phenomenon. His hypothesis was that, under compression, the individual fibers buckle in a short wave length pattern in a fashion analogous to the buckling of a column or a plate on an elastic foundation. The assumptions were based on two primary modes of buckling stated as follows:

• Extension Mode: Fibers buckle in opposite directions in adjacent fibers and so called the extension mode as shown in figure 2. In this model, the major deformation of the matrix occurs in the direction perpendicular to the fibers. This has been observed in PMCs with low fiber volume fraction.

• Shear Mode: In this case, fibers buckle in the same wavelength and in phase with one another such that the deformation of the matrix material between the adjacent fibers deforms under shear stresses. Figure 2 shows the schematic diagram of a shear mode. This mode is common in PMCs with high fiber volume fraction. (V_f>0.6). The shear-buckling mode was proved as a potential deformation and failure mode [4], [5], [14] in fiber-reinforced composites with high fiber volume fraction, which is a part of this study. The compressive strength was predicted by the following equation.

$$\sigma_c = \frac{G}{(1-v_f)} \tag{2.1}$$

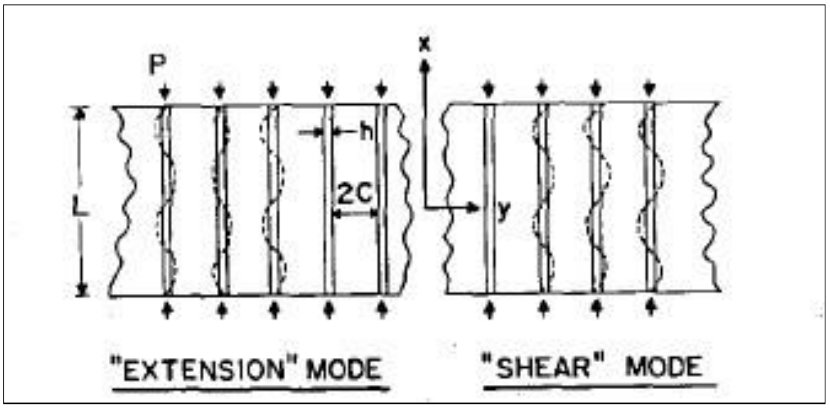

Figure 2. Rosen's Models for Two Different Types of Microbuckling that can Affect Compressive Strength in Fibrous Composites [15].

In equation (2.1), *G* is the shear modulus of the matrix and v_f stands for the fiber volume fraction [15]. Jelf and Fleck [16] tested Rosen's theoretical model by doing

experiments on composites to validate equation (2.1). They concluded that Rosen's model is only valid for elastic microbuckling in which the matrix deforms in simple shear. Using Rosen's work as a foundation, Argon [14] and Budiansky [5] extended the microbuckling theory by identifying the shear yield strength of the matrix (you need to show the symbol for this parameter here) and the initial fiber misalignment angle Φ_0 of the fibers as the main controlling parameters, and developing equations to predict compressive strength of the composites. Their analysis neglected bending of the fibers and assumed that the fibers within a finite width band *w* had an initial misalignment angle Φ_0. The unit normal to the band was rotated through a kink band inclination angle β as shown in figure 3.

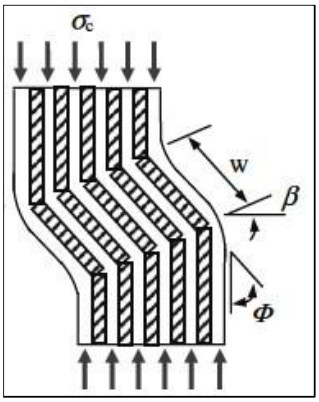

Figure 3. Plastic Kinking of a Band of w Width, Fiber Rotation Angle Φ (α) and Inclined at Angle β with a Remote Fiber Along the Vertical Direction [14].

Argon [14] approximated the kinking stress as a function of shear strength τ and initial fiber misalignment angle Φ_0 within a band inclination angle β=0 as follows:

$$\sigma_c = \frac{\tau}{\Phi_0} \tag{2.2}$$

Argon [14] argued that the critical compressive stress triggers the additional fiber rotation angle Φ (also commonly labeled α) within the band. He also showed that the compressive/kinking stress is reduced with additional fiber rotation angle in accordance with the following equation.

$$\sigma_c = \frac{\tau}{\Phi_0 + \Phi} \tag{2.3}$$

Budiansky [5] extended Argon's work by adding the yield strain of matrix Υ_y as a parameter to an elastic-perfectly plastic composite, as follows:

$$\sigma_c = \frac{\tau}{\Phi_0 + \gamma_Y} = \frac{G}{1 + {\Phi_0}/{\gamma_Y}} \tag{2.4}$$

Equation (2.4) is valid for both Argon's and Rosen's models with their respective inputs even with large initial fiber misalignment angle Φ_0. Many researchers validated the above equation by doing several experiments on different type of composites. It is clear from equation (2.4) that the ratio of $\Phi_0/\Upsilon_y = 0$ predicts the elastic kinking stress (ideal case of Rosen's work). Using experimental data, Chaplin [17], Hahn et al [24], Jelf [16] and Soutis [2] confirmed that Rosen analysis over predicts strength typically by a factor of four. This supports the hypothesis of microbuckling as a plastic event rather than an elastic one. In other words, the ratio of Φ_0/Υ_y in equation (2.4) was found to be greater than zero and dominates the manifestation of plastic microbuckling vs. elastic microbuckling. Some of the experimental results also show the effect of initial fiber misalignment on a composite's compressive strength. Wilkinson et al. [18] found that the compressive strength of T300/914 carbon epoxy cloth (G=6 GPa) reduced from 1 GPa to 200 MPa by inserting brass wires into the cloth normal to the fiber direction to increase the waviness.

Hahn and Williams [24] predicted buckling (instability) strength in composites by considering single fiber buckling as a function of fiber volume fraction, the composite's shear modulus, Young's moduli of the fiber and the matrix, geometric imperfection parameters and the shear strain at the critical stress. The correlation between the analytical solution and experimental results was good especially for composites with a stiff matrix.

Steif's [19] model considers an imperfect (sinusoidal) fiber under bending, with finite deflections and large fiber rotations (α=Φ); the equation governing the problem is deduced from equilibrium of moments, considering the action of the compressive load, the bending moments and the shear stresses transferred by the matrix. It assumes an in-phase shear deformation during the kink band formation. The response is linear for small angles and it is perfectly plastic under large rotations. The corresponding equation for the shear stress (τ_m) in the matrix is

$$\tau_m = \sigma_m . tanh \frac{G_m . \alpha}{\sigma_m} \tag{2.5}$$

where, σ_m and G_m are bending stress and shear modulus of the matrix respectively.

Dávila et al. [21] proposed a model to predict damage initiation under axial compression based on the assumption of initially misaligned fibers and a shear dominated failure. These authors were able to compute the fiber misalignment for any given two-dimensional (2-D) load combination, and that angle of misalignment would then be used to calculate the stress components in the material's principal directions; once σ_{22} and τ_{12} are known for the matrix in the misaligned material, these stresses can be used as inputs for matrix failure criteria. By assuming that once the matrix fails the fibers lose their

support and break as a consequence, this model separates completely the formation of kink bands from micro-buckling or fiber failure.

Schultheisz and Waas [3] emphasize the importance of taking into account fiber misalignments, matrix non-linear behavior and three-dimensional (3-D) stress states in further development of models of fiber kinking.

Chaplin [17] studied the unique relation between $\Phi=\alpha$ and β in an inclined band of an incompressible material and concluded that the maximum fiber rotation angle $\Phi=\alpha = 2\beta$; however, experimental results do not support this relationship in all cases as α may exceed 2β during evolution of the kink band. The parameters are shown in figure 3.

Budiansky and Fleck [5] derived a relation to predict transverse strains (ε_T) and shear strains (γ) inside the kink band using the band's geometric parameters, which resulted in the following equation:

$$\varepsilon_T = \ln\left[\frac{cos(\beta-\alpha)}{cos\beta}\right] and\ \gamma = \alpha \tag{2.6}$$

Note from this relation that the transverse strain becomes compressive when $\alpha>2\beta$. Generally, the fibers are found to be locked up at $\alpha=2\beta$, as postulated by Moran [20].

2.3 Experimental Studies of Failure

Moran [20] presented and interpreted the results of his experimental work done with thick (6 mm) rectangular IM7/PEEK specimens, previously notched with a 4 mm indentation and loaded in compression under displacement control. According to his interpretation, after an initially linear behavior, the matrix starts yielding around the notch,

producing what was referred to as “incipient kinking.” This occurred just before the peak load was reached and a kink band was suddenly propagated from the notch across the entire specimen's width (10mm). The kink band, at this initial state, was characterized by $w = 10d_f$ (fiber diameter), β = 10° to 15°, and the rotation of the fibers increased slowly to α = 15° to 20° as the compression progressed. At this point, fiber rotation became unstable and it suddenly changed to α = 40° to 45°, followed by an increase of the band's angle (β = 10° to 15°), until the fibers were locked-up by the shear response of the matrix. After this “transient band broadening” phase, corresponding to the increase of α and under a decreasing compressive load, the band starts to become wider at a steady state (broadening) load; in this phase, the width of the kink band increased progressively, as the fibers at the outside border of the band were bent until they failed and aligned themselves with the previously locked-up fibers. After the tests the specimens were observed unloaded and it was found that the elastic recovery was small, leading the author to conclude that the matrix deformation was mainly plastic.

Kyriakides et al. [8] presented their experimental work with AS4/PEEK composites, using two different setups, both with confinement of the specimens. In their work, they emphasized the propagation of structural instabilities. Their first setup, testing a cylindrical rod specimen only unsupported in the central section, resulted in sudden and unstable fiber kinking failure; due to stress concentrations, damage was initiated near the boundaries of the non-confined length; the deformation was reduced because of the confining pressure, and several kink bands formed in each specimen (inside the specimen and at its surface, single and complementary ones), with angles 12°< β <16° and widths

75 μm < w < 225 μm. The authors also verified that the propagation load was lower than the initiation one, and for that reason the similarities between kink band formation and structural instabilities were pointed out.

The specimen used in the second set-up was a thin composite ring. The experimental setup consisted in three rings (polymer, loading and specimen) arranged in an ingenious way: one polymer ring, externally confined by a stiff retainer, was compressed axially by a loading ring; due to Poisson's effect, the polymer ring expanded radially inwards, compressing the specimen ring that was tightly adjusted to its inner surface, in the radial direction. These specimens presented a sudden and catastrophic failure due to fiber kinking for larger strains than the ones verified for the previous specimens (as no free-edge effect was possible along the load direction). Moreover, these researchers also quantified the fiber imperfections found in the composite, as their connection to fiber kinking was stressed.

Vogler and Kyriakides' experimental work [22, 23] on the propagation and broadening of kink bands in AS4/PEEK composites was presented in two different papers. The first paper [22] described the broadening of kink bands. Under action of compression, using 7.6 mm thick samples with a semicircular notch of 2.4 mm, these researchers were able to initiate and fully propagate a kink band across the specimen’s width in an unstable manner. Afterwards, by reloading the specimen with an existing pre-kink, the band broadening occurred in a steady state manner. In these experiments, the out of plane kink band was constrained by clamping the specimen between two rigid plates.

During the band broadening stage, the width of the kink increased as shown in figure 4. It was concluded that broadening was dominated by fiber failure due to bending, followed by further rotation of broken segments; in addition, as these broken segments were straight but there were unbroken fibers with high curvature, one can also conclude that the fibers were kept in the elastic regime, but the matrix did go into the plastic domain. Within the band and during broadening, the fiber angle was kept around $\alpha = 41°$ and the kink band angle at $\beta = 16°$; as the authors pointed out, this did not follow the usual relation $\alpha = 2\,\beta$.

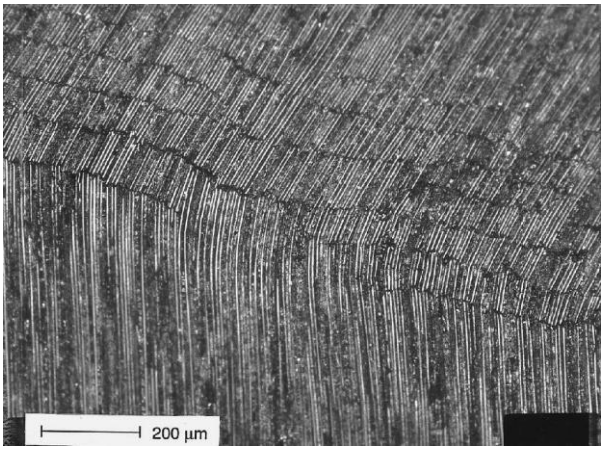

Figure 4. Kink Band Broadening and Fiber Failure (Unloaded), [22,23].

In their second paper [23], these authors show that they successfully developed stable kink bands in 3.18 mm thick square samples. The test consisted in five quasi-static steps: axial compression to a given load at first, followed by shear displacement (at constant compressive load) until the initiation of the kink band (identified by a reduction in the shear load), after which the specimens were completely unloaded; then, a new step of axial compression was performed, and. finally, the propagation of the kink band could

be observed by applying shear. During this final step, several pictures were taken, allowing the phenomenon to be followed; it was found that the inclination and width of the kink band remained constant through propagation at $\beta = 12°$ and $w = 25d_f$, while the angle of the fibers (for a given location) was increasing progressively with the propagation of the kink band proceeding at $\alpha = 26°$.

Following the total propagation of the kink band through the width of the specimen, the band started broadening, increasing its width but keeping both angles constant. After the test, the kink band was observed unloaded under the microscope, and it was found that almost no fiber failure had occurred (figure 5); this, according to the authors, was due to the (comparatively) small fiber rotation within the kink band (not requiring a curvature as high as usually observed). Taking this into account, it was concluded that the shear stresses were crucial to the formation of the kink band, being the failure of the fibers an eventual consequence [23].

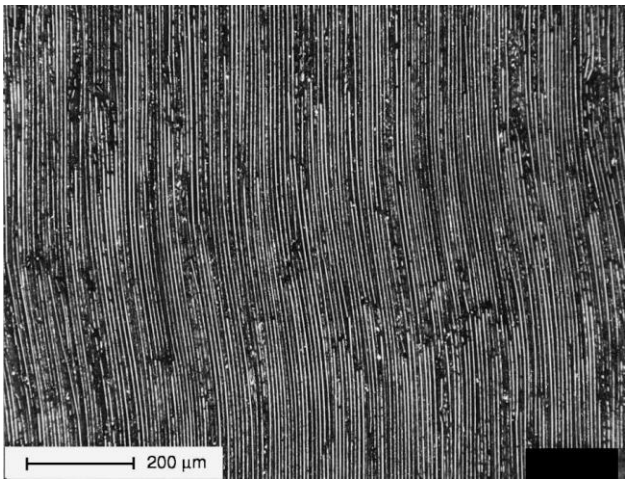

Figure 5. Kink Band Initiated by Compression and Shear, Without Fiber Failure [23]

In a review of Prabhakar's work [28], a digital image correlation (DIC) technique was adopted to measure transverse and shear strain distribution on the side surface of the laminates tested under uniaxial compression, using a 16-ply specimen to follow the evolution of the strains as a function of macroscopic stress state (see figure 6). The image in figure 6a provided a reference for the DIC measurements, corresponding to the unloaded state, while the next two images correspond to instances near the peak load and immediately thereafter. In the image in figure 6b, a delamination crack was already visible and was identified as the first event that may trigger the catastrophic failure, which, as seen in the third image, also induced kinking in the zero lamina in the post-peak regime.

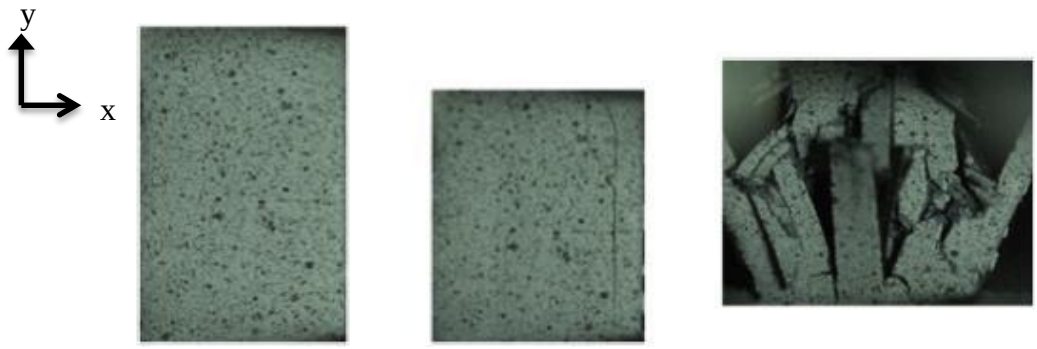

Figure 6. Lateral View of Specimen Used for DIC Measurements. (a) Unloaded (b) Peak Load (c) Failed [28].

Figure 7 shows the transverse (normal) strain distribution on the side surface of a 16-ply laminate along the global x-direction as shown for the aforementioned stages. It can be observed that the distribution is banded along the thickness, due to the different layers present in the specimens. As the loading was increased, the positive strain between the +45° and -45° layers increased rapidly, and subsequently, the specimen delaminated at that interface, as shown in Fig. 7c.

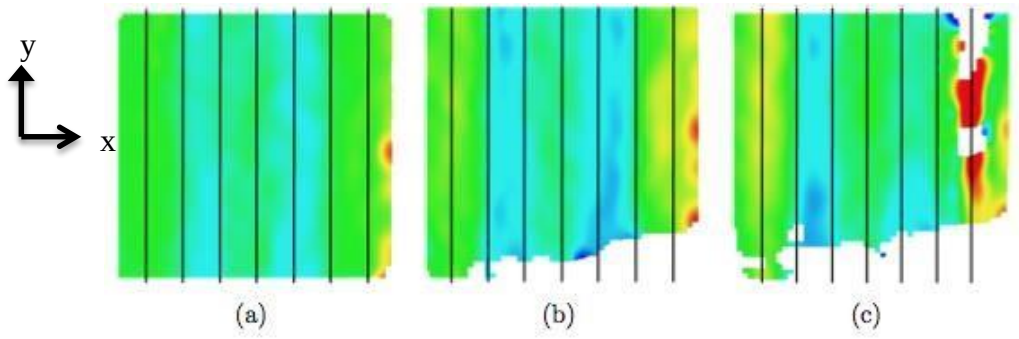

Figure 7. Transverse Strain Distribution on the Side Surface for a 16-Ply Laminate (a) Linear Stage (b) Prior Peak Load (c) At Peak Load [28].

To corroborate the above statement, the strain distributions ε_{xx} and ε_{xy} along a line on the side face were also obtained, as shown in figures 8 and 9, respectively.

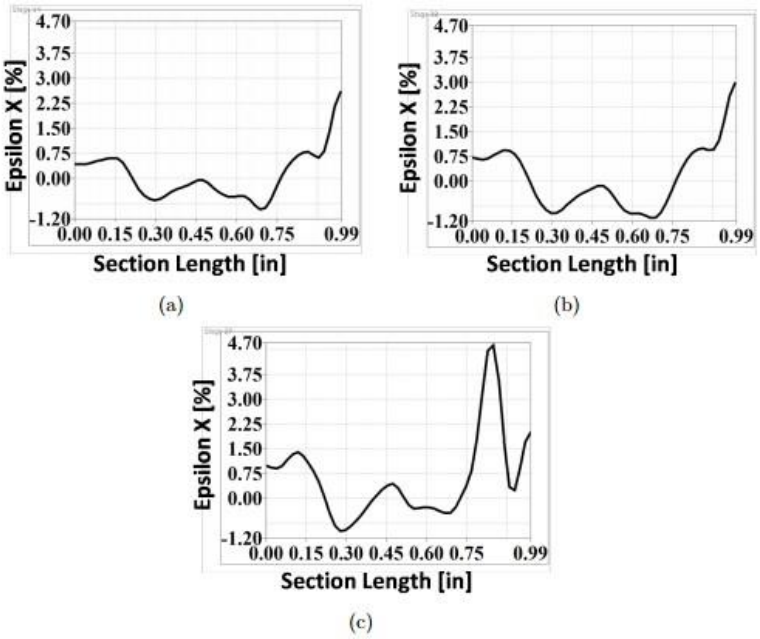

Figure 8. Transverse Strain Distribution Across the Side Surface for a 16-Ply Laminate (a) Linear Stage (b) Prior to Peak Load (c) At Peak Load [28].

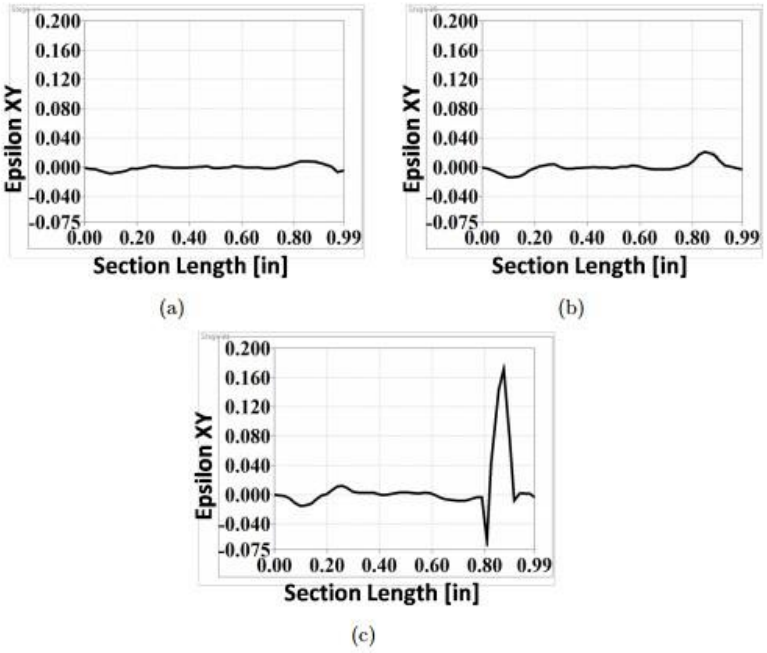

Figure 9. Shear Strain Distribution Across the Side Surface for a 16-Ply Laminate (a) Linear Stage (b) Prior to Peak Load (c) At Peak Load [28].

It is clear from figures 8 and 9 that as the load increased (progressing from (a) to (b) to (c)), the transverse strain (ε_{xx}) and the shear strain (ε_{xy}) attained maximum values at the interface between +45 and -45 layers. Upon further loading, the transverse and shear strains increased to very large values as the specimen delaminated at the interface on the right (refer to figures 8c and 9c). In summary, the specimens appeared to initiate failure by delamination followed by kink band occurring in the post-peak regime.

The aforementioned DIC work in [28] was only limited to three stages and the composites were tested in uniaxial compression. The macroscopic state reported does not give any insight into the strain fields inside the kink band during its evolution. This can be obtained by high resolution DIC, which would facilitate the quantitative assessment of displacement and strain fields inside the kink band. Moreover, the quantification of these

strain fields at high resolution during kink band evolution, in general, and during damage evolution can give additional insight into the damage mechanisms of individual plies during bending tests (under the effect of stress-gradients), all driven by plastic microbuckling.

Liu [27] researched the collapse mechanism of UHMWPE (Ultra High Molecular Weight Polyethylene) fiber composites using beams with short (L = 10 mm, L/h<10) and long (L = 100 mm, L/h>10) spans. Experiments were conducted in a cantilever configuration (see figure 10) to observe the different possible collapse modes. It was observed that short beams failed under a shear mode and long beams collapsed under a bending mode. The failure mechanism for the long beam was quite different as a plastic hinge formed near the built-in end of the beam, which resulted in formation of wedge-shaped kink bands (figure 10b). Figures 10 (b) to (d) show kink bands at different magnifications.

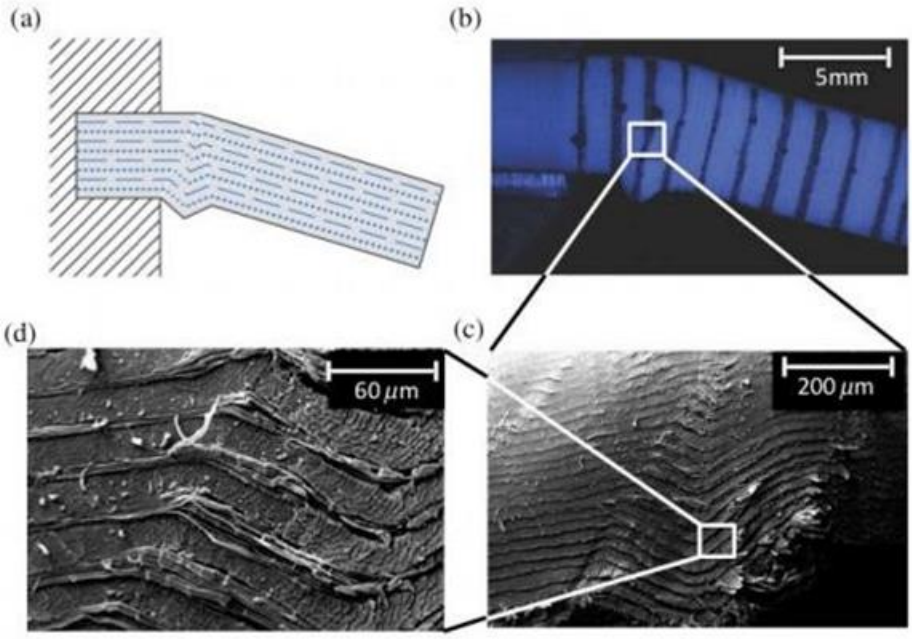

Figure 10. Plastic Hinge Formation by Microbuckling in a Long Beam (L=100mm): (a) Sketch of the Double-Wedge Kink Band. In this Illustrative Sketch, Chain Lines Denote the 0° Plies, and the Dotted Lines Denote the 90° Plies; (b)-(d) Kink Band Images at Different Magnifications [27].

The load-displacement profiles for short and long beams are depicted in figure 11(a). Figure 11b shows the deformation of short and long beams. The microbuckling phenomenon was observed with the formation of wedge-shaped kink bands for long beams. These bands are unlike the parallel-sided microbuckling bands, which have been exhaustively studied in the literature, see for example the reviews of Fleck [4], Kyriakides et al. [8] and Schultheisz and Waas [3]. Both of the observed collapse modes involved inter-ply plastic shear and elastic deformation of the plies [28].

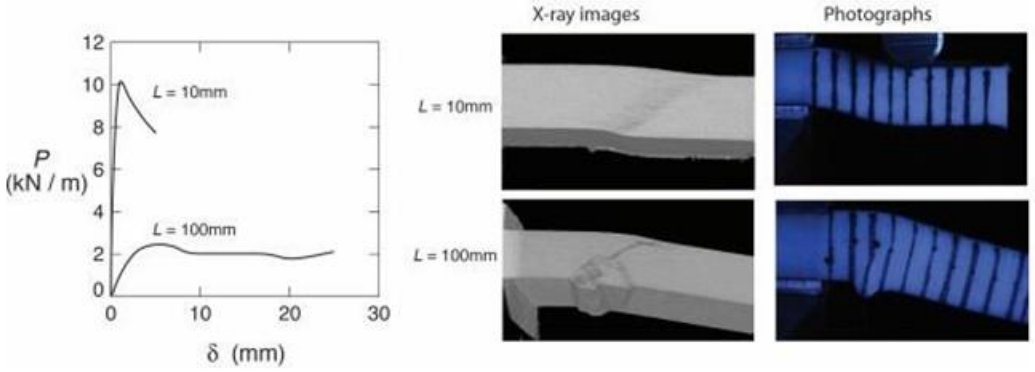

(a) (b)

Figure 11. (a) Load per Unit Width Versus Displacement Responses of Short (L=10 mm) and Long (L=100 mm) HB26 Composite Beams. (b) X-ray and Photographs Showing the Deformation of the Short and Long Beams at Applied Displacements of 8 mm and 25 mm, Respectively [27].

The primary focus of Liu's work [27] was to identify the collapse mode for short and long beams under cantilever configuration. But, unfortunately, the study did not cover any quantitative analysis of how the developed wedge shaped kink band led to delamination failure in long beams, since there was a lot of constraint near the built-in end. This constraint does affect the nucleation and evolution of the kink band during the test in cantilever configuration. Testing under stress gradients with lesser constraints, such as those present during 3-point bending, would provide a simpler stress condition, which, in turn, would facilitate both experimental characterization and modeling of kink band nucleation and evolution, as well as the mechanisms of damage initiation at these kink bands.

In addition to the aforementioned limitation, there is another gap of knowledge identified in [27]. During the bending test performed on long beams, the load-

displacement profile (figure 11a) showed some load oscillations with increasing displacement. However, there is no explanation offered in [27] for these load oscillations during kink band evolution.

The aforementioned limitations motivate to capture the physics behind these potential failure mechanisms in PMCs through finite element study. For example, the load-oscillations observed in [27] may correspond to micro-mechanisms that are responsible for interacting one or more deformation and failure mechanisms that lead to the failure of overall structure. Moreover, the sensitivity analysis in FEMs would give additional insight in to the parameters that affects the kink band morphology under 3-point bending configuration.

2.4 Numerical Simulations

The development of numerical models able to simulate the composite's behavior during the formation of kink bands is also reported in the literature, although not at the same extent as for the experimental work. Several researchers have developed numerical models to predict a composite's strength assuming fiber micro-buckling (e.g., instability), while others modeled kinking using matrix yielding and initial imperfections.

Kyriakides et al. [8] focused their numerical study on kink bands in an extended study about the influence of several physical and modeling parameters on the composite response and kink band geometry. The modeling strategy used a 2D layered approximation, assuming a periodic array of a finite number of fibers interposed with layers of matrix (figure 12 (a)), the constitutive law for the matrix considered a standard

elastic-plastic (with initial hardening) isotropic behavior, and the fibers were assumed to be isotropic and either with linear or nonlinear response. All models assumed a sinusoidal initial imperfection as shown in figure 12b and were solved using finite elements (FE) with the Riks modified method.

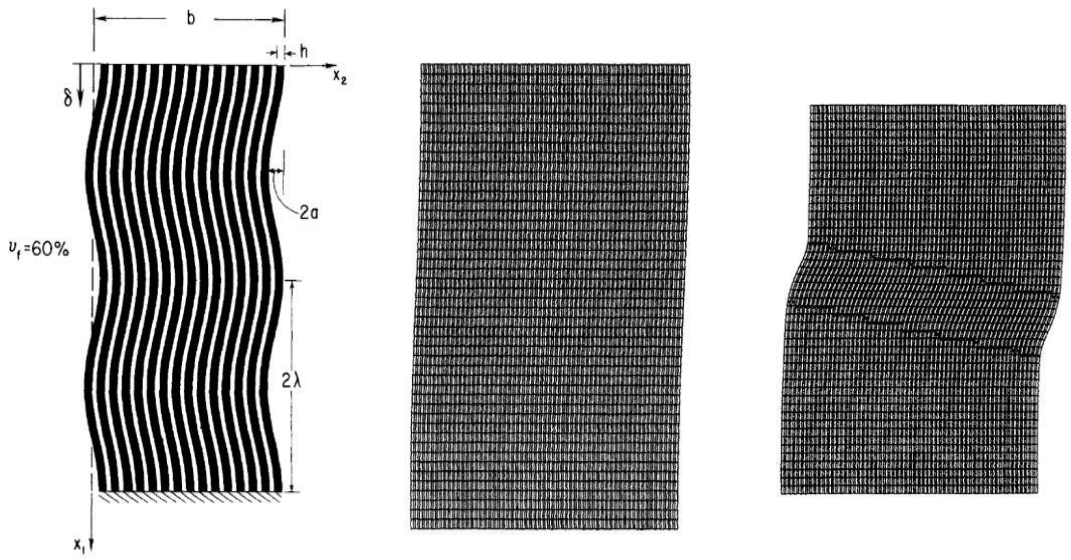

(a) (b) (c)

Figure 12. (a) Overview, (b) Imperfection, (c) Deformed Configuration. After [8].

The typical composite's global response (figure 13) is initially almost linear (points 0 to 2), until a peak load (point 2) is reached; after that, due to both geometric and matrix non-linearities, the model evolves through a softening domain with a sudden reduction on the compressive load and a recovery on the shortening (points 3 to 6), followed by further compression and load stabilization (points 7 to 9). During this softening domain, the model develops a kink band with its boundaries defined by the points with maximum bending

stresses in each fiber, increasing its width w and angles α and β as the compression progresses. Considering this overall response, a parametric study was performed. It was found that the addition of more fibers in the model would affect - increasing – the peak remote stress. In addition, the longer models (along the axial direction) presented a higher instability after the peak load, due to the greater amount of strain energy available; fiber material non-linearity was found to have a reduced influence, both on the initial domain (increasing its non-linearity, but without affecting the peak load) and final strain. The response is referred to as snap-back of fibers and depends upon an initial imperfection of the composite as shown in the above case.

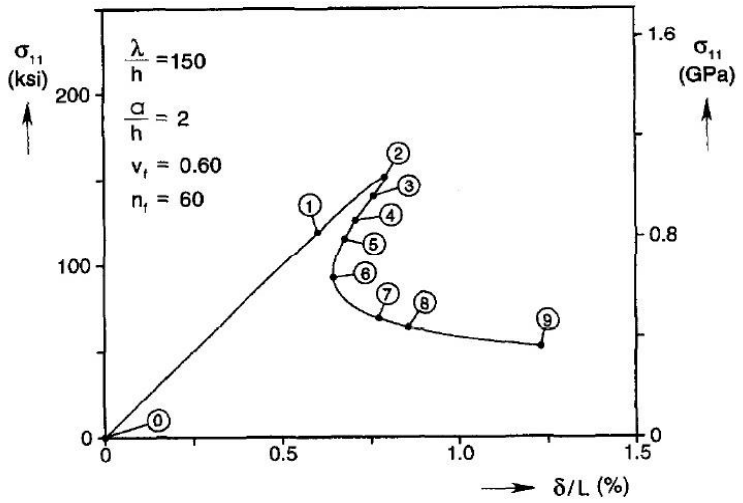

Figure 13. Snap Back Response of the Fibers (Axial Compression) During Kink Band Formation [8].

Vogler and Kyriakides [23] later extended the same model by adding capabilities under compression and shear. The approach to the problem was similar to previous work (Kyriakides et al. [8]). The fibers were modeled with global and local (for kink band

initiation) imperfections. Two constitutive laws were chosen for the matrix's plastic domain: the J_2 type solid with isotropic hardening and Drucker- Prager plasticity model as modified by Hsu et al. [47]. Overall, the models were capable of reproducing the propagation of a kink band through the fibers, both using the combined action of direct shear and compression and by pure compression only; no major differences between the 2-D and 3-D responses were found.

Moreover, a parametric study was also carried out. It was found that increasing fiber volume fraction improves the composite's strength and leads to wider kink bands with a smaller fiber angle α. A similar effect was found by increasing the fiber diameter. The matrix yield stress affected material strength and the kink band geometry (a stronger matrix gave a wider band with fibers more inclined). On the shape of the initial imperfection, it was found that the most relevant parameter was the amplitude of the global imperfection, with a severe impact on the composite strength. Finally, it was found that the number of fibers included in the model had an effect on the kink band geometry, since both the band and fiber inclination (β and α) increased for the models with fewer fibers.

Pimenta [25] developed several FE models to study the sequential events of kink band formation with respect to micromechanics. In this work, four different models were created to initiate the kink band and to study the response curves. They ran 2-D numerical simulations using the FE method for kink band initiation and propagation and analyzed the results in detail; models make use of initial imperfections, independent matrix and fiber representations and yielding and softening constitutive laws for both constituents. Useful information to understand how and why kink bands are formed was obtained from

the analyses and their discussion; shear stresses and matrix yielding were found to play a major role on kink band formation. In addition to the basic process, several other experimental features were reproduced as well. The description of the models is as follows:

- Cohesive model with failing interface, implemented through a decohesive constitutive law for the matrix;
- Matrix model with yielding interface, implemented through an elastic-plastic constitutive law for the matrix;
- Continuous damage mechanics (CDM) model with failing fibers (short configuration), using a bi-linear constitutive law for the fibers (both in compression and tension);
- Extended CDM model with failing fibers and extended (twice as long) configuration, with straight ends added to the initial imperfection.

In all these models, fibers were treated as isotropic and linearly elastic and the matrix was modeled either by elastic-plastic elements or by interface/cohesive elements. The load vs. displacement profiles of all four models are shown in figure 14.

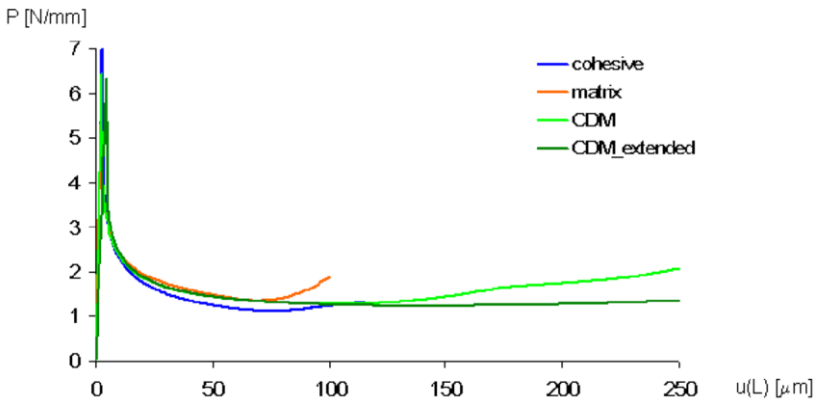

Figure 14. Load (P) vs. Displacement (u) Profiles of Four Models on Kink Band Initiation [25, 26].

Figure 14 shows the expected behavior for fiber kinking: the response is stiff and nearly linear at the beginning, which can be identified as an elastic domain, with a sudden reduction in the stiffness after the peak load is reached; afterwards, the material continues to be compressed under a progressively reducing load, i.e., a softening domain. The initial stiffness is approximately the same in the four models; the major difference is found in the CDM-extended model, which is slightly softer than the other three. The peak load is also similar in all of them, being slightly higher in the model with failing (cohesive) interface [25].

Right after the peak load, all the models converge to the same solution; as compression continues, the model with the failing interface shows a slightly higher degree of softening than the other three. Models without failing fibers (cohesive and matrix) do stiffen, so the load increases for further compression; that behavior is delayed in the short model with the failing CDM interface, and visibly reduced in the extended configuration (CDM-extended).

Comparing these results with the analytical model in [26], the onset of fiber failure in the numerical simulation starts in the outer fibers and progresses transversely. As the analytical model has no edge effect, it predicts fiber failure to start after the numerical onset of outer fiber failure. On the other hand, the curvature of the central fiber in the numerical model is reduced due to the transverse stiffness of the composite as a whole, delaying its failure. For these reasons, the analytical onset of fiber failure occurs between the numerical onset of failure in outer and central fibers.

Prabhakar et al [28] reported a novel computational modeling framework to predict the compressive strength of fiber reinforced polymer matrix composite (FRPMC) laminates. The model accounts for interaction between kink-banding and interface fracture (or delamination), which are observed in experimental results. To reduce the size of the computational model, those interfaces that are most susceptible to delamination are first determined through a free-edge stress analysis. Furthermore, off-axis layers, which are passive in the failure process, are represented through an equivalent homogenized model, but the microstructural features of the on-axis layers (zero plies) are retained in the computational model. This study mainly focuses on homogenization techniques for laminates.

A repeating unit-cell of 8 layers [-45/+45/90/0]s of multi-directional carbon fiber reinforced polymer matrix composites is investigated. Two different models (i) a fiber-matrix discrete model and (ii) an up-scaled semi-homogenized model have been implemented to predict the compressive strength. The semi-homogenized model was later extended to enable delamination prediction capabilities by adding interface elements.

Delamination is governed by the fracture properties of the matrix and/or fiber matrix interface [28].

In the fiber-discrete model, each lamina has been modeled as a hexagonally packed transversely isotropic layer having three rows of fibers. The fiber diameter and the volume fraction are 6 μm and 0.49, respectively. These laminae are scaled layers that capture these two features but do not have the same thickness as the laminae in an actual laminate. Figure 15 (a) shows the scale model simplification of the laminate, where red, cream, blue and green regions are fibers in -45, +45, 90 and 0 degrees, and the rest is the matrix material. Figure 15 (b) shows a model with a small imperfection and boundary conditions.

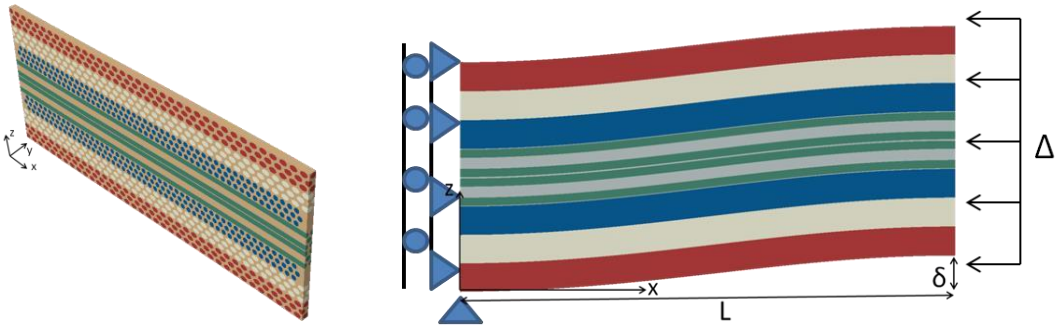

(a) (b)

Figure 15. (a) Fiber-Matrix Discrete 3-D Model Consisting of 8 Layers, (b) Model with Imperfection and Boundary Conditions [28].

In the model shown in Figure 15, the fibers are modeled as elastic transversely isotropic materials and the matrix is modeled as an elastic-plastic isotropic material [28].

The up-scaled homogenized model consists of 8-layers of laminae (see Fig. 16), where the off-axis layers, i.e., -45°, 45°, 90° layers are homogenized using the technique mentioned in the previous section. Here, the red, cream and blue regions are the

homogenized -45, +45 and 90° laminae. Micro-mechanics is maintained in the zero degree layers, as they are the load bearing layers and are responsible for kink band formation in multidirectional laminates. Therefore, the regions in green are the 0° fibers, and regions in grey are the matrix in 0° lamina. The imperfections imparted, boundary conditions and loading applied are identical to the discrete fiber-matrix model. Results show good agreement between both models. An up scaled semi-homogenizing method was formulated using deformation plasticity theory along with Hill's anisotropic plasticity model to predict the compressive strength allowable for composite laminates, dominated by kink banding failure. More details can be found in [28].

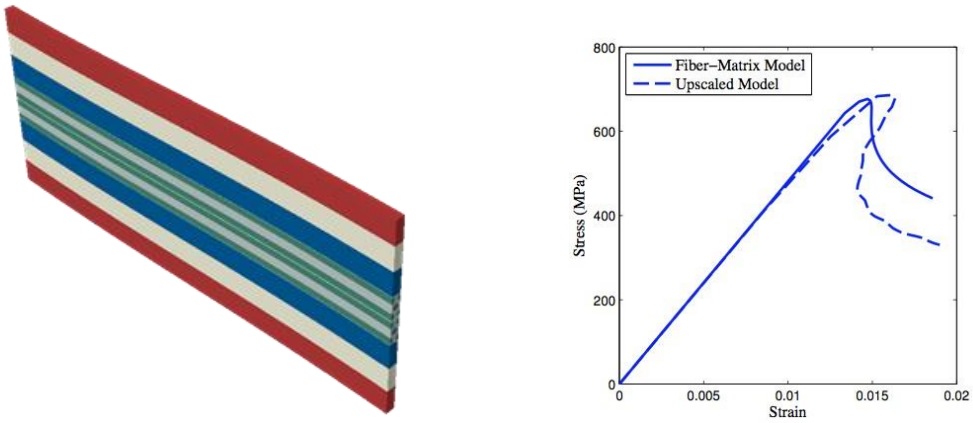

(a) (b)

Figure 16. (a) Up-Scaled Homogenized Model Consisting of 8 Layers and (b) Comparison of Global Stress-Strain Response between Discrete Fiber-Matrix Model and Up-Scaled Homogenized Model with 1° of Imperfection [28].

This semi-homogenized model was later extended in conjunction with de-cohesive zone modeling (DCZM). Modes I and II delamination failures are incorporated with

appropriate traction separation laws at -45°/+45° interfaces to capture delamination along with kink-banding. Figure 17 shows the different phases of development of a kink band along with delamination at a -45°/+45° interface.

The aforementioned model accounts for failure mode interaction between kink-banding and interface fracture (or delamination), which are observed in uniaxial compression tests. The idea of simulating the behavior of these composites via microstructurally explicit representations of plies in the models has been adopted as one of the objectives of current research. However, the presence of stress-gradients during 3-point bending is bound to make a difference in kink band evolution through the plies as compared to pure compression, and it is important to understand how the microbuckling event is triggered and interacts with other damage mechanisms during the kink band evolution through the plies under the influence of stress-gradients.

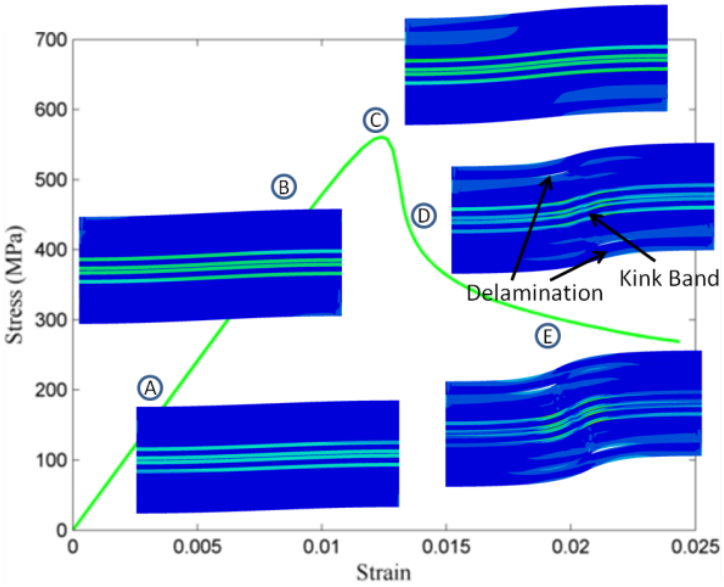

Figure 17. Global Stress-Strain Response along with Deformed Shapes of an Up-Scaled Model with DCZM Added at -45/+45° Interface. σ_c=12.5 MPa and τ_c=15 MPa, Where σ_c and τ_c are Cohesive Strengths in Mode I and Mode II Respectively [28].

Liu [27] modeled the collapse response of long beams, involving the introduction of a small imperfection (Φ) near the cantilever support [27]. A two-dimensional finite element model was created using 0 and 90° plies in a cross-ply stacking sequence. The interface was taken into account by introducing cohesive zone elements between the alternating plies [27]. A typical schematic is shown in figure 18. Plies were constructed with plane strain elements and orthotropic material properties, whereas the interface was modeled using an elastic-plastic traction separation law with cohesive elements. Details on properties and methodology can be found in [27].

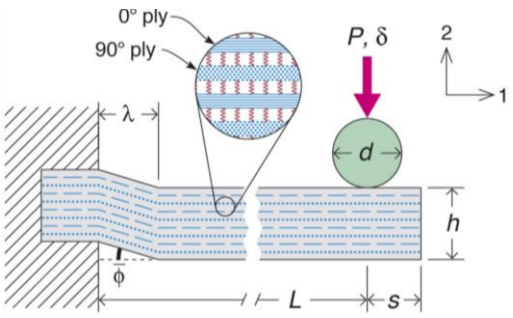

Figure 18. Sketch Illustrating the Details of a Finite Element Model of Cantilever HB26 Composite Beams used in [27]. Chain Lines Denote the 0˚ Plies, and the Dotted Lines Denote the 90˚ Plies.

The finite element analysis of long beams demonstrated that the wedge-shaped double kink mechanism involves interlaminar shear, along with elastic shear and elastic bending of the intervening plies. A sensitivity analysis was performed to study deformation and bending hinge formation for three different values of Mode II, inter-laminar shear stress as shown in figure 19.

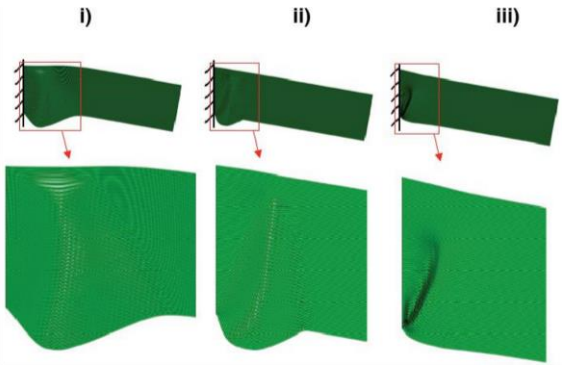

Figure 19. Finite Element Calculations to Illustrate the Sensitivity of the Response of Long Cantilever Beams; Predicted Deformed Configurations for the Three Choices of Inter-Laminar Shear Strength: (I) 0.2 MPa; (II) 2 MPa and (III) 20 MPa. Results are Shown for an Applied Rotation [27].

In addition to the above parametric study, the extended work of Liu in [63] identified the sensitivity of microbuckling response to overall effective shear modulus and interlaminar shear strength of long composite beams. However, the study did not emphasize on the sensitivity of kink band morphology in particular; addressing width of the kink band, band inclination angle and band rotation angle for the long beams with varying thickness. Hence, there is a gap of knowledge to address the above-mentioned particulars, which is an area of interest and one of the potential modeling objectives of the current research.

2.5 Constitutive Modeling of Polymer Matrix Composites

The behavior of most PMCs is known to be rate-dependent due to the viscoelastic and viscoplastic nature of their matrices. Several experimental studies have been performed with the goal of determining the effects of strain rate on the mechanical

properties and response of PMC systems at high strain rate conditions. A survey done by Gates et al. [42] describes several analytical models to simulate the rate-dependent response of various types of PMCs. Later Gates and Sun [42] developed an elastic-viscoplastic model for an orthotropic material without tension/compression symmetry and Gates [42] used an extension of that model to describe an experimental methodology to generate material constants. Goldberg and Stouffer [4] presented an historical survey of experimental development to study the strain rate effect on mechanical properties of polymer matrix composites, followed by constitutive modeling [43].

Most PMCs are pressure sensitive materials too. The hydrostatic stress can cause significantly greater changes in the mechanical properties of polymers and polymer-matrix composites than in metals or rocks. Furthermore, polymers and polymer-matrix composites yield at different stresses in tension and compression, while the elastic modulus increases with hydrostatic pressure [54, 55, 56].

One possible approach to modeling the constitutive response is through the use of a plasticity approach to generate the non-linear stress-strain curves observed experimentally for UD composites. [59]. Several reports in the literature use a viscoelastic approach to capture the time dependent behavior of these materials [57, 58]. Vyasa [59] studied loading under quasi-static conditions at the ply level and so an elastic-plastic constitutive law is used with a Drucker-Prager yield criterion. A pressure dependent yield criterion for UD composites is formulated and achieved by some mathematical manipulations in an existing yield criterion. The proposed yield criterion by Vyasa [59] is

both hydrostatically sensitive (predicts the increase in yield with pressure) and accounts for the different response of UD composites in the fiber direction.

Attwood et al [53] have proposed a constitutive model of Dyneema composites for out of plane compressive response. For a UD ply, to retain consistency with the anisotropic elastic response, an anisotropic yield criterion was proposed that models the non-linear response of the composite. This is based on the following considerations:

- The ply is treated as elastic in the fiber direction.
- In all other directions, ply yielding is assumed when the maximum shear stress reaches a shear yield strength similar to the Tresca criterion for metals.
- However, unlike metal plasticity, the shear yield strength of polymers (including polyethylene) is pressure dependent.
- Plastic straining is incompressible, i.e., the flow rule is non-associative.
- Rate insensitive due to very low strain rate explored in the investigation [53].

Hsu et al. [47] presented micromechanical models for simulating the non-linearities exhibited by AS4/PEEK composites in shear and transverse compression, their interaction, and their rate dependence at room temperature. The fibers are assumed to be transversely isotropic and to be distributed in a hexagonal pattern in the matrix. The PEEK matrix is modeled as an elastic, power-law viscoplastic, isotropic solid through two related models. Model 1 is a simple J_2–type visco-plastic formulation; Model 2 is a rate dependent version of the non-associative Drucker-Prager model. Both models are calibrated so that they reproduce the shear response of the composite and they capture the rate dependence

of the composite well. The unit cell model is capable to examine the stresses in the composite.

Most of the above literature review covers the constitutive framework for individual constituents – fiber and matrix, by modeling their plasticity using different criteria. The information on constitutive modeling of UHMWPE composites at ply level is very limited. Note that, all proposed models include pressure sensitivity and hence implications can be drawn from this survey that a constitutive modeling of a UD ply in UHMWPE composites (Dyneema and Spectra shield) may require a hydrostatic pressure sensitivity term in a yield function. However, it is not required in the present study as [27, 63] do suggest that the microbuckling response is a result of elastic bending of plies and plastic shearing of interfaces. Moreover, the implications in literatures [8, 23, 27, 28, 47 and 63] also suggest that modeling of fiber kinking /microbuckling may not require consideration of plasticity at the constituents such as ply or fibers as the influence on the response is untraceable, but the matrix constituent does require plasticity/non-linearities which is a likely case in modeling the interfaces between the plies of composites. This motivates incorporating the plasticity in the cohesive zones (represent the interfaces) in terms of traction–separation law, which has been explained in the next section. Therefore, it is essential to obtain the mechanical response of the interfaces through Mode I (opening mode of crack) and Mode II (shear mode of crack) delamination fracture tests and same needs to be modeled through cohesive zones.

2.6 Cohesive Zone Modeling (CZM)

Mode I Fracture in Polymer Matrix Composites

Continuum damage mechanics is not very suitable to model damage at physical interfaces like adhesively bonded joints, which is common in polymer matrix composites [44, 45]. A commonly used technique to simulate damage at these interfaces and their separation to form new surfaces is the so-called cohesive zone modeling. Cohesive zone models have been widely used to model crack initiation and growth in fracture mechanics problems and they are implemented in most of the commercially available finite element codes (citation!). The basis for cohesive zone models can be traced back to the works of Dugdale [44] and Barenblatt [45]. In practice, the cohesive zones are modeled with zero-thickness elements between the continuum elements that open apart under a tensile load. However, to simulate the mechanical response of mode I fracture in adhesively bonded joints, a cohesive zone should be modeled with finite thickness to represent the physical condition of the interface in addition to match the mechanical response obtained in experiments [60].

Alfano and his co-workers [29] have provided substantial information in modeling fracture in adhesively bonded joints. According to CZM, the fracture process is lumped into the crack line and is characterized by a cohesive law that relates traction and displacement jumps (T-□) across cohesive surfaces. In the simplest and most usual formulation of CZM, the whole body volume remains elastic while the nonlinearity is embedded in the cohesive law, which dictates the interfacial conditions along the crack line (see figure 20) The peak stress on the cohesive law is the cohesive strength of the

material, σ_c, while the area under the curve is the cohesive fracture energy, G_c. As a consequence, the fracture process can be summarized as illustrated in figure 20: at first a linear elastic material response prevails (1), as the load increases the crack initiates ($T=\sigma_c$) (2) and then, governed by the nonlinear cohesive law, it evolves from initiation to complete failure (3) with the appearance of new traction free crack surfaces ($\Delta=\Delta_c$) (4).

It is therefore necessary to provide two constitutive laws (i) a linear or non-linear stress-strain relation for the bulk material and (ii) a cohesive law that allows spontaneous crack initiation and growth. To achieve this, it is very important to select a proper shape of the softening region.

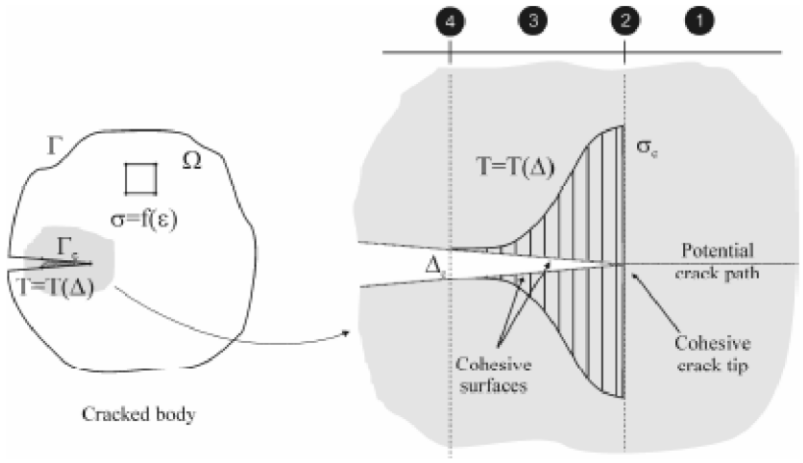

Figure 20. Cohesive Zone Modeling and Fracture [29].

A typical mode I bilinear law is depicted in figure 21. The slope of the initial linear region is known as the penalty stiffness [29]. The traction-separation law needs to be incorporated precisely if calibration and validation with experimental results are required. There are many factors related to this cohesive law, but the governing factors that have

the most influence on the mechanical response are the peak stress σ_c and the critical energy/fracture energy G_{Ic}.

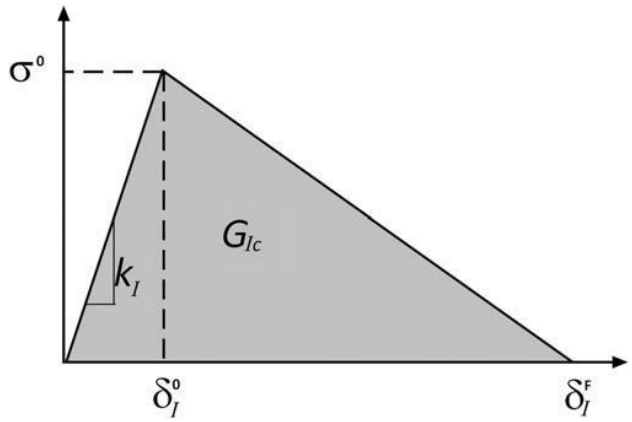

Figure 21. Mode I Bilinear Cohesive Law

The T - Δ curves can have many different forms, e.g., a smooth non-linear curve instead of a triangular shape and it can be tuned depending on the physical conditions.

In a review of Lee et al. [62], referring to a single leg bending joint (similar to a 3-point bending test) offers an inherent mixed-mode condition, normal and shear behaviors arise concurrently in the fracture process zone. Damage initiation in the mixed-mode condition is evaluated by a quadratic criterion including the stress components (σ_I, σ_{II}) and the critical cohesive strengths (σ_{Ic}, σ_{IIc}), as shown in Eq. (2.7). Lower indices '*I*' and '*II*' represent modes I and II, respectively, and lower index '*c*' means the critical value. Crack growth along the cohesive layer is evaluated by a linear criterion considering the energy release rates (G_{Ic}, G_{IIc}) and the fracture toughnesses (G_I, G_{II}), as shown in Eq. (2.8). Damage initiation at a given element starts when the equality of Eq. (2.7) is satisfied, and

complete separation occurs ruled by Eq. (2.8) in a similar way. The shape of the traction–separation law for each mode is defined as a bilinear model, similar to that in figure 21, with three cohesive parameters: fracture toughness (G_{Ic}), critical or peak cohesive stress (σ_{Ic}, σ_{IIc}) and penalty stiffness (K_I, K_{II}).

$$\left(\frac{\sigma_I}{\sigma_{I_C}}\right)^2 + \left(\frac{\sigma_{II}}{\sigma_{II_C}}\right)^2 = 1 \tag{2.7}$$

$$\left(\frac{G_I}{G_{I_C}}\right)^2 + \left(\frac{G_{II}}{G_{II_C}}\right)^2 = 1 \tag{2.8}$$

The cohesive zone model in pure modes I and II is generally calibrated using the Double Cantilever Beam (DCB) test and the End Notched Flexure (ENF) test, respectively [62]. However, the procedure for determining the cohesive parameters does not seem to be systematic and efficient because these are obtained iteratively by matching the experimental results and simulation results [62].

The literature review provided here shows that there is a substantial body of knowledge on the formation and evolution of kink bands in PMCs, as well as the failure of these materials via delamination. Nonetheless, the same literature strongly suggests there is gap of knowledge in understanding the detailed mechanisms for kink band evolution, experimentally and with finite element models, especially under the effect of stress-gradients, and how that evolution leads to failure due to delamination. One key goal of this research is to bridge this gap, and the specific objectives of this research that will enable this overall goal are given in the next section.

3. OBJECTIVES

Kink band formation and growth can be a sudden and unstable process in PMCs. The parameters associated with it are complex to understand. The phenomenon of the sequential events of kink band nucleation and evolution has been explored by many researchers through both experiments and modeling approaches, with emphasis in uniform stress states like those obtained under pure compression. This work has led to theoretical predictions of compressive strength of the composite, relationships between kink band inclination angle and fiber rotation angle and macroscopic strain evolution during band propagation using kink band geometric parameters. However, this previous work has not provided yet a thorough understanding of the sequential events of kink band formation, evolution and failure of PMCs under stress-gradients, which are present during bending, an extremely important loading mode for practical application of PMCs.

The presence of stress-gradients is bound to make a difference inside the kink band as compared to kink bands observed in pure compression. The micro-buckling phenomenon is more localized under stress-gradient effects, which strongly suggests that heterogeneities should exist inside the band. These heterogeneities, in turn, are bound to have important effects on kink band evolution and its interaction with damage mechanisms. Hence, a key experiment proposed here is the measurement of the strain field inside the kink band via high resolution Digital Image Correlation (DIC), starting from nucleation and following through kink band propagation and material failure. These measurements will be complemented with modeling of the deformation mechanisms using

microstructurally explicit finite element models and then leverage those models along with experiments to understand how kink bands lead to failure of the samples via delamination. In this regard, the specific objectives of this research are as follows:

Experimental Objectives:

- High-resolution DIC measurements to facilitate the quantitative analysis of displacement and strain fields inside and around the kink band during its evolution under stress-gradients – as present during 3-point bending tests for Dyneema HB80 and Spectra Shield specimens.
- Qualitative analysis of different damage/failure mechanisms and their interaction with plastic micro-buckling, which lead to failure of samples via final delamination.
- Quantification of micro-mechanisms leading to load-oscillations during 3-point bending tests for both the materials.
- Quantification of inter-laminar mode I and mode-II toughness and determination of ply interfacial strength. These experiments are required for calibration and validation of cohesive zone models of ply decohesion.

Modeling Objectives:

- To develop micro-structurally explicit finite element models in ABAQUS/Standard to capture microbuckling response under bending for both UHMWPE composites – Dyneema HB80 and Spectra Shield materials.

- To leverage the micro-buckling model along with experiments to understand how kink bands nucleate and grow under bending and lead to failure of PMC samples via delamination.
- To simulate mixed-mode delamination fracture with Cohesive Zone modeling (CZM), by embedding cohesive zones between plies using cohesive elements.
- To do parametric analysis of mechanical (global) (load vs. displacement curve obtained in simulations) and microbuckling response by changing variables such as geometry, increasing or decreasing number of plies and interfacial properties.
- Sensitivity analysis of kink band morphology in particular; kink band width, band inclination angle, band rotation angle.
- Identify parameters or variables that influence the mechanical and microbuckling response closer to the results obtained in experiments – 3-point bending and Mode I and Mode II fracture tests.

4. METHODOLOGY

4.1 Experimental Procedure

4.1.1 Three Point Bending Test

Samples of Dyneema HB80 and Spectrashield were machined from the plates to conduct 3-point bend tests to study the kink band formation and nucleation. Both the materials, Dyneema HB80 and Spectrashield, used in this study are a cross-ply laminate $[0/90]_s$. Each of the material plate had a thickness of 10.57 mm thickness. The samples were cut from the plates by water jet as rectangular parallelepipeds with 10.57 mm thickness, 12.38 mm width and 203.2 mm length. Sample dimensions are shown in Table 1, which result in an acceptable 1 to 20 thickness to span ratio [48]. The samples were tested as received from machine shop. There was only one kind of sample preparation applied as in terms of speckle pattern for DIC, on the side surface of the sample. The detailed procedure of speckle pattern for DIC has been discussed in the next section of this chapter.

Note that 3-point bending leads to a significantly reduced constraint as compared to a cantilever beam, which will allow to study kink bands without spurious effects of restrictive boundary conditions, as was the case in [27]. Understanding the sequential events of kink band formation and evolution is a complex phenomenon as the process can be sudden and hence all tests were conducted under displacement control with a very slow displacement rate to insure stability. ASTM D7264/D7264M - 07: “Standard Test Methods for Flexural Properties of Polymer Matrix Composite Materials” [48] was followed as closely as possible.

Table 1. Sample Dimensions (in mm) for 3 Point Bending Tests (Aspect ratio Followed in [48]).

Total Beam Length	203.2
Supported Beam Length	152.4
Beam Width	12.38
Beam Thickness	10.57

Tests were performed at room temperature using a computer-controlled, screw-driven, electro-mechanical load frame under displacement control with a constant displacement rate of 2 mm/min. Samples were rested on knife-edge roller supports (see figure 22), a radius of 5 mm, as accepted by the standard [48] and load was applied through the roller of 5 mm radius [48] in the middle of the span. Load vs. displacement data were captured digitally during the tests and used to obtain normalized load vs. displacement curves from the equations that are equal to stress-strain curves as long as strain is elastic.

$$\sigma = \frac{1.5P\ L}{bh^2} \tag{4.1}$$

Where, σ = stress at the outer surface at mid-span, MPa, P = applied force, N, L = support span, mm, b = width of beam, mm, and h = thickness of beam, mm

$$\varepsilon = \frac{6\delta h}{L^2} \tag{4.2}$$

Where, δ = mid-span deflection, mm, ε = maximum strain at the outer surface, mm/mm, L = support span, and h = thickness of beam, mm.

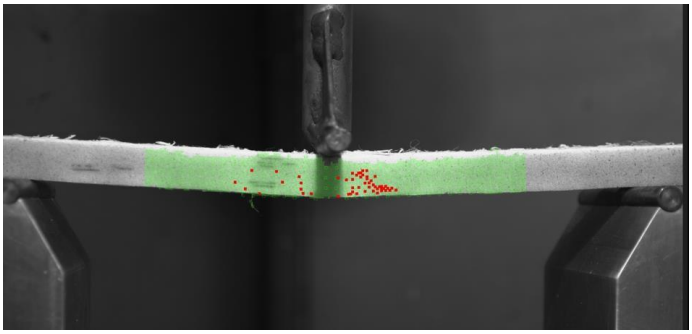

Figure 22. Experimental Setup for 3-Point Bending Testing: Dyneema HB80 Sample Resting on Knife-Edge Rollers and Subjected to Load at the Center of the Span Through a Pin.

4.1.2 Digital Image Correlation and Optical Microscopy

Sample Preparation for 3-point bend and DIC

It has been discussed in previous sections (from experimental observations) that, the length scale of the kink band is in the range of tens to a few hundred microns and one of the objectives of this research is to quantify the strain field within and around the kink band. In particular, the width of the kink band is approximately 600 microns, observed in the experiments. So, in order to get accurate results for the 2-D strain fields inside and next to the kink bands, the technique requires the best possible speckle pattern for the size of the feature to examine and the desired resolution; optimal illumination and magnification (see Fig. 23). The white fluorescent CFL bulbs of 1400 lumens were used to provide optimal illumination on the side surface of the sample. The manipulation of parameters such as focal length and aperture control (F-stop) in camera (Edmund Optics™ CMOS sensor, 5MP) and Rodenstock™ 35 mm lens assembly resulted in a field of view

of 15 mm x 15 mm, which was adequate enough to focus the kink band on the side surface of the sample. This entire procedure has been explained in detail in the data acquisition section.

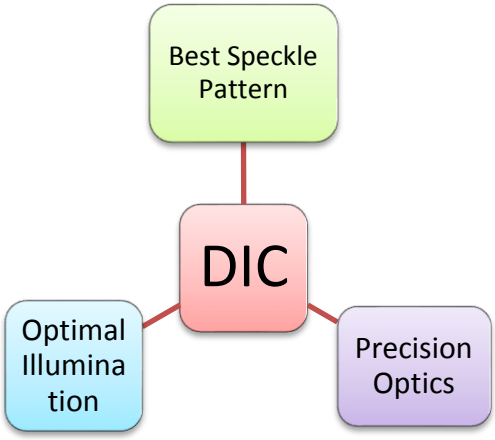

Figure 23. Parameters that Affect DIC Measurements, After [73].

In this regard, a more generalized and common technique [73] of spraying the black ink with an airbrush that had a fine nozzle tip of 0.3 mm diameter was applied to meet the desired length scale of the kink band width. Spraying this way resulted in a fine droplets of approximately 20 to 25 μm, mean size diameter along with an optimum inter-spacing (≤10 μm) of the dots to obtain enough resolution through the kink band width. Moreover, the speckle pattern had enough contrast on the white sample surface (both dyneema and spectrashield), which is the utmost requirement in DIC for best results.

An example of fine droplets created by an airbrush (Paasche – 0.3 mm nozzle tip) and picture taken by optical microscope is illustrated in Figure 24 (a) and its associated histogram in (b).

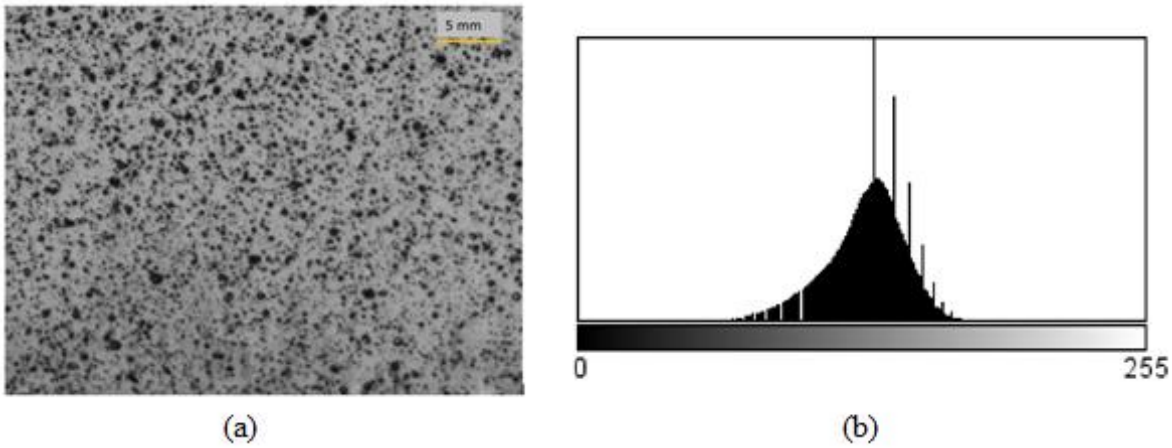

Figure 24. (a) Speckle Pattern Created with Paasche 0.3 mm Nozzle Tip in a Field of View of 5 mm by 5 mm. (b) Its Associated Histogram – Gray Value Distribution.

The inter-spacing of speckle dots was adequate within the kink-band region (see fig. 39a) as the band would contain enough dots to resolve the strain field with the desired resolution. The average spacing of these particles can be estimated by obtaining the distribution of nearest neighborhood distanced (NND). The NND of speckle dots in the above image was ~ 10 μm calculated from Image J software. However, the above-mentioned technique was not successful when tested along with 3-point bend experiment. In addition to the diffusion of black ink droplets in to both the UHMWPE samples, the speckle sheared/smeared (see figure 25) within the region of kink band during the test, which was in vain to further analyze the displacements and strains as there were no data points in terms of speckle dots. Note that, the same image also suggests the length scale of the kink band width that is in order of few hundred microns.

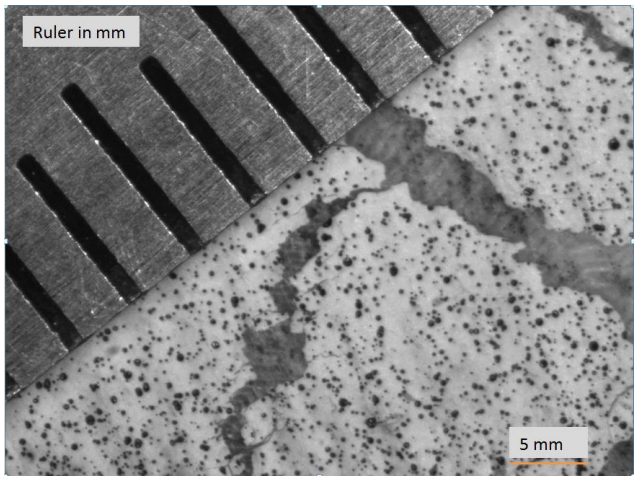

Figure 25. Smearing of Speckle Pattern Created with Paasche Airbrush within the Kink Band Region.

The aforementioned issue eventually led to develop new techniques by creating a carrier medium on the sample surface that allows applying the speckle on it and remains undiffused and does not shear during the kink band nucleation and evolution.

The following two different techniques were implemented to create a micro-scale speckle pattern along with the medium in order to meet the length scale of kink band.

1. Micro-scale speckle created with copper particles settled in epoxy
2. Micro-scale speckle created with copper particles on a thin adhesive film

Micro-scale speckle created with epoxy and copper particles

The first step was to create a solution of epoxy and hardener, by taking a ratio of 10:1 by weight. In this case, *4.55* grams of epoxy by weight and *1/10*th of epoxy solution, *0.45* grams –hardener was used to prepare the epoxy-hardener solution. After this process, *1 to 2* grams of fine Cu powder (diameter of 5 μm) was mixed with the prepared epoxy-

hardener solution. The entire solution was mixed with care to avoid any formation of air bubbles and clusters of Cu particles. Then after, this solution was applied as a thin layer to the side surface of beam samples. The samples were stored at room temperature (77 F) for 24 hours to cure the applied solution. The resulting speckle is shown in figure 26.

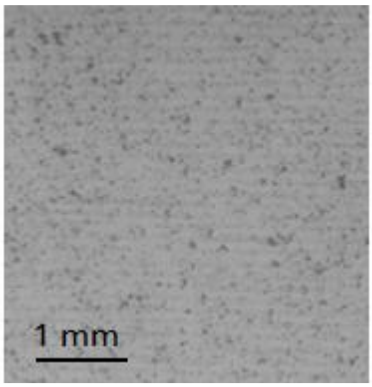

Figure 26. Resulting Speckle Pattern of Copper Particles Mixed with Epoxy-Hardener Solution.

Micro-scale speckle created with copper particles on a thin adhesive film

In this method, a thin adhesive film, 3M™ Adhesive Transfer Tape 9485PC of 100 micron thickness was applied with adequate pressure on the side surface of beam samples. For better adherence, the film was cured for 24 hours at the room temperature. After curing of film, the Cu particles were applied on top of the film by dropping them from a fine mesh sifters, a size of 100 μm and 150 μm respectively, placed on top of each other to get fine particles . As a result of this action, the fine particles adhered to a film and formed a micro-scale speckle pattern. The resulting speckle is shown in figure 27.

Both of these above listed methods were tested by taking the pictures with the same camera-lens assembly and analyzing the pictures in a DIC software, GOM

ARAMIS^{TM} with two different known deformations (i) axial stretch of the picture in x-direction by 1% and (ii) rigid body rotation of the same picture by 5 degrees in anti-clock wise direction.

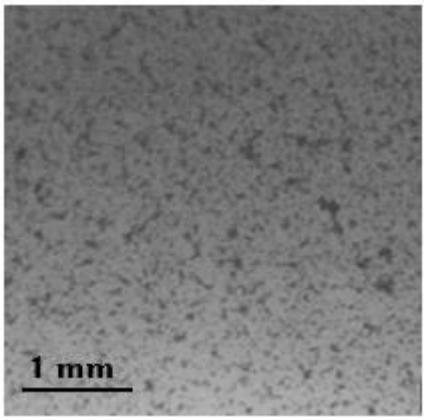

Figure 27. Resulting Speckle Pattern of Copper Particles on a Thin Adhesive Film.

From [31, 32], for case (i) a normal strain, $\varepsilon_{xx} = 1\%$ in ARAMIS^{TM} was achieved as a result because it was purely stretched in x-direction. For case (ii), the deformation gradient tensor [F] = [R] was a result from ARAMIS^{TM}, where R is an orthogonal rotation matrix. The components of matrix [F] were extracted from ARAMIS^{TM} (refer to the ARAMIS manual [73] for more details to extract the components of [F]).

Data acquisition for DIC

Localization of strains within the kink band during a 3-point bend test was analyzed by two dimensional (2-D) DIC using GOM ARAMIS^{TM} software. This technique measures the displacement fields of an object under load and uses that displacement field to obtain in-plane strain fields. The samples were prepared with one of the methods

described in previous paragraphs to create a fine speckle pattern so that the camera could detect the movement of the speckle points as load was applied.

A 5 MP monochrome CCD camera with a ½ inch CMOS sensor from Edmund Optics™ was attached with Rodenstock™ 35 mm lens to get adequate resolution, to focus the speckle dots on the sample surface with 1400 lumens fluorescent CFL light bulbs. Note that, the size of the kink band width has been observed in order of the tenth to the few hundred microns, reviewing the literature [8] and also implied referring figure 25. Therefore, the manipulation of the parameters such as focal length and aperture control of the camera and lens assembly was a key factor to obtain the desired resolution in order to resolve the size of speckle dots (micro-speckle) that has a minimum of 10 to 15 μm, mean size diameter along with an optimum inter-spacing (≤5 μm) through the kink band width. The aperture stop of *f/4* was an appropriate selection for the amount of the light that travels through the lens to the image point to obtain the desired resolution. This particular aperture stop of *f/4* and the appropriate adjustment of the diaphragm (or ring) on the lens resulted in *15 mm by 15 mm* field of view, sufficient enough to capture the region with enough speckle dots. The picture taken with above mentioned parameters led to obtain 2560 pixels horizontally across the 15 mm as shown in figure 28, which may result in approximately 100 pixels across the kink band that should have an expected width of 600 μm.

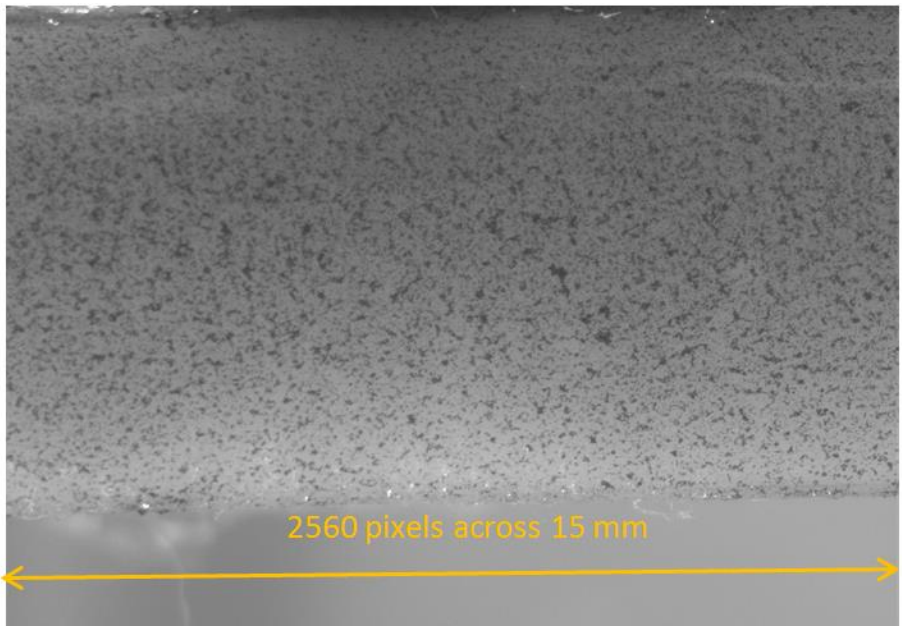

Figure 28. An Image Taken with EO 5MP Camera and Rodenstock 35 mm Lens Assembly to Capture Speckle Dots that has a Resolution of 2560 pixels Horizontally Across 15 mm Length.

The formation of the kink band is an unstable process and it was expected to develop on either side (left or right) of the load point application in 3-point bend. Therefore, an assembly of translation stages to move the camera along 3 axes was built to follow the kink band to allow studying the sequential events of the kink band formation during in-situ loading. The camera-lens system was placed on a v-block that was supported by the translation stage assembly (see figure 29). This entire assembly was placed in front of the load frame, and photographs of the sample were taken at different values of load during sample deformation. The resulting images were used to map the evolution of the sample displacement field as it went from undeformed (zero load) to deformed configurations (different values of loads during experiment). The camera-lens assembly

captured the movement of the speckle dots, and the DIC software, GOM ARAMIS™ used this information to calculate the strains within and around the kink bands.

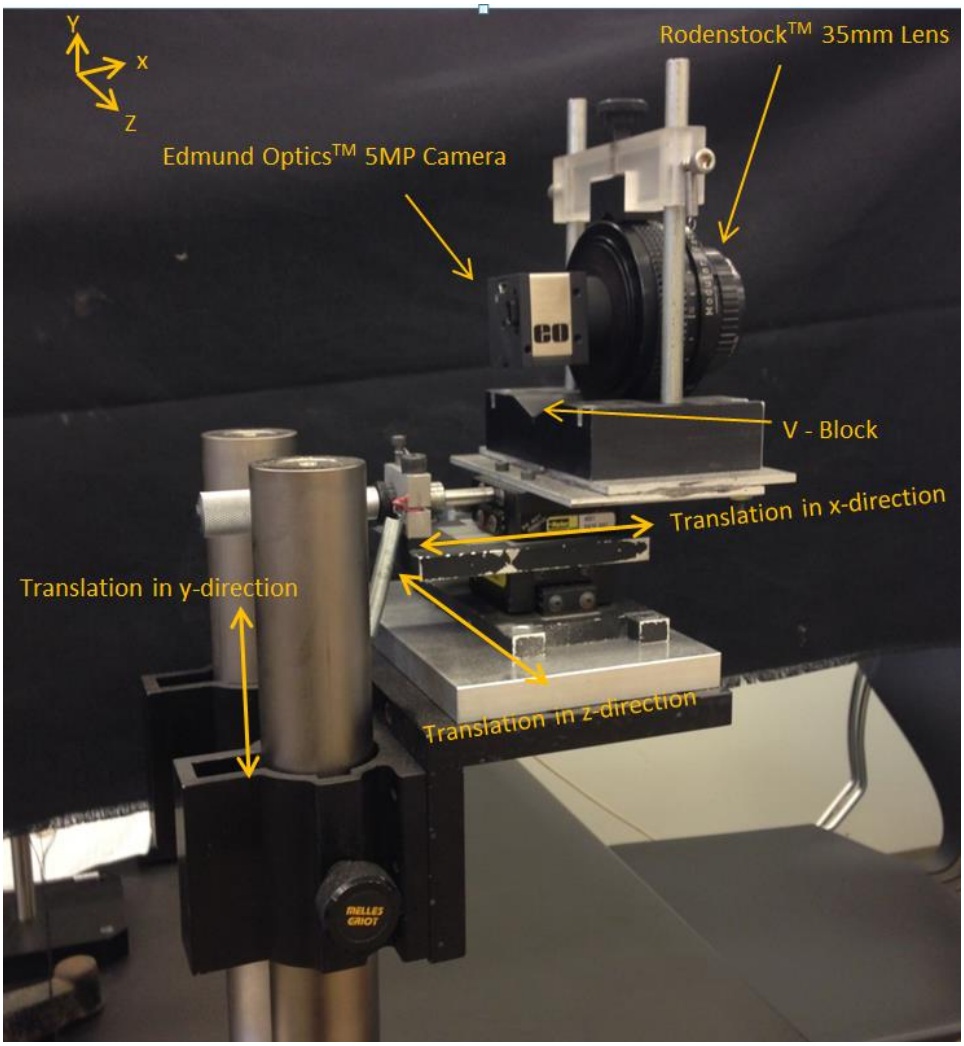

Figure 29. Camera-Lens Assembly with V-Block Supported on 3-Axis Translation Stages to Follow the Kink Band during the 3-Point Bend Test.

Procedural Steps in DIC software ARAMIS^{TM} for image processing

The first step was to rename the series of images taken during the experiment. The first image with zero load (undeformed configuration) was named as numeric "*0*" and the images thereafter were renamed as *1, 2, 3… and so on*, depending on the number of images captured. This series of renamed images were imported in the DIC software. The software processed the images and recognized in terms of stage numbers. For example, the image with name *0* was referred as stage 0 (reference or undeformed stage) and so on with increasing number. Once the number of stages was recognized, the next step was to mask the image.

There are certain parameters in ARAMIS^{TM} such as masking the image, facet size and facet overlap that directly relates to the accuracy of computing the displacements and strains using speckle dots [73]. The masking relates to the specific area of interest in the image to obtain displacements and strains. For, example in this study, the masking refers to region where the kink band is expected to pass through that specific region, by analyzing all images. That particular region was selected as a masking region, where the next step was to select the size of the facet and corresponding overlap to discretize the facet field within that masking region. The selection of facet size and overlap depends on the desired length scale of the region where the displacements and strains are of interest. Smaller facets correspond to higher data resolution as each facet corresponds to a data point during analysis. However if the facet size is smaller than ideal, the facet will be indeterminable and measurement accuracy will be compromised. [73]. For example, in the present study, an ideal size of *21 x 21* pixels with close to 50% overlap, i.e. an overlap of approximately

12 x 12 pixels in a *21 x 21* pixels window is required to achieve 100 pixels across the kink band width. This selection leads to obtain minimum of 4 facets across the kink band width, which is close to minimum to solve strains inside the kink band in UHMWPE composites. The displacement and strain accuracy refers to the stability of the center of each facet from stage to stage, in fractions of a pixel. There should be no movement whatsoever. The default setting of 0.04 pixels in ARAMIS^{TM} means that any data values which exceed the stated accuracy will not be presented or exported. As an example, for a 100 mm field of view, with 1280 pixels, each pixel is 78 microns. 0.04 pixels corresponds to 3.1 microns, which is below the stated accuracy of 3.3 microns. So, in the present case with 15 mm field of view, with 2560 pixels, each pixel is approximately 6 microns which is several magnitudes better than the default accuracy and acceptable to report by the software.

Once the facet field was assigned, the next step was to analyze the series of images in the evaluation module of the software. Different sections were created in different regions (where the kink band propagates) to extract the major strain and displacement jumps in x and y directions across the kink band width. All these results are discussed in detail in chapter 5.

Optical microscopy

Micrographs of the microstructure of Dyneema HB80 and Spectra Shield composites being tested were obtained using transmission optical microscopy with a Nikon ME600 microscope. The samples were obtained using a microtomy setup in a computer-controlled displacement stage equipped with a microtomy blade, so that samples

of the desired thickness (100-200 µm) could be obtained. Each slice was placed between two glass slides to prevent the thin material from curling during observation of the microstructure. After carrying out a 3-point bend test, some samples were also taken for optical analysis. Slices of the material at the bending point of the samples were cut with the microtome that were large enough to include the kink band and observed to document its inner structure. All the images were taken using optical microscope with objective lens that had 4X magnification and resulted in 100 µm resolution, approximately 2 microns/pixel.

4.1.3 Mode I Inter-Laminar Fracture Toughness

Interlaminar fracture toughness tests were carried out for each UHMWPE composite using a double cantilever beam (DCB) configuration in accordance with ASTM Standard 6671A [49] at 77 °F. Samples were machined by water jet as rectangular parallelepipeds with 10.57 mm thickness (*h*), 12.38 mm width (*b*) and 203.2 mm length (*L)*. Door hinges (Piano hinges as per the standard) were machined in house to be attached to the sample to provide a loading location 25.4 mm into the length of the sample. The basic geometry of the sample with loading location and pre-notch was followed from the protocol [49] as shown in figure 30.

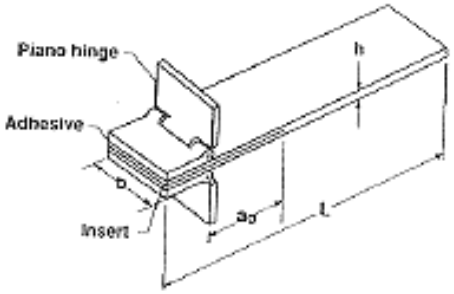

Figure 30. Double Cantilever Beam with Piano Hinges, where b = Sample Width, L = Sample Length, a_0 = Pre-Notch or Initial Delamination Length and h = Thickness of the Sample.

The hinges were attached using a two-part epoxy. A pre-notch was created using a microtomy blade at the geometric center of thickness of the beam to ensure the notch was in the middle of the specimen and a depth of 50.8 mm along the length, which resulted in.an effective of 25.4 mm (a_0) for the pre-notch. This value is important and had to be kept consistent throughout the testing to follow the protocol from [49] as closely as possible. The newly prepared samples were mounted in the load frame and clamped down using manual wedge grips. The test was carried out under displacement control with a displacement rate of 2 mm/min.

Figure 31 shows a DCB sample subjected to inter-laminar testing at room temperature. The test was continued until the crack reached the far end of the sample as to split it into two pieces.

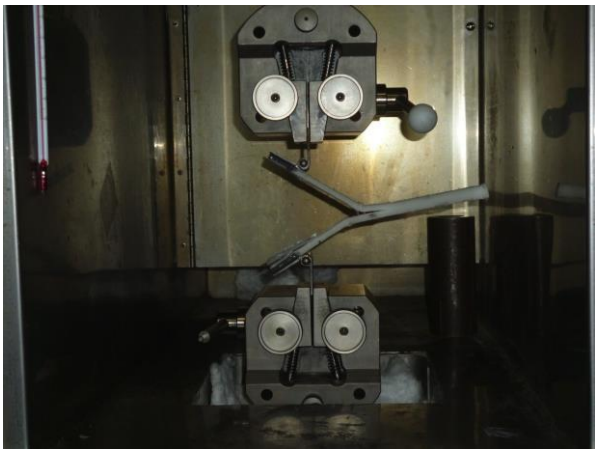

Figure 31. Interlaminar DCB test of a Dyneema HB80 Sample at Room Temperature.

Good adherence of the epoxy on the hinges was critical in this test. The bonding must be strong enough to withstand tensile stresses carried by the hinges. For this purpose, the hinges were roughened using a metal file to allow for better adhesion and a generous amount of the epoxy was applied. A curing time of 24 hours (more than the manufacturer's recommendation) was also used for all samples. By applying this procedure, the samples were able to withstand the needed amount of load until interfacial failure. Tests were successfully carried out at room temperature and the data were collected to determine the Mode I interlaminar toughness of the samples. The mode I fracture toughness G_{IC} was calculated as per the ASTM D5528-01 [49] standard using modified beam theory.

$$G_{IC} = \frac{3P\delta}{2wa} \tag{4.3}$$

Where P = load, δ = load-point displacement, w = specimen's width and a = delamination length.

4.1.4 Determination of Mode II Inter-Laminar Fracture Toughness

Mode I delamination is a common fracture process in polymer matrix composites. However, there is a strong possibility of mode II (in plane shear) contributions in the delamination failure, since the sample undergoes finite rotations during 3-point bending, and the interface is subjected to sliding [27, 74]. Hence, to understand mode II delamination fracture characteristics, additional tests were carried out in the form of pure shear - single lap joint (figure 32). The testing protocol "ASTM D3165 - Standard Test Method for Strength Properties of Adhesives in Shear by Tension Loading of Single-Lap-Joint Laminated Assemblies" [61] was followed as closely as possible. Through this test, the interface was sliding during the fracture event and the corresponding load-displacement profile was recorded to assess Mode II cohesive strength, which characterizes the onset of sliding of an interface.

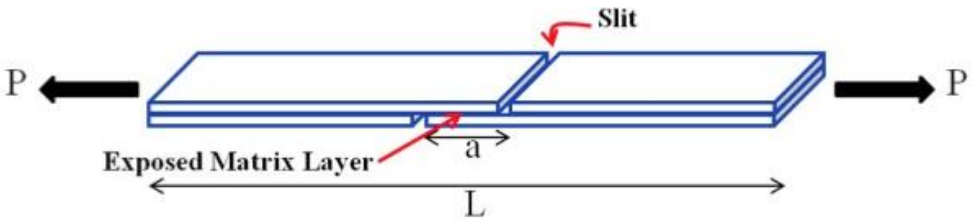

Figure 32. Single Lap Joint Test to Determine Mode II Cohesive Strength [28].

This testing idea was adopted from Prabhakar et al. [28]. The contact area – overlapped region of length "*a*" between adjacent plies (here 0 and 90 degree plies) was

susceptible to slide under uniaxial loading. The same samples, used for three point bending (refer to table 1 for dimensions) were modified, by cutting slits with the waterjet to get an exposed layer/interface affected zone of length *a*=12.40 mm by 10.57 mm wide (see figure 33 for more details).

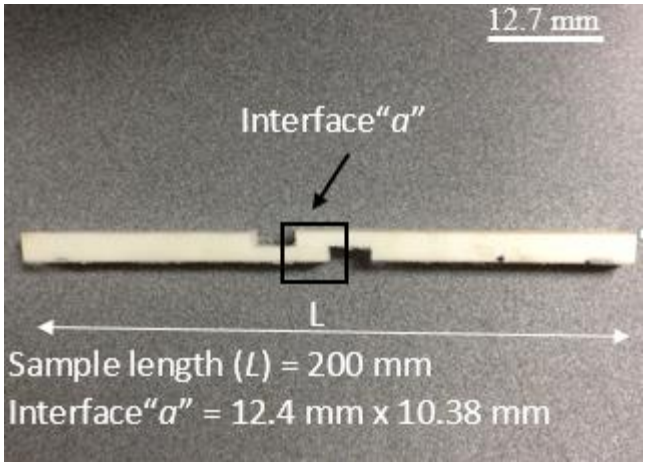

Figure 33. Exposed Interface Area, Which Was Subjected to Pure Shear When Loaded in Uniaxial Tension Test.

This exposed overlapped rectangular area as shown in figure 39 is barely one ply that was under pure shear by applying a uniaxial load to samples. The choice of the length of the overlapped region, *a = 12.40* mm was made as recommended in [61].

The peak cohesive shear strength characterizes the separation of the plies within the overlapped region. This peak cohesive strength was determined by recording the failure load (peak load) of the exposed shear area = *12.4 mm by 10.57* mm at which the separation occurs as described in [61].

4.1.5. Measurement of Large Deformation – Finite Strains

Previous reports [4, 8] suggest that material around the kink band deforms significantly, so the strain analysis it needs to be carried out using large deformation kinematics. Hence, large deformation theory is used here to measure finite strains expected within the deformation (kink) band. Actually, as per existing literature, the deformation inside the kink band is in terms of finite rotation as the plies inside the band rotate during the microbuckling process. Hence, a finite strain measure is obtained from the deformation gradient **[F]**. The deformation gradient maps the neighborhood of a material point in the undeformed (reference) configuration to the neighborhood of the same material point in the deformed configuration [31, 32]. The polar decomposition theorem implies that, physically speaking, the mapping performed by **[F]** can be expressed as a pure deformation followed by a rotation, or by a rotation followed by a pure deformation. Mathematically this is written as [31, 32]

$$[F] = [R][U] = [V][R] \tag{4.3}$$

Here R is an orthogonal rotation matrix, whereas U and V are symmetric positive definite matrices called the right and left stretch tensors, respectively.

According to continuum mechanics, a convenient and objective measure of finite strain is the Green – Lagrange strain tensor [E] that quantifies the changes in length of a material fiber per unit of reference length. The Green-Lagrange tensor can be expressed as follows:

$$E = \frac{1}{2}(F^T F - I) = \frac{1}{2}(U^2 - I) \tag{4.4}$$

4.1.6. Measurements of Major Strains from ARAMIS™

From [73], the strain measures ε_x and ε_y have the disadvantage of being defined as dependent on the coordinate system. This disadvantage can be eliminated by calculating major and minor strain values. The symmetrical matrix U can be transformed to the main diagonal form. The two eigenvalues λ_1 and λ_2 can be calculated as follows:

$$\lambda_{1,2} = 1 + \frac{\epsilon_x + \epsilon_y}{2} \pm \sqrt{\left(\frac{\epsilon_x + \epsilon_y}{2}\right)^2 - (\epsilon_x \cdot \epsilon_y - \epsilon_{xy}^2)} \tag{4.5}$$

Depending on the choice of the strain measure, the stretch ratios λ_1 and λ_2 can be transformed into corresponding strain values. Based on the larger eigenvalue, the major strain is determined (ε_1 or φ_1), and based on the smaller eigenvalue the minor strain (ε_2 or φ_2). The corresponding eigenvectors determine the two directions of major and minor strain. The strain values thus determined are independent of the coordinate system and are universally applicable. Based on this fact, the major principal strains have been extracted through the sections that pass through the kink bands. However, to report the actual strains inside the kink band the coordinate system has been rotated with x-axis being parallel to the kink band propagation direction. With respect to this coordinate system, the maximum

shear strains have also been extracted to determine actual material strains inside the kink band. All these results have been shown in DIC results of chapter 5 for both the composites.

4.1.7 Radius of Curvature of Kink Band in FEM

The radius of curvature from FEM model was calculated taking all data points and plot that as a function of true distance within the kink band region. The formula for the radius of curvature at any point x for the curve y = f(x) is given by:

$$\text{Radius of curvature} = \frac{\left[1 + \left(\frac{dy}{dx}\right)^2\right]^{3/2}}{\left|\frac{d^2y}{dx^2}\right|} \tag{4.6}$$

The radius of curvature gives insight in to the bending curvature of the plies, once the kink band is fully developed. This data has been compared with the micrographs of the deformed samples of both the UHMWPE composites. Moreover, it can also provide details in parametric study about the effect of bending curvature with increasing no. of plies.

4.2 Modeling Techniques

4.2.1 Micro-buckling model with microstructurally explicit plies

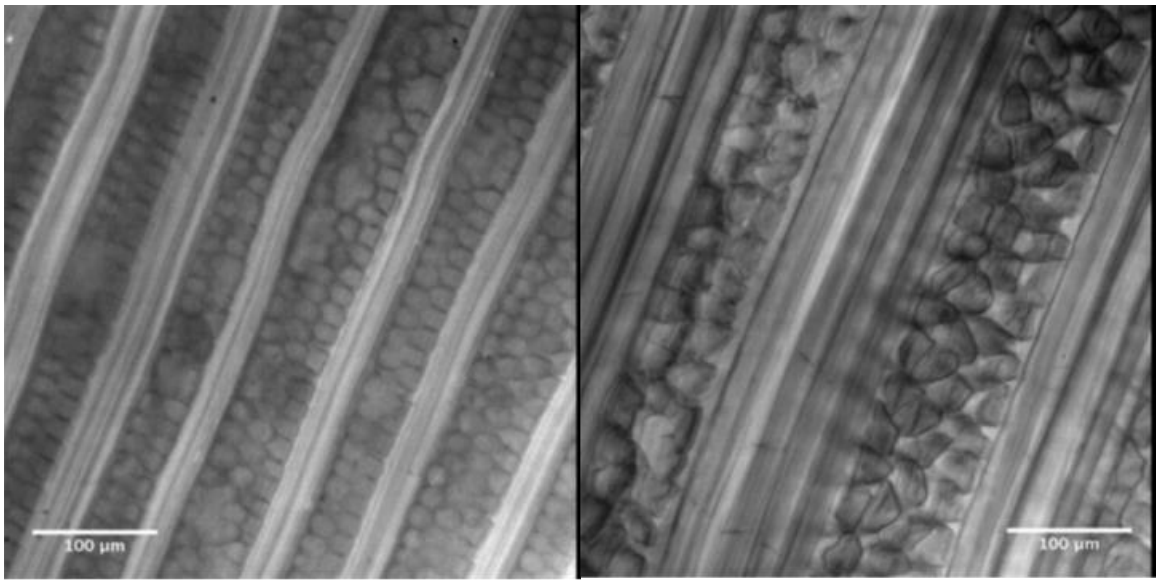

(a) (b)

Figure 34. (a): Micrograph of Dyneema HB80 Sample, Thin Plies (b) Micrograph of Spectrashield Sample, Thicker Plies as Compared to Dyneema HB80.

The UHMWPE composites, Dyneema HB80 and Spectrashield used in this study are cross-ply laminates $[0/90]_s$ as discussed in previous sections. From the microstructure study (see figure 34), note that Dyneema HB80 has thinner plies and spectra shield has thicker plies. Further characterization confirmed that Dyneema HB80 consists of 264 plies and spectra shield consists of 152 plies with a same beam height of 10.57 mm.

A 2-D micro-structurally explicit finite element model is implemented to simulate the global response, i.e., load vs. displacement during testing, while also capturing the strains inside and around the kink band. Note that, the kinking instability is caused by fiber

micro-buckling, so the analysis has been carried out to capture localized buckling of plies near the vicinity of the load application point.

In order to capture the expected localized buckling of plies, a Riks step is used, such that an arc-length solution scheme is adopted [28, 75]. This method is able to follow the unstable equilibrium paths that can occur at bifurcation points. During the 3-point bend test, the load-displacement profile is expected to follow an oscillating path, i.e., peaks and valleys are observed in the experimental data in [27]. They may correspond to the onset and development of buckling instabilities during loading.

To make the model fully microstructurally explicit, a cohesive zone is incorporated in between the 0° and 90° (off-axis) plies. So, for 264 plies which is a case of Dyneema HB80, 263 cohesive zones have been embedded in between the plies. Similar approach has been followed to make the microstructurally explicit model for Spectra shield too. An example of generalized 2-D model, representing the plies and cohesive zones and imperfection region, where the kink band is expected to nucleate and propagate near the vicinity of the load application point at the center of the node as shown in the figure 35.

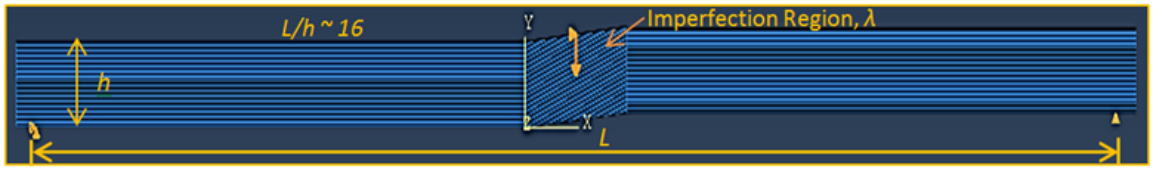

Figure 35. Microstructurally Explicit Model with Boundary Simply Supported Conditions

It has been postulated in [75-77] that in ABAQUS, fully integrated first order 2D elements such as plane stress, CPS4 and plane strain, CPE4 may manifest shear locking and their reduced versions, such as CPS4R (plane stress reduced) and CPE4R (plane strain reduced) may manifest hour glassing under bending. The same references [75-77] also suggest to use higher order (second order) reduced integration elements to avoid hour glassing under bending, but they are computationally expensive. The literature in [76-81] suggests using incompatible version of 2D or 3D solid elements to capture bending accurately to avoid shear locking. For example, one incompatible element through the thickness is sufficient enough to capture the bending as accurate as using four reduced order elements (CPS4R) through the same thickness.

Using more elements may lead the simulations to be computationally expensive, so the choice of the incompatible elements was considered a better trade-off, especially modeling microstructurally explicit plies under bending, which is a current focus of this research. Therefore, keeping all the above critical things in to consideration, only one plane stress incompatible element (CPS4I) per each ply thickness is used. The cohesive zone that represents the interface between each 0° ply and 90° ply is modeled with four node cohesive elements (COH2D4) as offered in ABAQUS elements library. Reviewing the section of finite element modeling in chapter 2 does suggest that the ply misalignment angle or fiber misalignment angle characterizes an imperfection in the model (and in the actual material) that triggers nucleation of the kink band. Therefore, to capture the kink band in the current microstructurally explicit model, a bigger imperfection region, λ,

approximately twice the height of the beam *h*, ($\lambda \sim 2h$) with misalignment angle Φ varying between 3° to 5° has been considered as shown in figure 36.

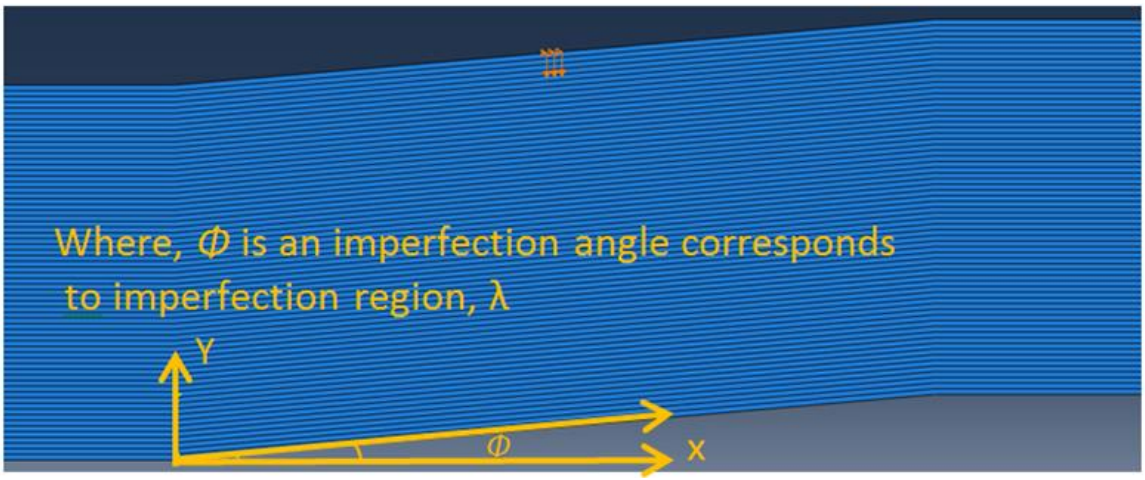

Figure 36. Imperfection Angle Φ Within the Imperfection Region λ (Magnified Inclined Portion)

The choice of misalignment angle Φ between 3° to 5° is enough to trigger microbuckling as indicated in literature review. From a review of literature survey done in chapter 2 and in more particular [27, 63], any ply misalignment angle/imperfection angle of 3° to 5° characterizes an imperfection in the model (and in the actual material) that triggers nucleation of the kink band to simulate the global response as close as experiment. The higher misalignment angle other than this does not change the results significantly. Knowing this fact, imperfection angle ≤ 5° has been considered in all simulations for both the materials.

Note that, this is the particular region where the kink band is expected to get arrested as a result of the simulation. Therefore, a mesh design is a key factor and it needs to be refined appropriately in the imperfection region, which is an area of interest. The mesh everywhere else, outside the misalignment/imperfection region needs to be relatively coarse as compared to the imperfection region. Doing so would result in reduced number of overall elements in the model and hence makes the simulations computationally least expensive vs. using the same uniform mesh for the entire model. To implement the appropriate mesh design as explained, a mesh biasing technique has been used, such that the imperfection region has a uniform refined mesh (same mesh density) and in all other regions, the mesh density decreases (coarse mesh) progressively as shown in figure 37.

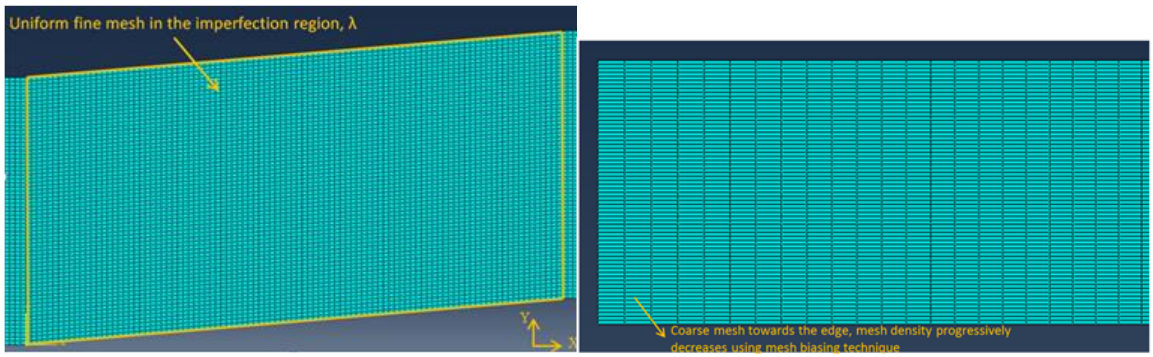

(a) (b)

Figure 37. (a) Uniform Fine Mesh Density in the Imperfection Region (b) Coarse Mesh Towards the Edge/Boundary of the Model.

Material Properties and Ply Configuration

From [27, 43], note that, the microbuckling response is a result of elastic bending of plies and plastic shearing of interfaces. Knowing to this fact, the plies in the current model has been given a more simplified material assumption, purely isotropic elastic

material (Young's modulus same in all directions) incorporated in the model in a cross-ply configuration [0˚/90˚/0˚].

Cohesive Layers: Traction-separation law for mixed mode deformation and failure, where the plasticity and non-linearity has been embedded in cohesive zones.

Elements Library: Incompatible continuum elements, CPS4I

Cohesive Elements: Four node cohesive elements, COH2D4.

The material properties have been given in such a way that it facilitates a stiff ply (0 degree ply) to buckle first near the vicinity of load point application and the ply below it – 90 degree, follows the 0 degree ply. Boundary conditions have been applied, such that the model replicates the similar configuration of simply supported beam following the experiment as shown in figure 25. The nodes (pinned at one end and the roller at the other end) have been fixed such that the supported length matches the aspect ratio of $L/h \sim 16$ as close as possible in the experiment.

The primary and initial goal is to calibrate the global response, load vs. displacement during the 3-point bend test, which will be obtained during experiment for both the Dyneema HB80 and Spectrashield. The calibration of the finite element model requires two important considerations as follows:

1. Estimation of Young's modulus of 0 and 90 degree ply from effective elastic/flexure modulus, calculated from 3-point bend experiments, following classical theory for laminated composite beams [64].

2. Peak cohesive strength and fracture toughness values for Mode I and Mode II delamination from experimental data and its implementation in cohesive zone modeling.

The composite beam's effective Young's modulus derived from flexure gives an idea about bending stiffness under 3-point bending within the elastic regime. The young's modulus of 0 and 90° plies has been calculated, such that the combination yields effective Young's modulus of $E_{Dyneema/eff}$ = 6500 MPa, measured from experiments. It is known, from laminated composite beam theory for cross-ply laminates [64] that the stiffness contribution of off-axis plies under bending is significantly lower than the 0 degree plies. So, to do further analysis for kink band evolution, the effective modulus of Dyneema HB80 is varied between 6500 MPa (same as effective flexure modulus of beam) to 20000 MPa at 6500 MPa, 10000 MPa and 19000 MPa and used as the corresponding Young's modulus of each 0 and 90 degree ply to make look the effects on the flexure response of the composite beam.

Similar consideration has been given in estimating mechanical properties of plies for Spectrashield. The micrographs of Spectrashield specimens show thicker plies as compared to Dyneema HB80 as shown in figure 34 (b). This is bound to make noticeable difference in finite element simulations. Laminated composite beam theory has also been applied in this case to determine the corresponding Young's moduli of the 0 and 90° plies in Spectrashield that are consistent with the effective modulus obtained from the flexure, experiments. In this case, the effective modulus of spectra shield, $E_{Spectrashield/eff}$ = 5000

MPa is varied between 5000 MPa (same as effective flexure modulus of beam) to 10000 MPa (twice the effective modulus of beam), at 5000 MPa, 7500 MPa and 10000 MPa and used as the corresponding Young's modulus of each 0 and 90 degree ply to make look the effects on the flexure response of the composite beam.

Effects of non-linearities in the material model have been taken into account by including inelastic strain using the mix mode traction separation law in cohesive zones that represent the interfaces between 0° and 90 ° plies as explained in chapter 2. The finite element study in [27, 63] does suggest that the microbuckling response is a result of elastic bending of plies and inelastic shearing of interfaces. Moreover, the implications of several results available in the literature [8, 23, 27, 28, 47 and 63] also suggest that modeling of fiber kinking /microbuckling may not require consideration of plasticity at the constituents such as ply or fibers as the influence on the response is untraceable. Most of the permanent deformation can be explained by sliding and separation of interfaces rather than plasticity of the plies. This motivates incorporating the plasticity in the cohesive zones (represent the interfaces) in terms of traction–separation law as explained in preceding sections.

The aforementioned discussion on estimation of mechanical properties of plies and interfaces can be a stepping stone to calibrate the mechanical response for both the materials. However, the calibrated models may not shed light on capturing the physics behind the sensitivity of the microbuckling response. This motivates performing a parametric study. The objective of the parametric analysis is to understand qualitative and quantitative effects of key variables on the behavior of fiber –reinforced PMCs via the use of the microstructurally explicit model, and use this understanding to make meaningful

comparisons with the results obtained from 3-point bend experiments and DIC measurements. Moreover, it can give additional insight into the material and geometric parameters that influence the mechanisms controlling kink band evolution and their relationships with failure.

The following parameters and constraints have been varied to do a parametric study with the model for both materials, while keeping the simulations cost effective.

1. Increasing the effective Young's modulus of Dyneema HB80 and Spectra Shield, measured from flexure test and hence the corresponding ply properties for 0° and 90° plies. Note that the calibration part has a close resemblance with this test case.
2. Increasing or decreasing the peak cohesive strength and fracture toughness for Mode I and Mode II delamination fracture, other than the calibrated values from calibrated models (one above and one below). This leads to two different cases for each model.
3. Variation in imperfection region, λ, (i) $\lambda=h$ and (ii) $\lambda=2h$, where h is the height of the beam. This leads to two different cases for each model.
4. Variation in imperfection angle, ϕ for 3° and 5° that leads to two different cases for each model.

The parametric study has been done only on 33, 42 and 66 ply models to capture the physics of changing the above-mentioned variables as the same study with 264 plies (a

case for Dyneema HB80) and 152 plies (a case for Spectra Shield) would be computationally expensive. Results for all these cases are presented in chapter 5.

4.2.2. Cohesive Zone Modeling of Mode I Delamination

A 2-D finite element model has been calibrated using Mode I delamination fracture testing. The interface has been modeled using a surface based cohesive zone with 4-node cohesive zone elements and the bulk material outside the interface has been modeled with plane stress solid (continuum) elements. It has been reported [44] that surface based or node based cohesive zone approach gives the same behavior and results.

Figure 38 shows the model parameters with boundary conditions. The red highlighted region corresponds to an interface and the solid blue region corresponds to the bulk material. An initial crack (delamination length) of approximately 25.5 mm has been used, following the experiment. Two important constitutive laws have been adopted here to simulate appropriate behavior. The bulk material is modeled with homogenized lamina –equivalent isotropic material properties and the cohesive zone is modeled with a cohesive law (traction-separation) that captures spontaneous crack initiation and growth. For this purpose, parameters associated with maximum damage criterion and damage evolution have been selected. Alfano's [29] work suggests tuning the governing parameters; σ_c – Peak stress and G_{IC} - fracture energy to get the correct behavior of the interface. With respect to the 2-D model, four node plane stress elements, CPS4 in a bulk material section

and four node cohesive elements, COH2D4 in a cohesive zone have been specified from the Abaqus™/standard element library.

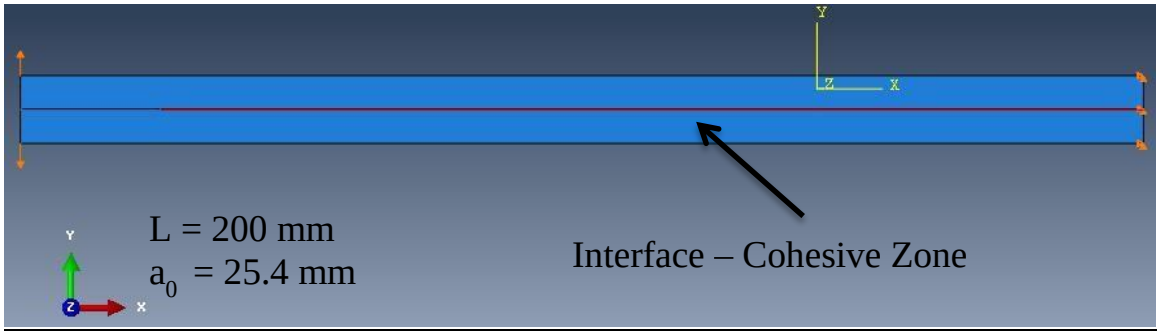

Figure 38. Cohesive Zone Modeling of the Mode I Delamination Fracture Test

Results from these models have been compared with the experimental data. The primary goal is to match the peak load at which the crack initiates and grows along the bond line.

4.2.3 Cohesive Zone Modeling of Mode II Delamination

Figure 39 shows the model parameters with boundary conditions for the model used to simulate the mode II delamination test.

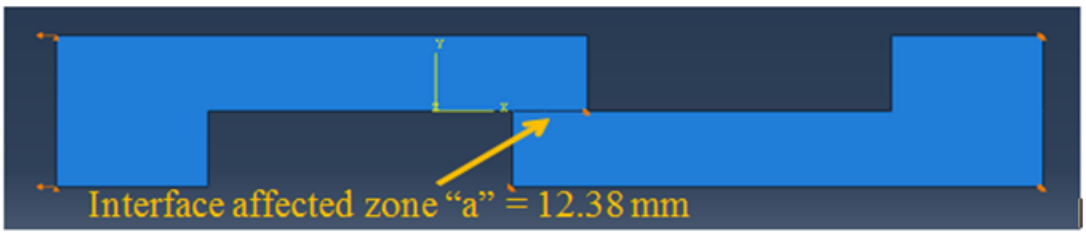

Figure 39. Cohesive Zone Modeling of Mode II Delamination Fracture

A similar approach as that used for Mode I has been adopted to model Mode II fracture. As explained in previous sections, the contact area – overlapped region of "*a*" between adjacent plies (0 and 90° plies) is susceptible to slide under uniaxial loading. This overlapped rectangular area has been modeled as a bond line between two adjacent plies, following the experiment. The cohesive elements (COH2D4) have been embedded into this bond line, referred to a cohesive zone/interface affected zone under pure shear. The traction separation law has been implemented within the cohesive zone to capture spontaneous crack initiation and growth. The bulk material is modeled with isotropic material properties and 4 node plane stress elements (CPS4).

Similar implications from Alfano's work [29], such as σ_c - peak stress and $G_{IIC,}$ critical fracture energy in shear one direction (pure shear), following the experiments have been applied to cohesive zones to get the correct physical behavior of the interface.

Simulations have been compared to the experimental data, more importantly the peak load, where the separation between the plies occurs. All results have been discussed in the following chapter 5.

5. RESULTS AND DISCUSSION

This chapter focuses on a detailed description and discussion of results obtained through experiments and finite element modeling. The experimental part in particular, focuses on the results of 3-point bend tests (flexure) conducted on both UHMWPE composites used in this work along with DIC. There were load-oscillations observed during the flexure test in both materials. The explanation behind these load-oscillations, micro-mechanisms, is the primary aspect of the hypothesis formulated here and that has been discussed with DIC and finite element modeling results. The microbuckling model captures the physics behind these load-oscillations and reproduces the formation and interaction of deformation/failure mechanisms that have been observed in the experiments as a result.

The formulation of the microbuckling model requires the cohesive zones that represent the physical interface between the plies, 0° and 90 ° in this study for both the materials. Therefore, the criteria used to select the appropriate mechanical properties of the interface through Mode I and II delamination fracture tests have been explained as well as the process used calibrate finite element models. With respect to material characterization, optical microscopy has provided details on the microstructure of both the UHMWPE composites, i.e., configuration of plies and cross-section of the fibers. Moreover, the post mortem study has also elucidated details and provided the direct evidence of localization of strain on the sample surface (both samples), forming a kink band and delamination (axial splitting of fibers/plies).

5.1. Three Point Bending Test and Digital Image Correlation (DIC)

5.1.1 Three Point Bending and Corresponding Load-Displacement Curves

Three-point bending testing was a stepping-stone to study deformation and failure mechanisms in unidirectional fiber reinforced UHMWPE composites under stress gradients. From [27], note that, there were some load-oscillations observed during the bending tests in cantilever configuration, but unfortunately, there is no explanation addressing the physics behind these load-oscillations indicating the deformation/failure mechanisms under stress gradients. In the present study, during the 3-point bend tests, a similar type of load-deflection curves (peaks and drops) have been observed. An illustration of the load vs. displacement curves for three-point bend tests is shown in figure 40 for Dyneema HB80 and Spectra Shield samples.

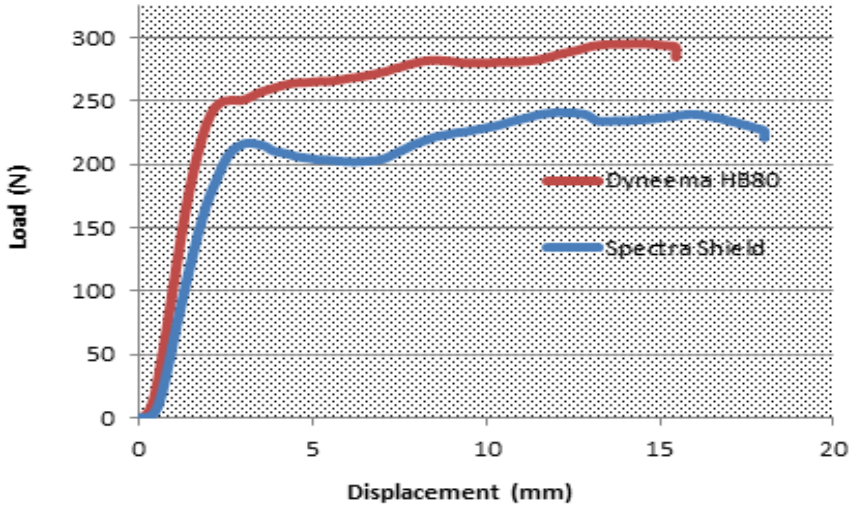

Figure 40: Load-Displacement Data for Dyneema HB80 and Spectra shield Samples Tested At Room Temperature.

The detailed analysis and prediction of these load-oscillations based on micromechanisms of deformation at the ply level is a primary aspect of the current work. The understanding of potential deformation/failure mechanisms behind these load oscillations is one of the main objectives of this research and that has been supported by the DIC results. Referring to figure 40, note that both UHMWPE composites show peaks and drops in the load-deflection curves. Note that, that the first peak load of Dyneema HB80 is approximately 2 % higher than Spectra Shield in bending. The entire area under this load-deflection curve corresponds to the toughness of the material. So, in this case, Dyneema HB80 is tougher than Spectra Shield. This difference in the global response and hence the toughness is consistent with a distinct variation of their microstructures (see figures 34a and 34b).

The current hypothesis to explain this behavior is that during three point bending, referring to the load-deflection curve, at the first peak load, the ply (or set of plies) that is in contact with the loading pin buckles due to compressive stresses. Upon a buckling event, that particular ply (or set of plies) loses its (or their) compressive load bearing capacity, which directly reduces the inertia of the cross-section and results in the load drop observed during the test, since the compressive strain needed at those plies to accommodate the curvature of the beam can now be carried through local bending of the buckle plies at much lower loads. However, with an increased displacement and bending of the beam, the adjacent plies (lower down the thickness) start to offer resistance to bending, which result in a rise of the compressive load as a subsequent peak is reached, leading to a new buckling event. The process of buckling and bulging of plies triggers the formation of the kink band,

which is a result of plastic microbuckling, as the buckled plies will lead to the local rotations that define the kink band. Load transfer across the plies, as described above, will continue the process and propagate the band. The process of subsequent buckling events continues until the kink band leads to delamination. At the final delamination, the structure completely loses its flexural stiffness. The quantification of this process, along with the confirmation of the hypothesis described above, is an important aspect of this work and the finite element study would give additional insight into the micro-mechanisms involved on load-oscillations.

The deformed Dyneema HB80 sample is shown in the figure 41. Localized buckling and bulging of plies were observed near the load application point.

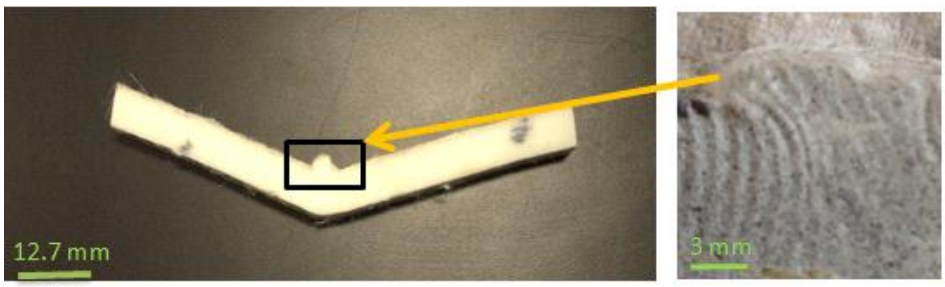

Figure 41: (a) Dyneema HB80 Sample After 3-Point Bend Test (Lower Magnification). (b) Bulge at Higher Magnification.

A similar deformation mode was also observed on the Spectrashield specimens. This localized buckling triggered the kink band formation (plastic microbuckling) from the compression side, which then propagated to the tension side of beam. The confirmation of this observation (another part of the hypothesis) and analysis is supported by DIC results, as discussed in the next section.

5.1.2 Digital Image Correlation Results for Increasing Loads

The predictions in the hypothesis behind these load-oscillations have been formulated and explained in the previous sub-section. The confirmation of the same has been illustrated with 3-point bend observations along with DIC. During the test, the first peak load induces a kink band to initiate from the compression side (near the vicinity of the point where load was applied through a pin), which then propagates towards the tension side of the beam with subsequent load oscillations. At this particular instance, the primary focus was to visualize the kink band initiation and its full development during the load-oscillations observed in the 3-point bend test. It was observed that within a second subsequent peak load, the kink band was fully nucleated and hence, the test was stopped after two subsequent peak loads.

Additional 3-point bending tests were carried out along with DIC to find the strains inside the kink band during its evolution up to two subsequent peaks (pointed out with two red circles) using the stages shown in figure 42 for Dyneema HB80. Note that, the distinct drops here are not the same as they were observed in figure 40. The drops in figure 42 correspond to the point of the pause of the test as the camera-lens assembly needed to be moved to follow the propagating band with further bending. After re-starting the test, the data acquisition continued recording the corresponding loads and displacements with further bending of beam, from the last point where it was paused.

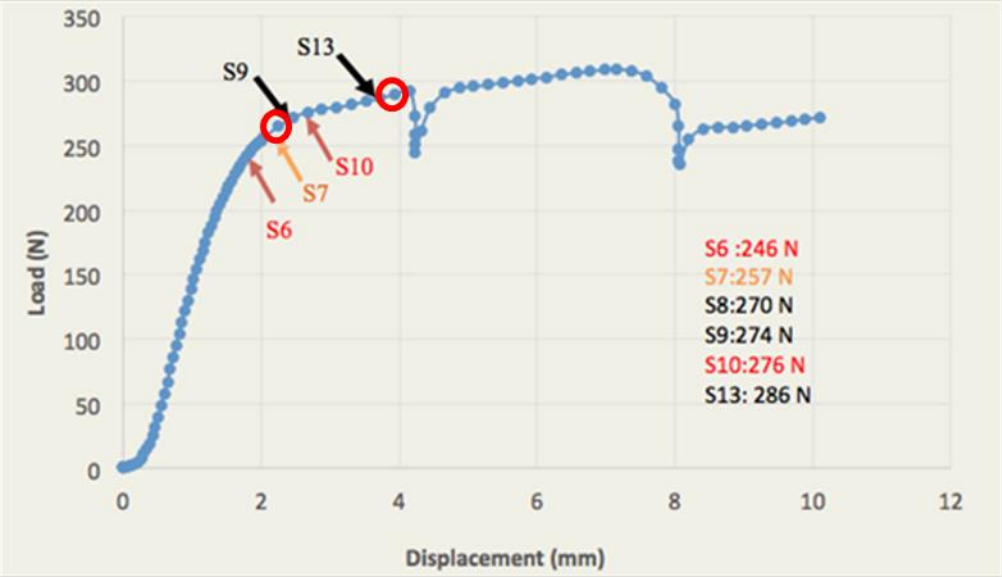

Figure 42: Load-Displacement Curve During 3-Point Bend Test for Dyneema HB80; Where the Letter S Stands for Different Stages of the DIC Measurement at the Loads Shown in the Inset.

Images were captured at zero load and also as load increased, with particular emphasis at the first two subsequent peak loads to visualize the development of the kink band from the compression side of the beam.

A similar procedure was applied to visualize the kink band nucleation and evolution on Spectra Shield specimens. The corresponding three point data along with the DIC stages and their loads are shown in figure 43.

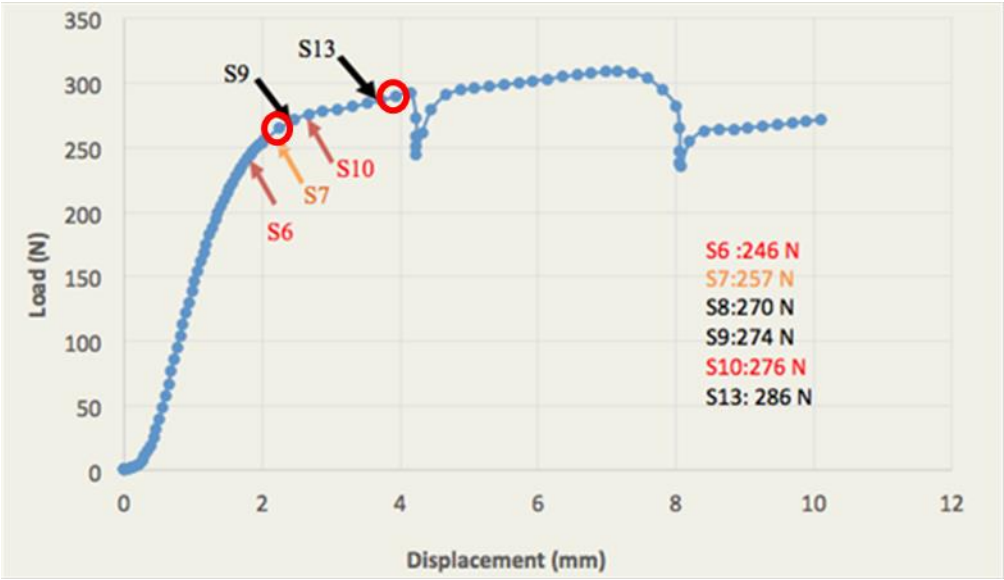

Figure 43: Load-Displacement Curve During 3-Point Bend Test for SpectraShield; Where the Letter S Stands for Different Stages of the DIC Measurement at the loads Shown in the Inset.

Note that, the drops in figure 43 are not the same as they were observed in figure 40. The same explanation for the Dyneema HB80 also follows here in case of Spectra Shield.

5.1.3 DIC Results

The series of images captured during the 3-point bending tests on the side surface of beam samples (Dyneema HB80 and Spectra shield) were further processed using DIC software to determine the displacements and strains within and around the kink band. Variables of interest that were extracted from the DIC results include displacement jumps (X and Y directions) across the kink band and major principal strains (%) inside and around it, as the band evolved during the sample deformation. Different sections were

created to determine the corresponding values of displacements and strains with the desired resolution and accuracy. The resolution of the DIC is based on the number of facets within the interested region. So, for example, a width of the kink band is a region where the sufficient number of facets passes through during the DIC analysis steps to resolve the accurate displacements and strains. In this case, looking in to the length scale of the kink band (a range of 500µm to 1000µm) the resulting resolution has at least 4 facets across the kink band.

An example of the different sections on the region of interest of the sample surface is shown in figure 43. It shows 4 different vertical sections drawn on the plane of the measurement. The blue square grids correspond to the facet fields, which have been explained in the chapter 4. For example, this image (reference stage) has been taken at zero load and the sections have been created to evaluate the variables of interest within the specific region. In this case, the kink band is an area of interest on the sample surface to extract the variables of interest. It can be presumed that the band may nucleate between the sections 2 and 3, as they surround the point of application of the load.

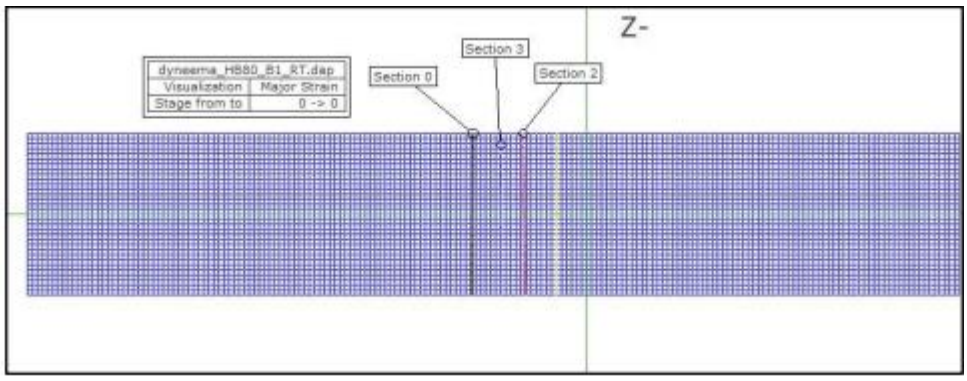

Figure 44: Reference Stage at Zero Load Condition and 4 Different Sections on the Region of Interest from ARAMIS^{TM} Software.

DIC Results for Dyneema HB80:

Figures 45-47 shows the process of kink band evolution in Dyneema HB80 specimen from stage 9 to stage 11 as portrayed through the DIC results. Stage 9 in figure 45 shows the nucleation of the kink band from the compression side of the beam where the loading was applied. Note that section 0 (black line) has displacement jumps both in X and Y directions, which indicates a kink band has nucleated and started to propagate. The major principal strain recorded for stage 9 is approximately 8% through section 0 and 6% through section 1 as shown in fig. 45 (d). As the kink band propagates through stages 9 to 11, a noticeable difference in displacements and major principal strain has been observed. Stage 10 (figure 46) shows a principal strain of approximately 16% through section 1, which indicates an increase of about 100% in the major principal strain between stages 9 and 10 at the same corresponding section, for an increase of displacement of only 8.5% and actually a small decrease in load. Comparing stages 9 and 11 (figure 47), note that the principal major strain increases from 8% to 24% through section 0, i.e., a 300% increase on strain.

The above results clearly indicate the presence of a kink band during sample deformation under bending, presumably triggered by plastic microbuckling. Note that, close to the peak load in stage 9, the band has already nucleated. This supports the hypothesis that the nucleation event of kink band occurs close to the peak load that is a result of plastic microbuckling and hence the localization of these principal strains inside the band is indirect evidential proof of microbuckling.

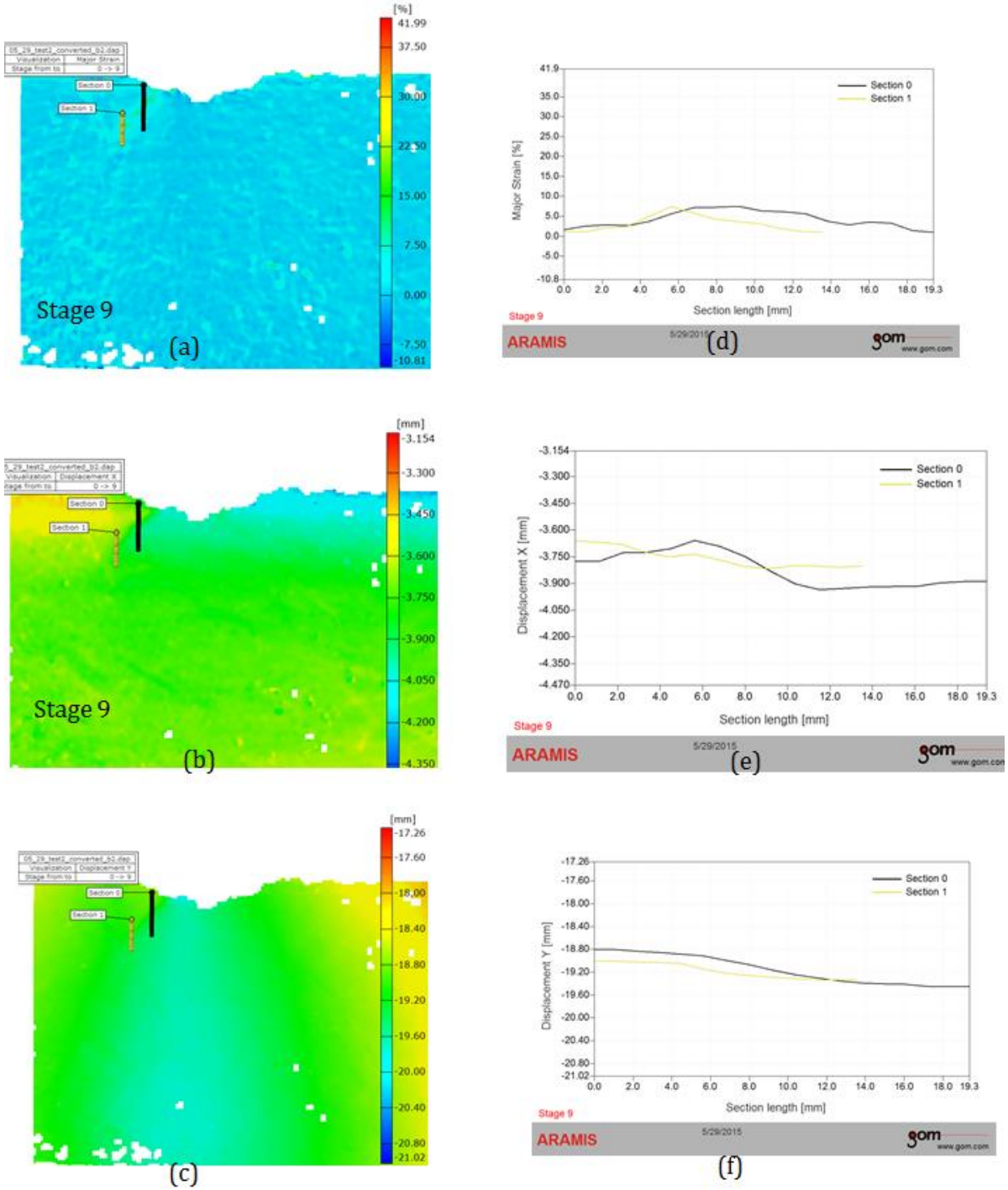

Figure 45: (a-c) Left: Location of Sections for Stage 9 to Extract Major Principal Strain, Displacement-x, and Displacement-y; and Its Corresponding Profiles Along the Same Sections, (d-f) Right Respectively.

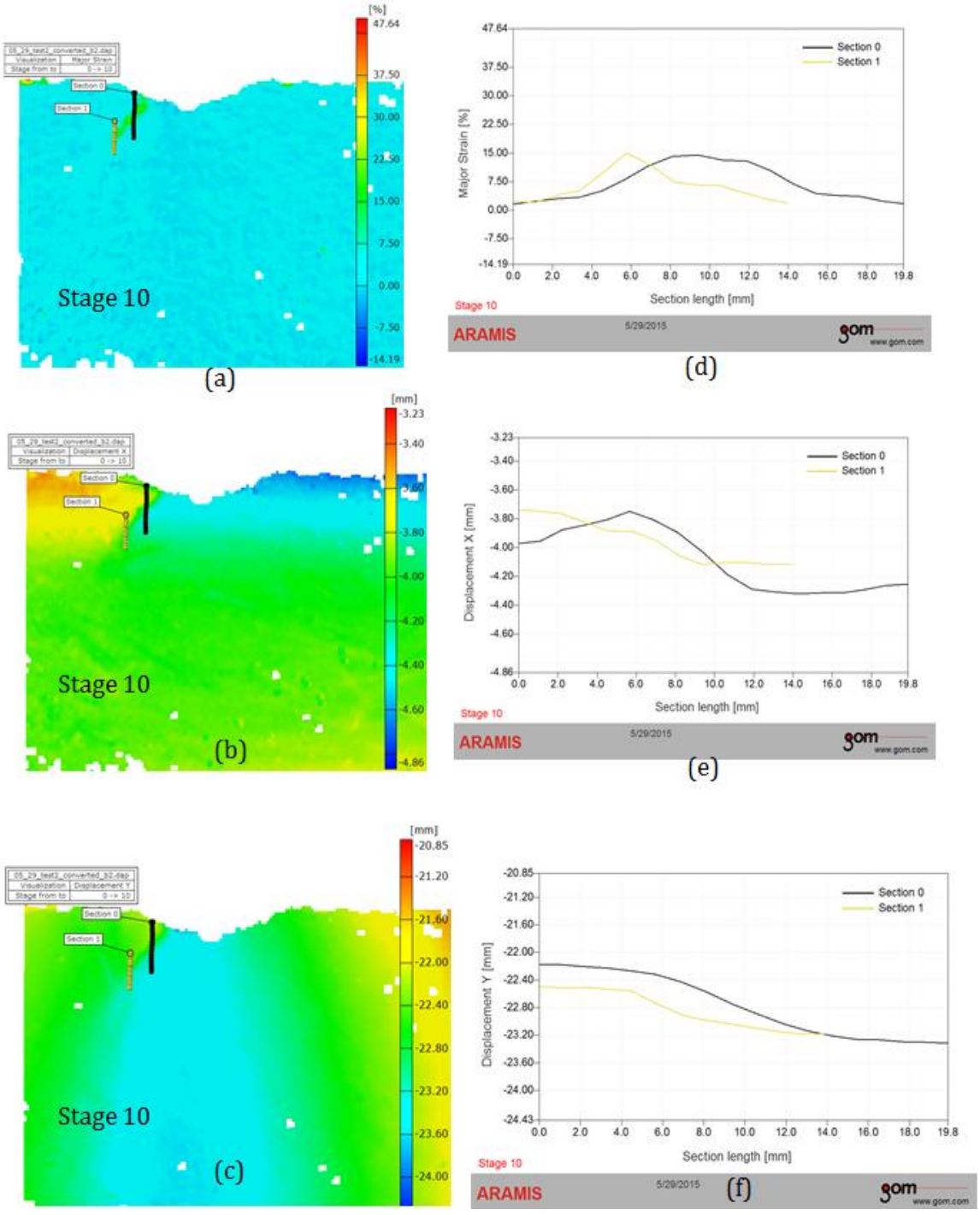

Figure 46: (a-c) Left: Location of Sections for Stage 10 to Extract Major Principal Strain, Displacement-x, and Displacement-y; and Its Corresponding Profiles Along the Same Sections, (d-f) Right Respectively.

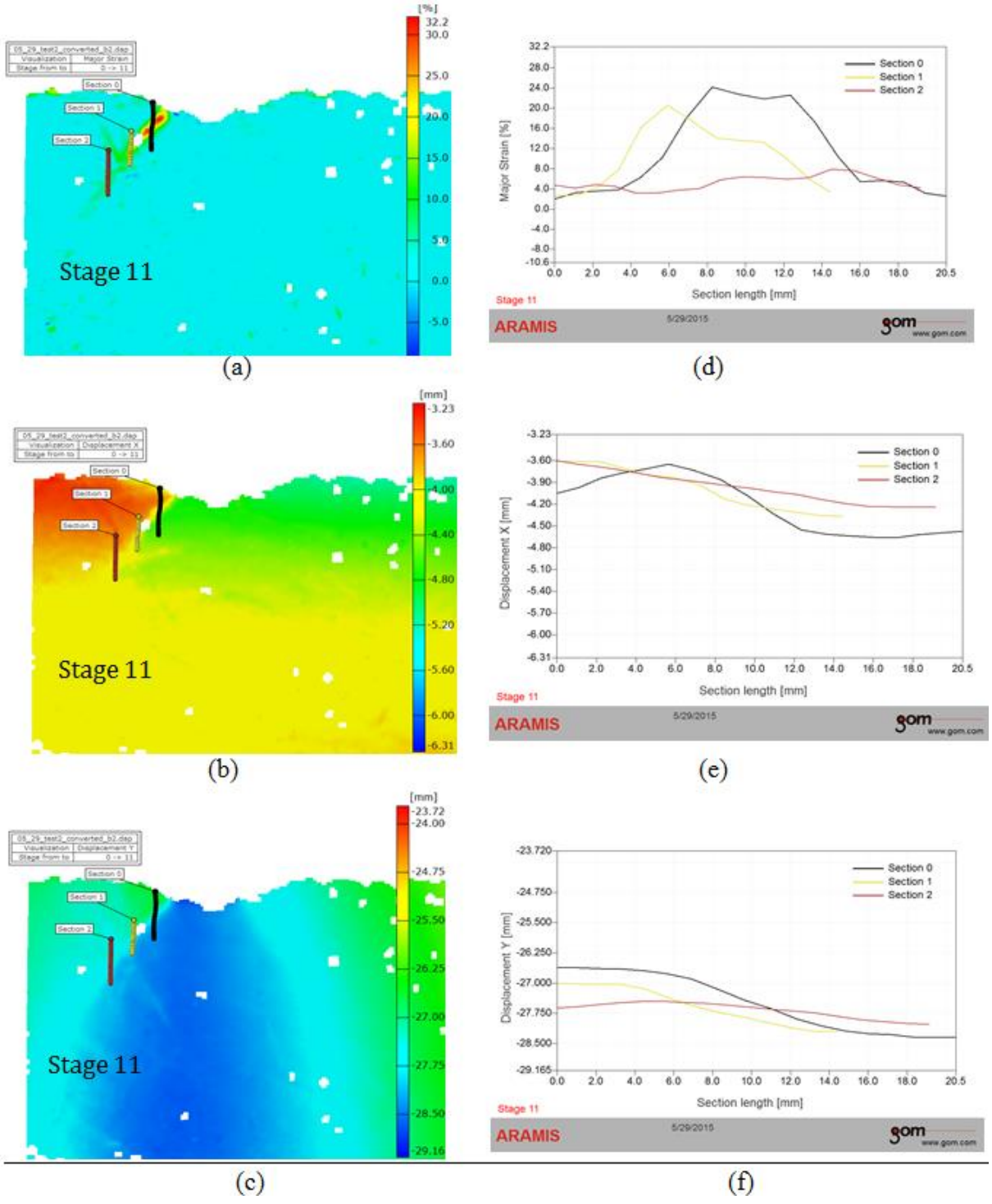

Figure 47: (a-c) Left: Location of Sections for Stage 11 to Extract Major Principal Strain, Displacement-x, and Displacement-y; and its Corresponding Profiles Along the Same Sections, (d-f) Right Respectively.

Note that, the principal strain in all subsequent stages for both the sections 0 and 1 increase with further bending of beam (see figure 48).

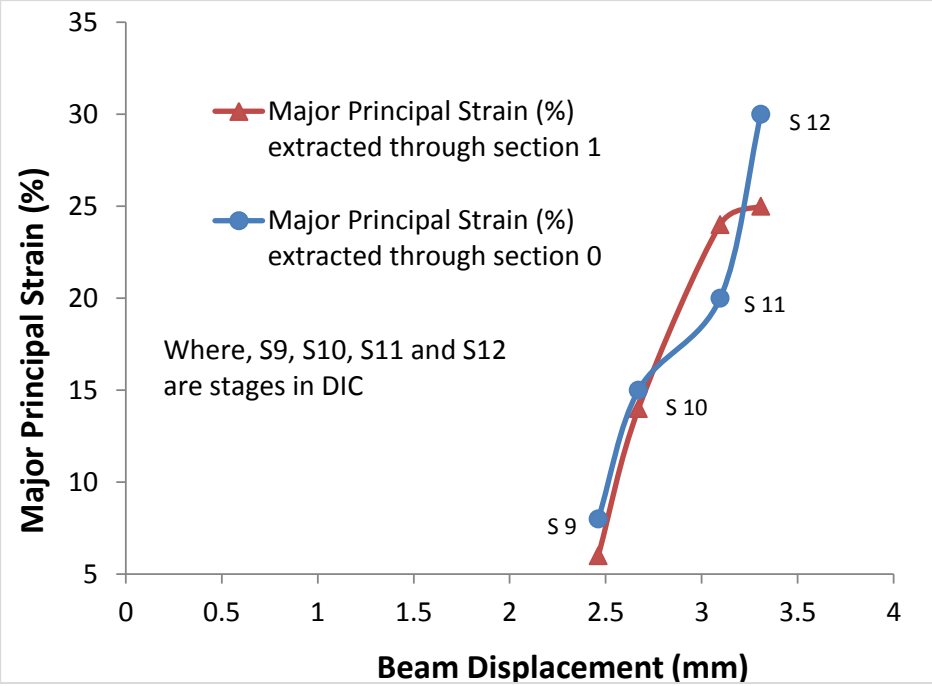

Figure 48: Major Principal Strain (%) vs. Beam Displacement From Stage 9 to 12 Extracted Through Sections 0 and 1.

Referring to all subsequent stages, note that, there is a significant displacement jump in the x direction (see figure 49) as the kink band propagates from stage 9 to 12. This indicates that the propagating kink band produces a significant amount of shear strain. With further propagation of a band, the maximum principal strain across all the defined sections increases.

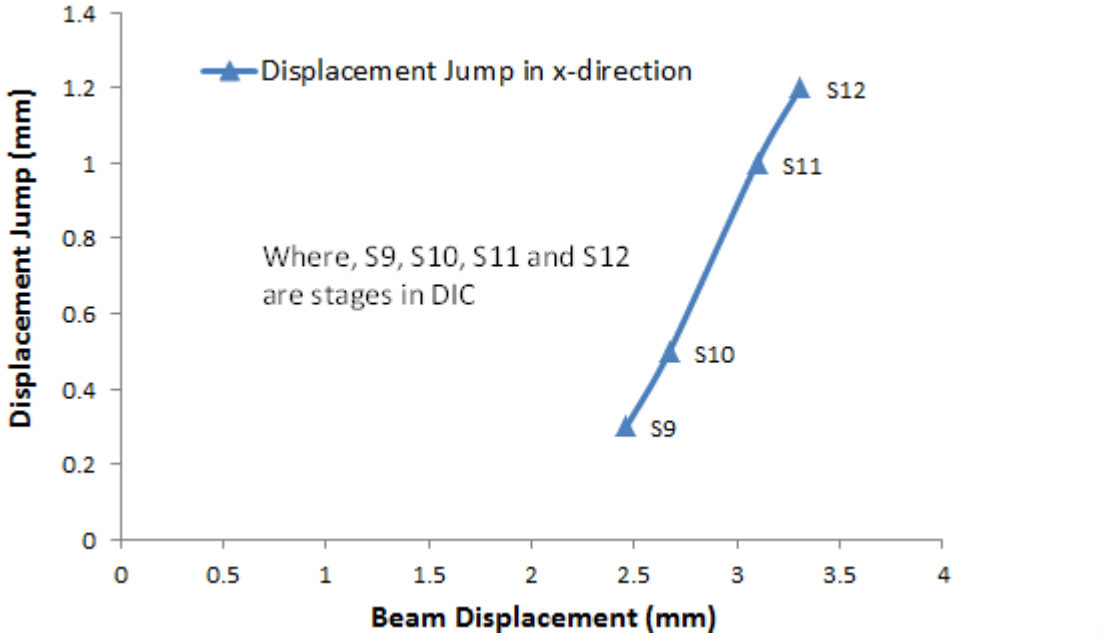

Figure 49: Displacement Jump in x-Direction vs. Beam Displacement from Stage 9 to 12 Extracted Through Sections 0

In addition to displacement jumps, the strain maps of ε_{xx}, ε_{yy} and ε_{xy} have also been plotted through the same sections. Figure 50-52 shows the ε_{xx}, ε_{yy} and ε_{xy} strain profiles vs. beam displacement. Note that, all curves show similar trend. The corresponding strain increases with further beam bending and subsequent stages. The strain plots suggest that the kink band carries a mixture of normal and shear strains inside the kink band.

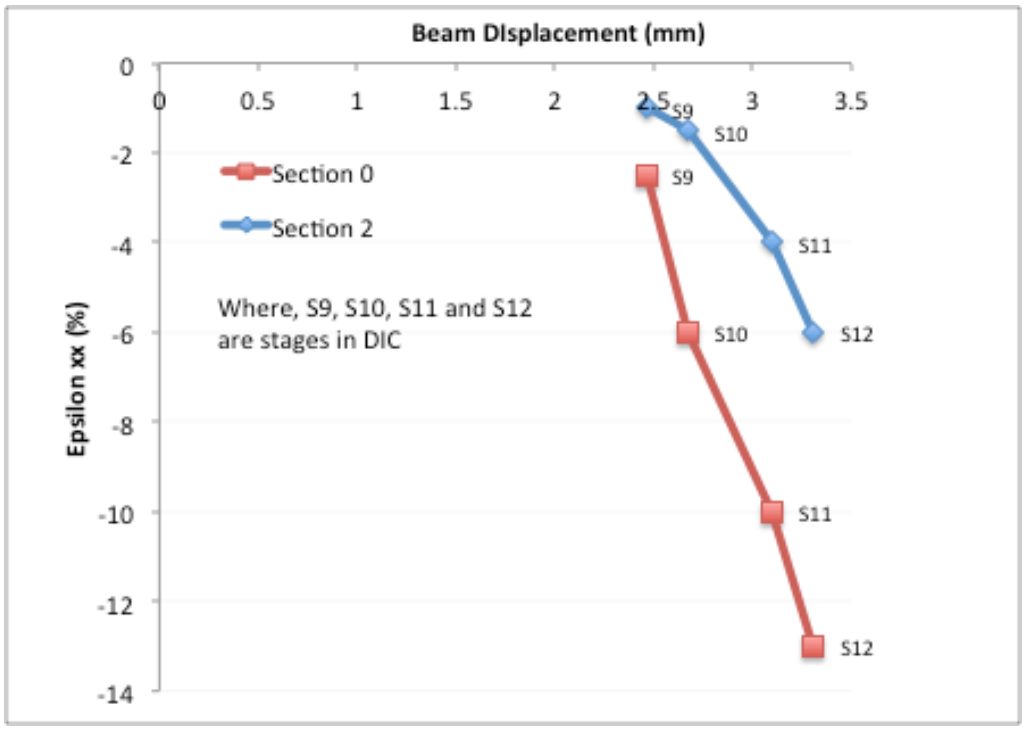

Figure 50: Normal Strain in x-Direction vs. Beam Displacement from Stage 9 to 12 Extracted Through Sections 0 and 2

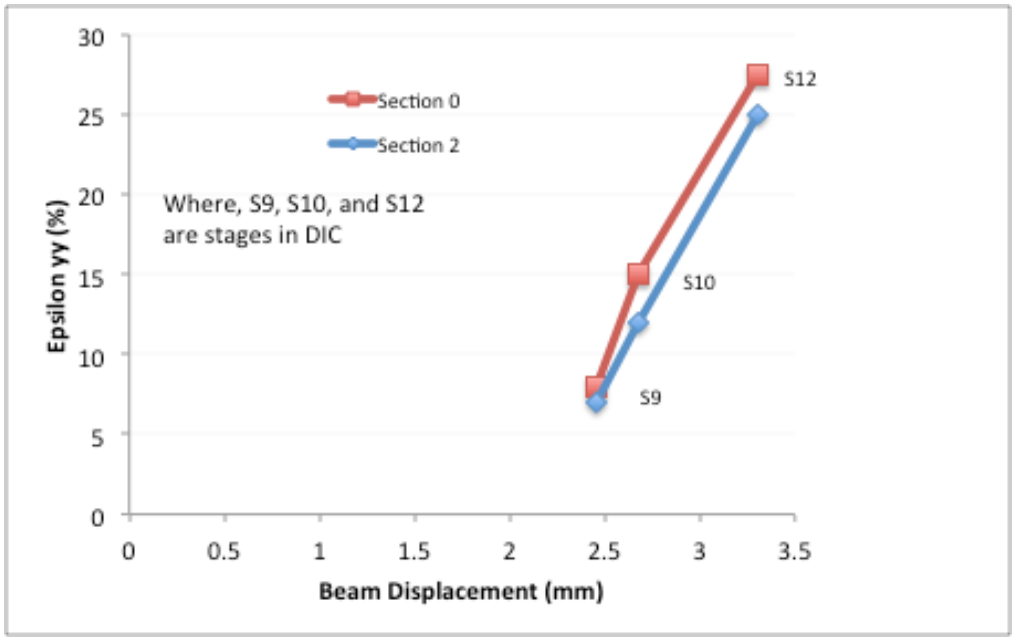

Figure 51: Normal Strain in y-Direction vs. Beam Displacement from Stage 9 to 12 Extracted Through Sections 0 and 2.

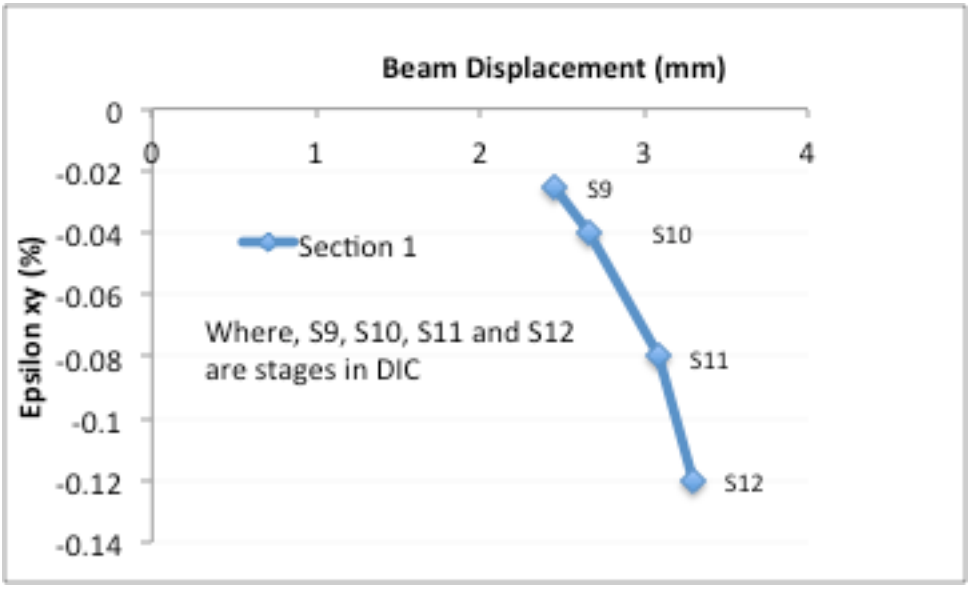

Figure 52: Shear Strain vs. Beam Displacement from Stage 9 to 12 Extracted Through Section 1.

To evaluate the actual strains (mainly shear) inside the kink band, further analysis has been done by rotating the coordinate system as shown in figure 53.

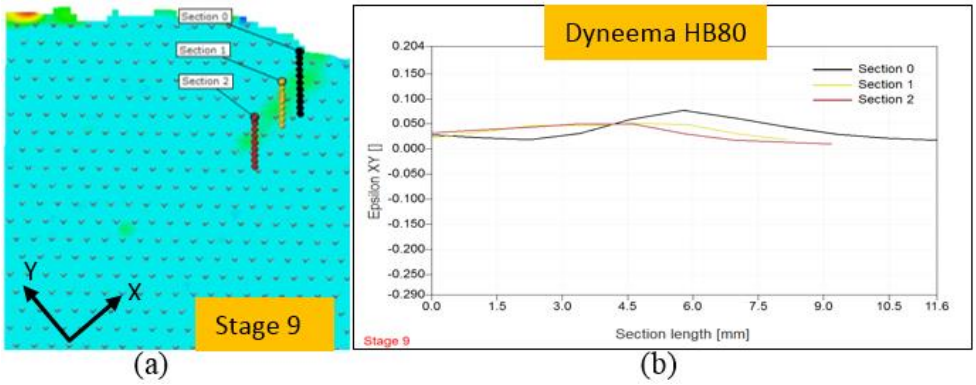

Figure 53: (a) Kink Band in Rotated Coordinate System along with Stages (b) Shear Strains Across Sections 0, 1 and 2.

The shear strain for section 0 is approximately 8%. As the band propagates and evolves with further bending, the shear strain increases for the same section. Figure 54 shows

approximately 300% of increase in shear strain from stage 9 to stage 12 for the same section 0.

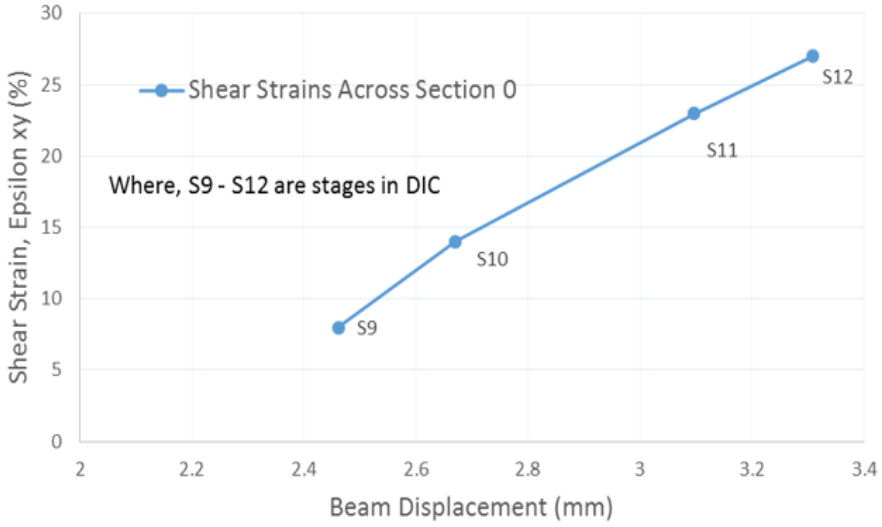

Figure 54: Shear Strain (%) vs. Beam Displacement (mm) in Dyneema HB80 Sample in the Rotated Coordinate System.

Note, that the strains in all stages increases as the band evolves with further beam displacement. This is because with further bending, the plies rotate (ply rotation angle, α dominates) cooperatively near the vicinity of the load point application.

One interesting and distinguished behavior of kink band evolution in some of the Dyneema HB80 specimens can be noticed from stages 12 and 13. Stage 12 shows another kink band nucleated and propagated perpendicular to a previously nucleated principal/parent band. (See stage 12 in fig. 55 for more details).

Moreover, while capturing and analyzing the details of the first kink band, it was found that a similar kind of kink band in another direction was fully developed (refer stage13, fig. 56).

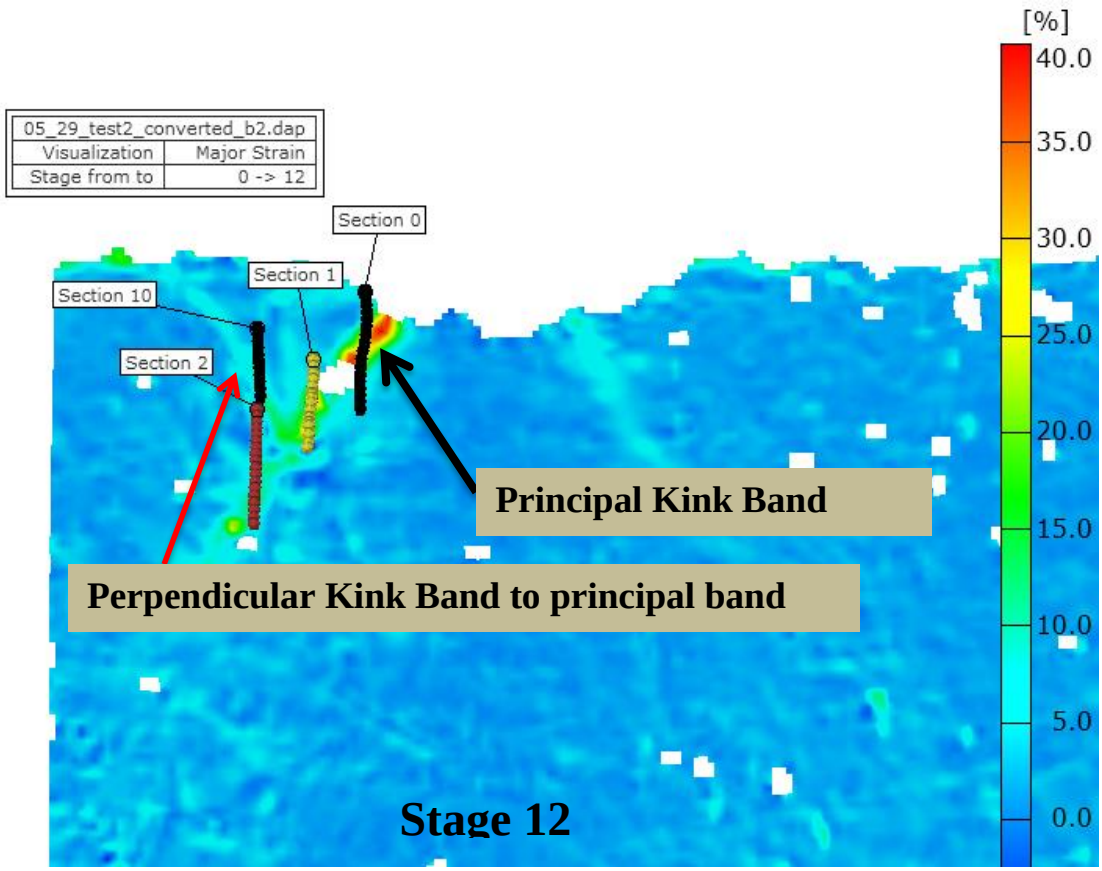

Figure 55: Evidence of Another Kink Band Nucleated Perpendicular to the Principal/Parent Kink Band.

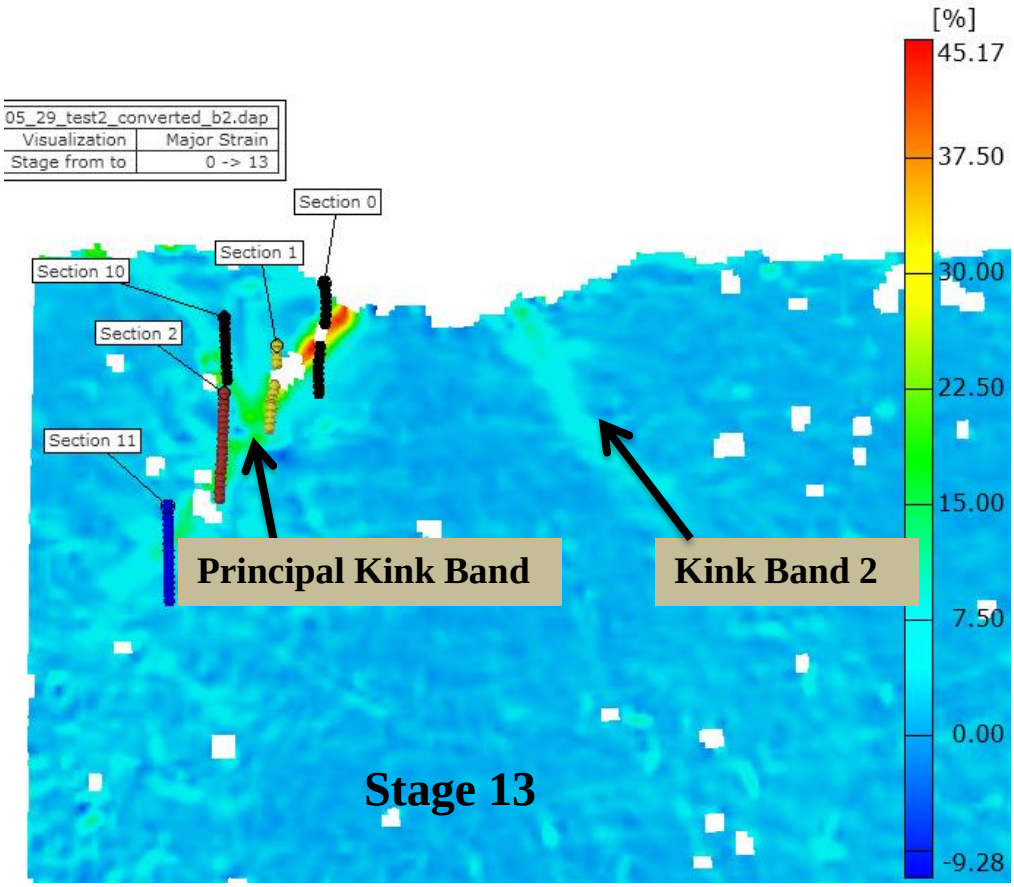

Figure 56: A Similar Kind of Principal Band Fully Developed in Opposite Direction, Named as Kink Band 2 Here.

The formation of the multiple kink bands is an interesting behavior and can be considered as analogous to slip and twining deformation mechanisms, more particularly observed in metals [84, 85]. The literature [82, 83] explains that during the compression failure of

composites, the formation of multiple kink bands is the result of non-interaction of microbuckling with delamination in earlier stages. Therefore, the multiple kink bands in different directions occur to relieve the strains. This can be referred as a strain relieving mechanism as well.

DIC Results for Spectra Shield:

Figures 57-59 show the process of kink band evolution in a Spectra Shield specimen from stages 6 to 8. Stage 6 shows the nucleation of the kink band from the compression side of the beam where the loading was applied. Note that section 0 (black line) has displacement jumps both in X and Y directions, which indicates a kink band has nucleated and propagated. The major principal strain recorded for a corresponding stage 6 is approximately 12% through section 0 and 4% through section 1 as shown in a figure 57 (d). As the kink band propagates through stages 6 to 8, a noticeable difference in displacements and major principal strain can be observed. Stage 8 in figure 59 (d) shows approximately 33% of principal strain, extracted through section 1, which indicates an increase of about 725% on maximum strain between stage 6 and 8 at the same corresponding section for an increase in displacement of 10 % and an increase in load of 11 %.

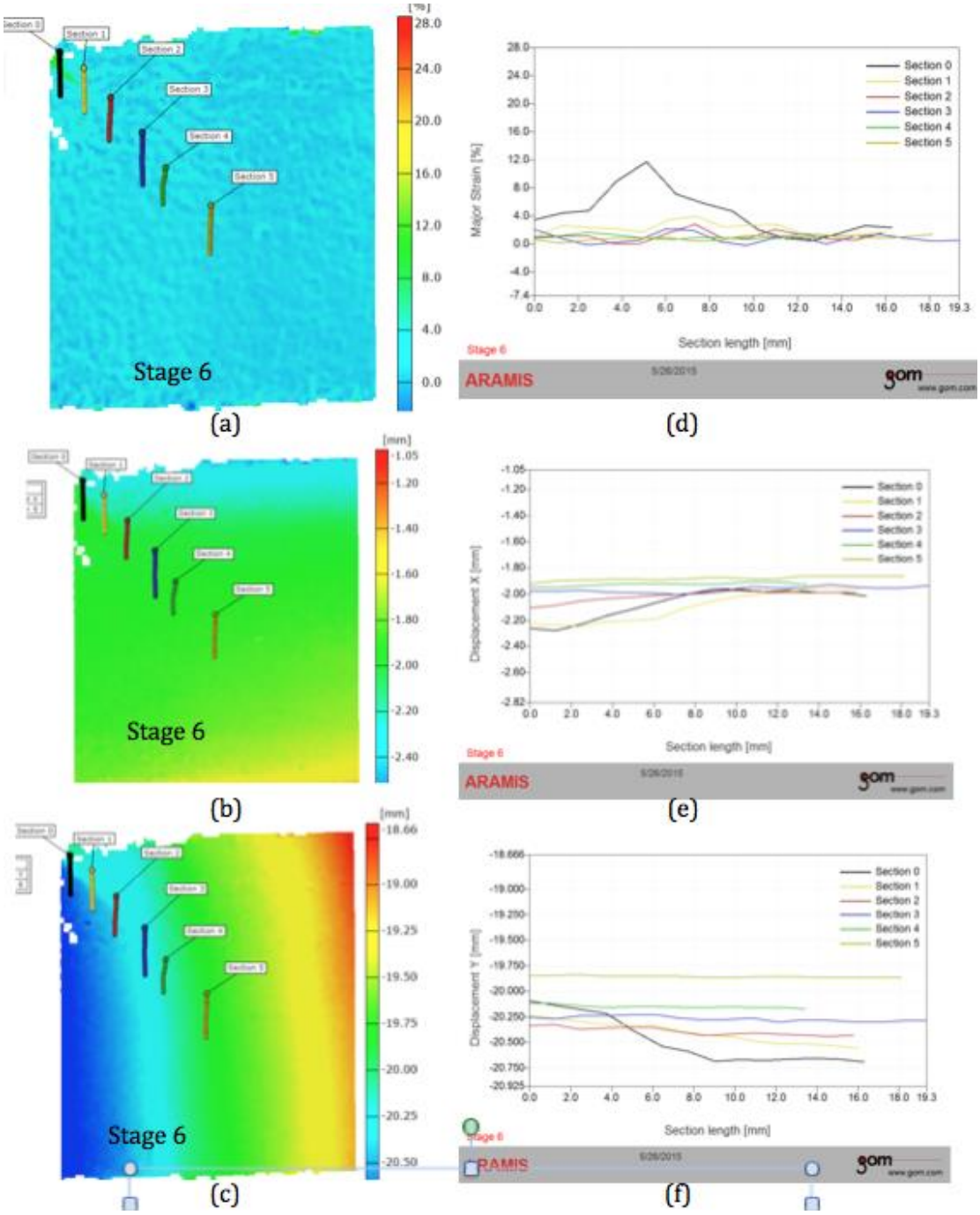

Figure 57: (a-c) Left: Location of Sections for Stage 6 to Extract Major Principal Strain, Displacement-x, and Displacement-y; and Its Corresponding Profiles Along the Same Sections, (d-f) Right Respectively.

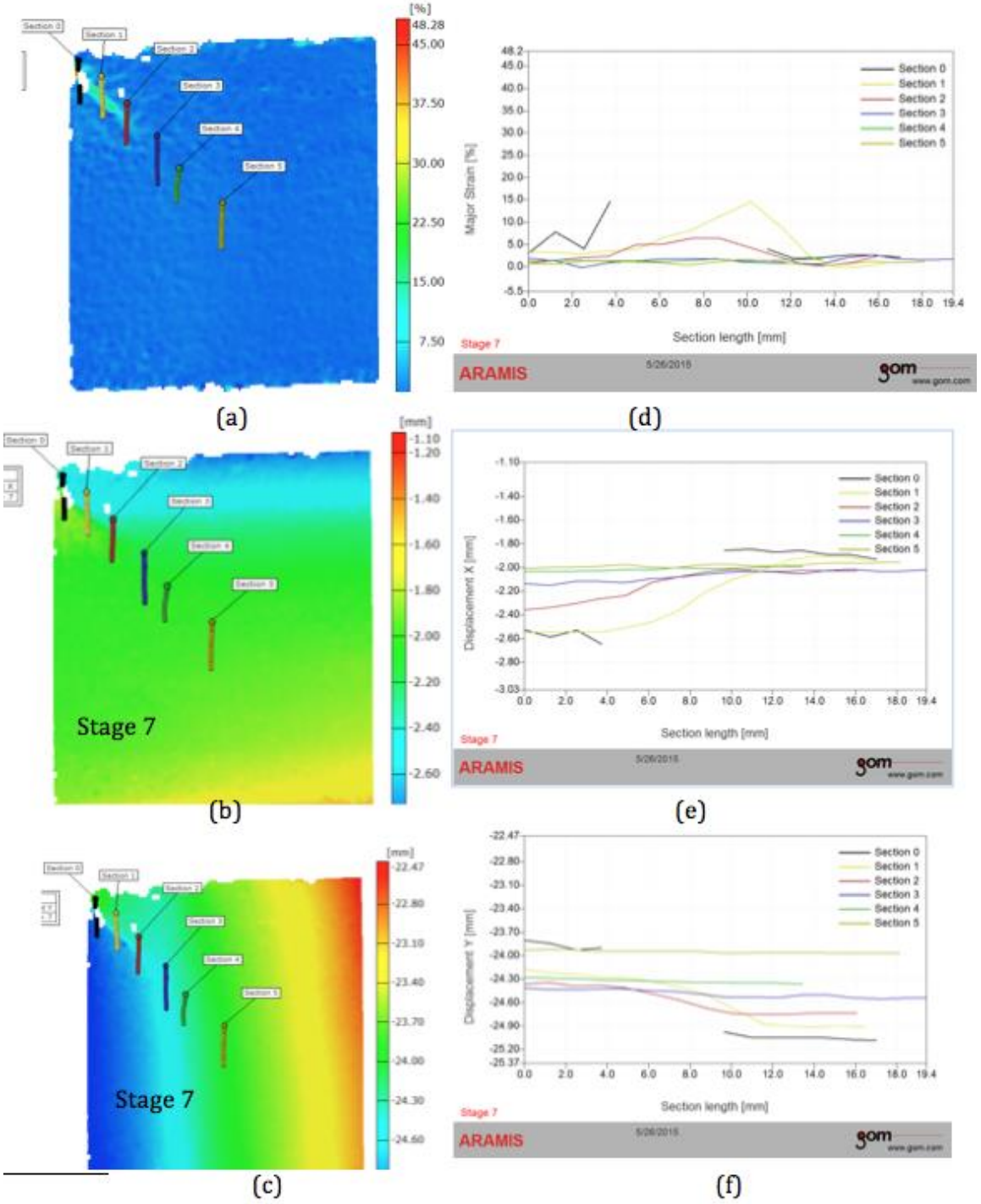

Figure 58: (a-c) Left: Location of Sections for Stage 7 to Extract Major Principal Strain, Displacement-x, and Displacement-y; and Its Corresponding Profiles Along the same Sections, (d-f) Right Respectively.

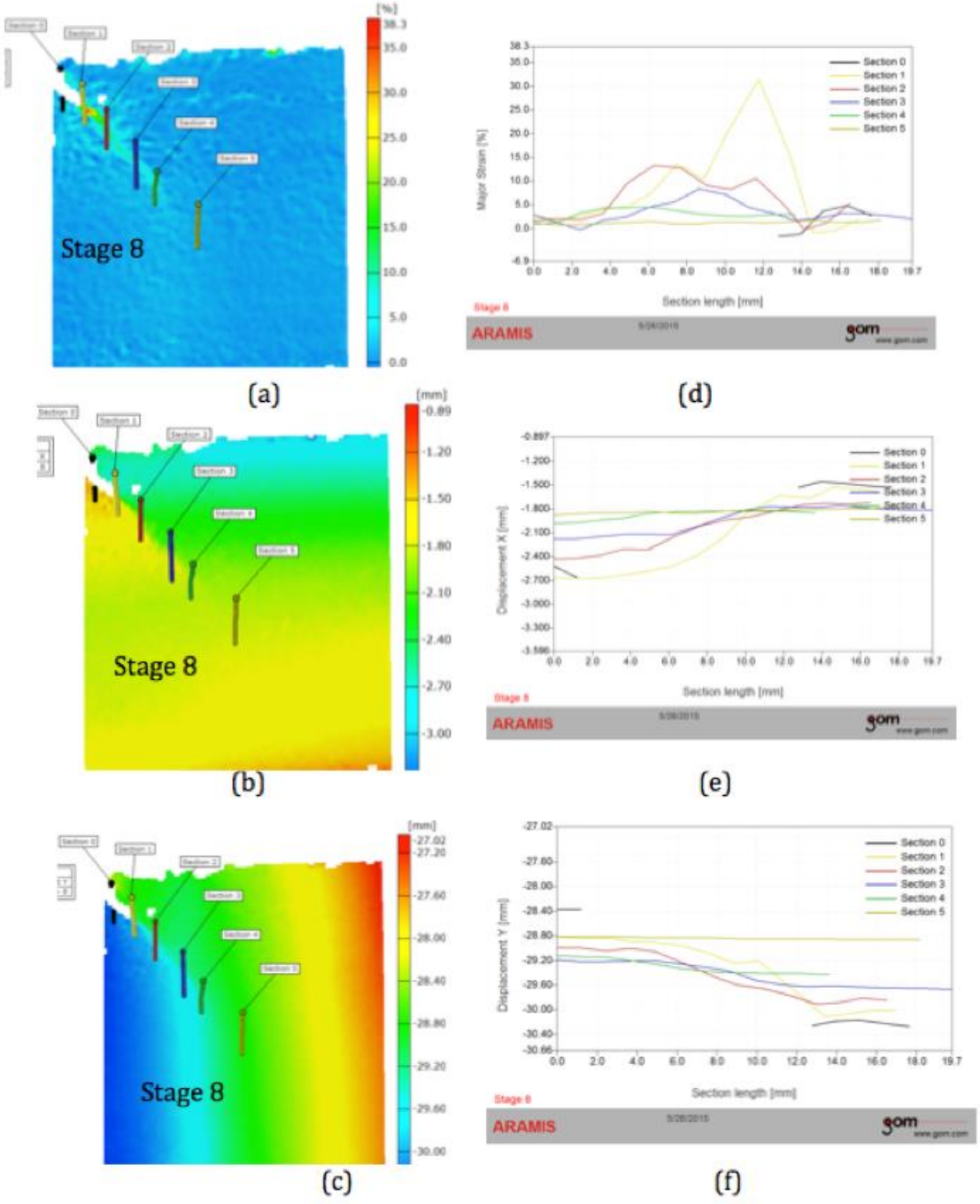

Figure 59: (a-c) Left: Location of Sections for Stage 8 to Extract Major Principal Strain, Displacement-x, and Displacement-y; and its Corresponding profiles Along the Same Sections, (d-f) Right Respectively.

With further propagation of a band, a major principal strain across the sections 0 to 5 increases. For example, the maximum principal strain through section 4 in stage 10 is approximately 22%, which significantly increases to approximately 37%, a raise of approximately 170% with kink band propagation. Similar behavior can be noticed from figures 60. It shows the increasing major principal strain in a propagating band from stage 6 to 11.

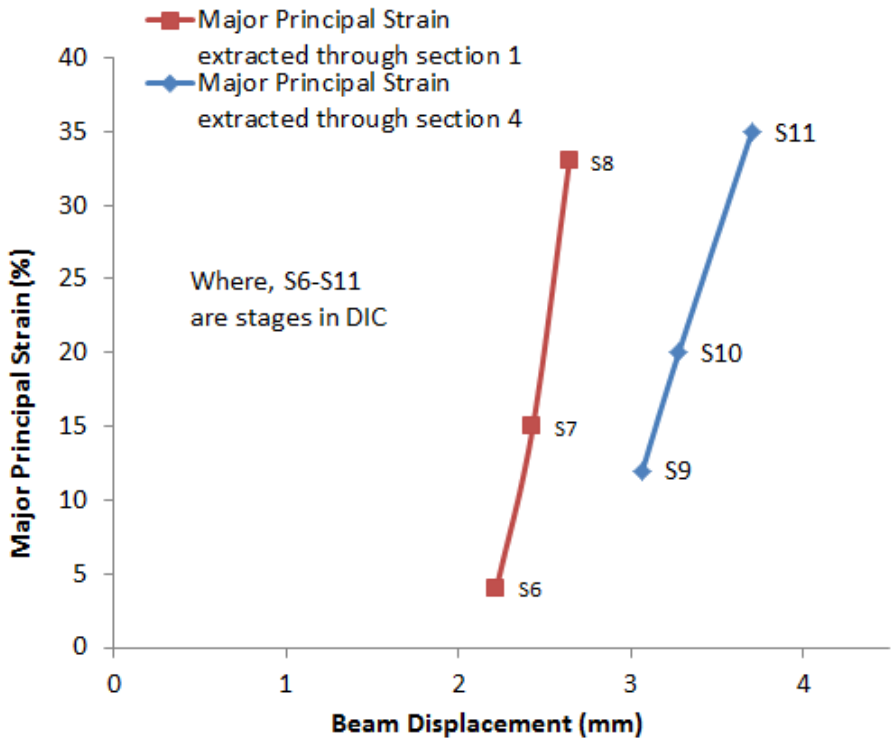

Figure 60: Major Principal Strain (%) vs. Beam Displacement from Stage 6 to 11 Extracted Through Sections 0 and 4.

Referring to the figure 61, note that the displacement jump in the X direction, increases from stage 8 to 10 with further propagation and bending of the beam.

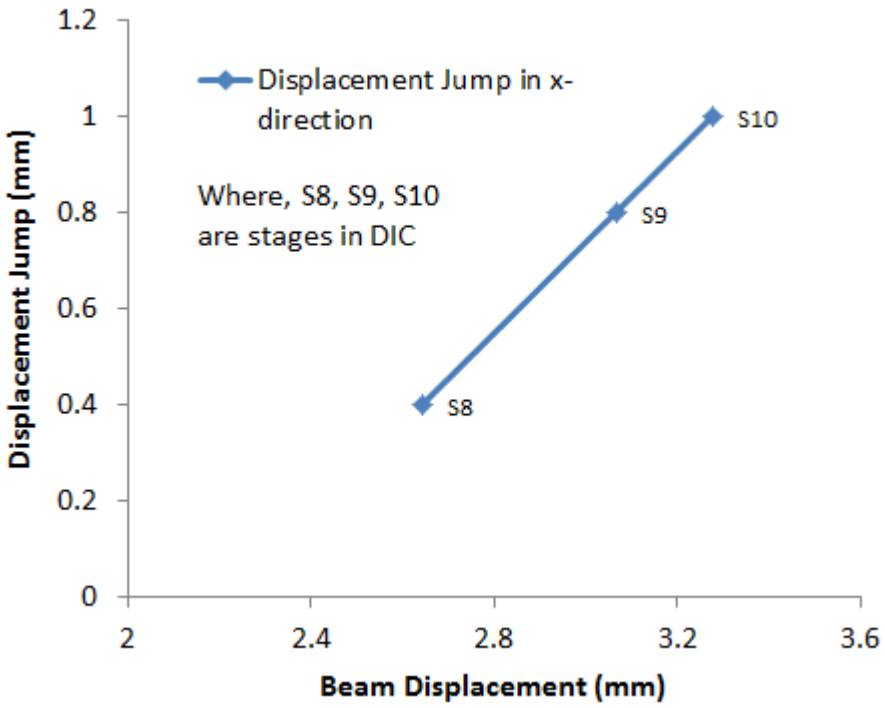

Figure 61: Displacement Jump in the x-Direction vs. Beam Displacement from Stage 9 to 12 Extracted Through Section 0.

In addition the above displacement jumps, the strain maps of ε_{xx}, ε_{yy} and ε_{xy} have also been plotted through the same sections. Figure 62-64 shows the ε_{xx}, ε_{yy} and ε_{xy} strain profiles vs. beam displacement. Note that in all subsequent stages, with further beam displacement, the normal strains in x and y directions and shear strains increases. These are direct evidence of presence of a mixture of normal and shear strains inside the kink band in both the composites.

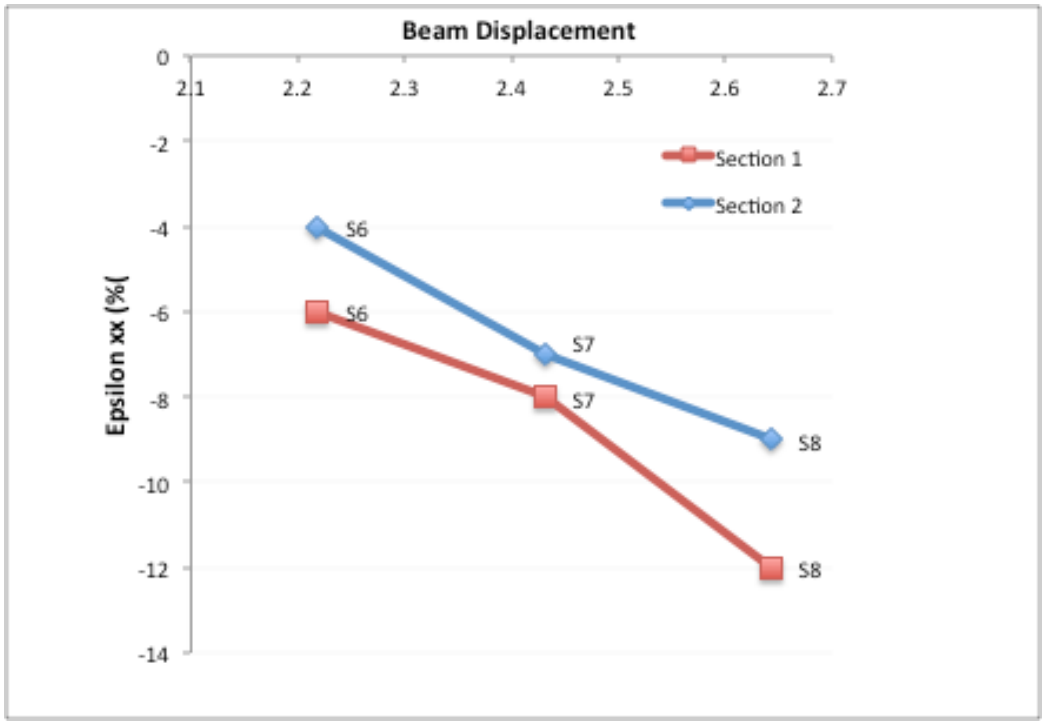

Figure 62: Normal Strain in the x-direction vs. Beam Displacement from Stage 6 to 8 Extracted Through Section 0 and 1.

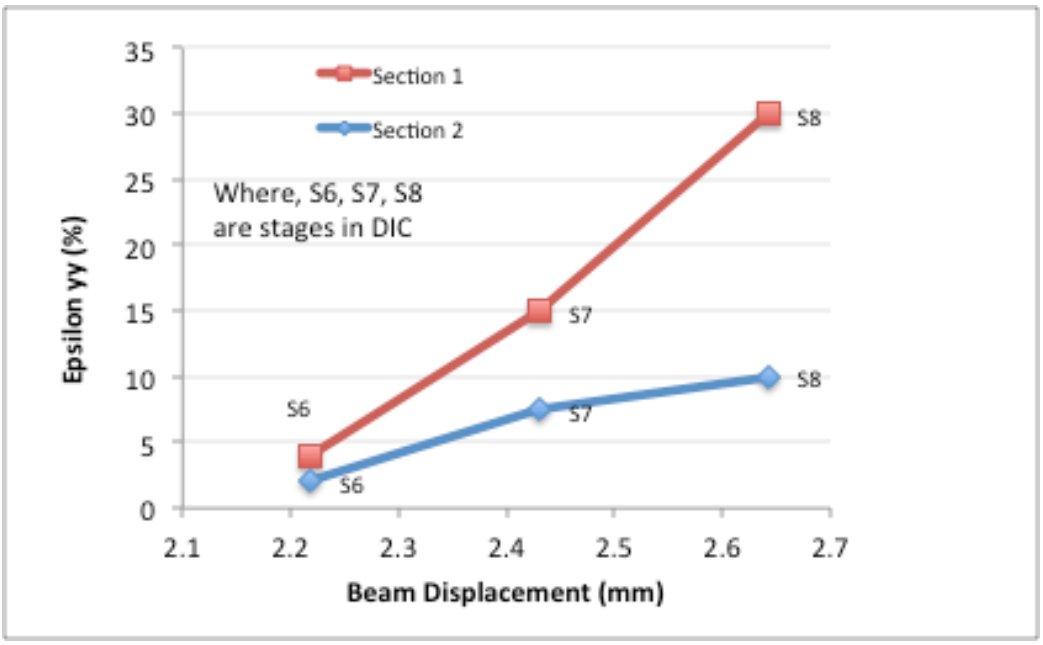

Figure 63: Normal Strain in the y-Direction vs. Beam Displacement from Stage 6 to 8 Extracted Through Sections 1 and 2.

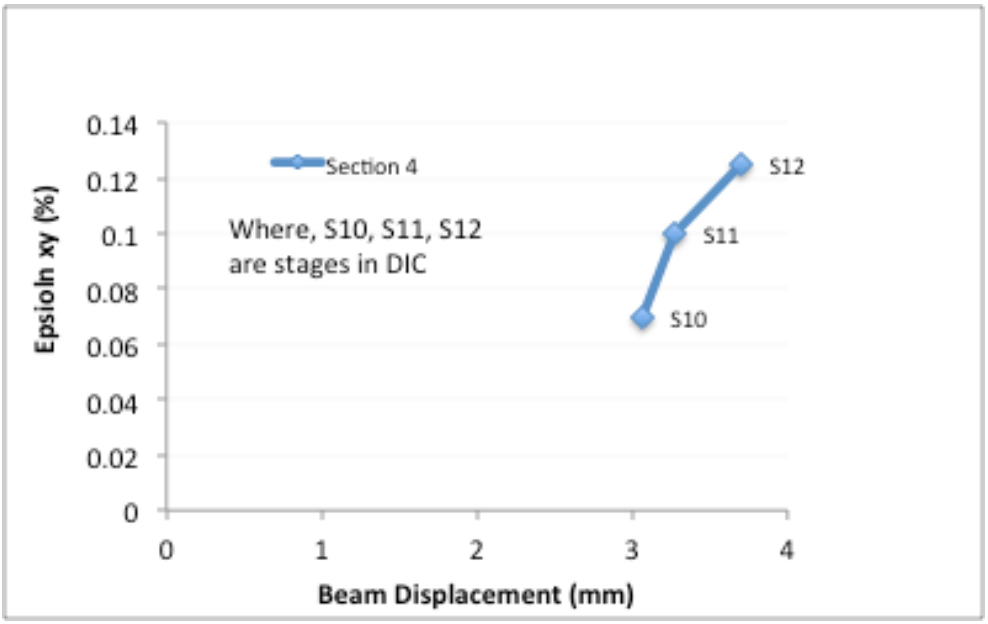

Figure 64: Shear Strain vs. Beam Displacement from Stage 6 to 8 Extracted Through Sections 1 and 2.

Similar procedure has been implemented in case of Spectra Shield to evaluate the strains inside the kink band by rotating the coordinate system as shown in figure 65. The figure 65a shows the rotated coordinate system along with stages and 65b shows the corresponding shear strains (absolute values without percentage).

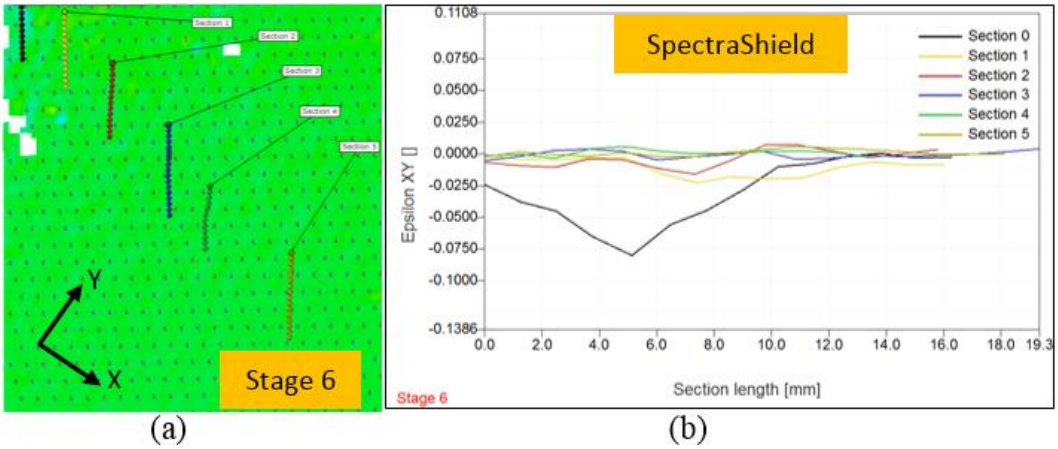

Figure 65: (a) Kink Band in Rotated Coordinate System along with Stages (b) Shear Strains Across Sections 0 to 5.

Note that, the section 0 (black line) in figure 65 shows nucleation of kink band. The shear strain across the section 0 and 1 is 7.5 % and 2.5 % respectively. As the band propagates with further bending, the shear strain increases. This trend has been shown in figure 66. The section 4 in stage 9 has 8% of shear strain that increases by 250% in stage 11 with only 15% of increase in displacement. The explanation for increasing strains during kink band evolution with further bending follows same in case of Spectra Shield too.

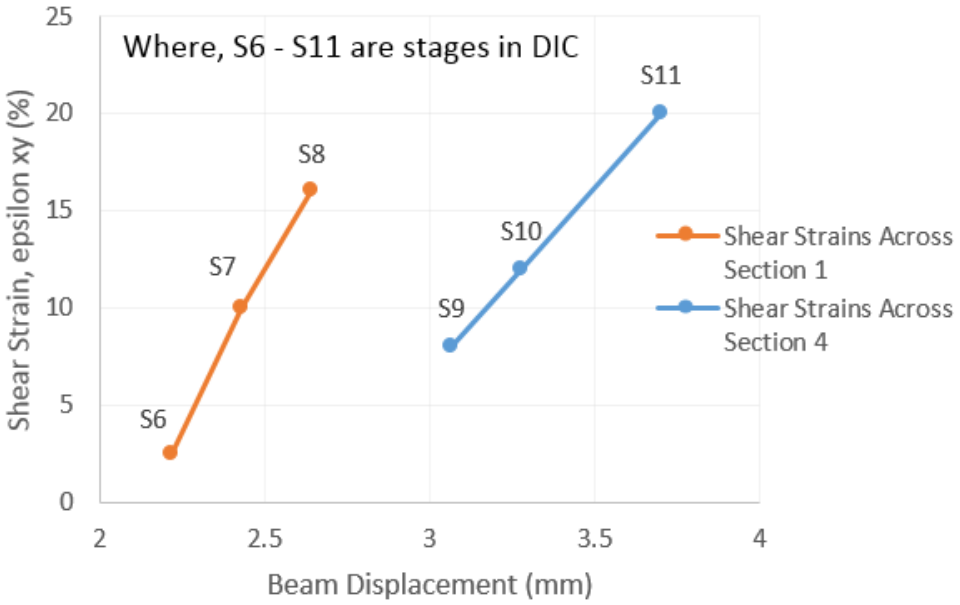

Figure 66: Shear Strain (%) vs. Beam Displacement (mm) in Spectra Shield Sample in the Rotated Coordinate System.

During this experiment and DIC analysis, one interesting behavior was captured in stages 10 and 12. Stage 10 shows another kink band nucleated parallel to a previously principal/parent band in the vicinity of load point application. (See stage 10 in fig. 67a and stage 12 in fig. 67b for more details). Once again, this is analogous to the slip and twinning deformation mechanisms in crystalline materials. The formation of multiple kink bands in other directions can be referred as a strain relieving mechanism. The principal kink band releases extra amount of strains as a result and that induces a parallel band to take the counter effect of high strains. A similar explanation it has been offered for Dyneema HB80. The results and procedures described here open a new window of opportunity to study the physics behind this behavior in particular with respect to composites, unfortunately, this is beyond the scope of the current study.

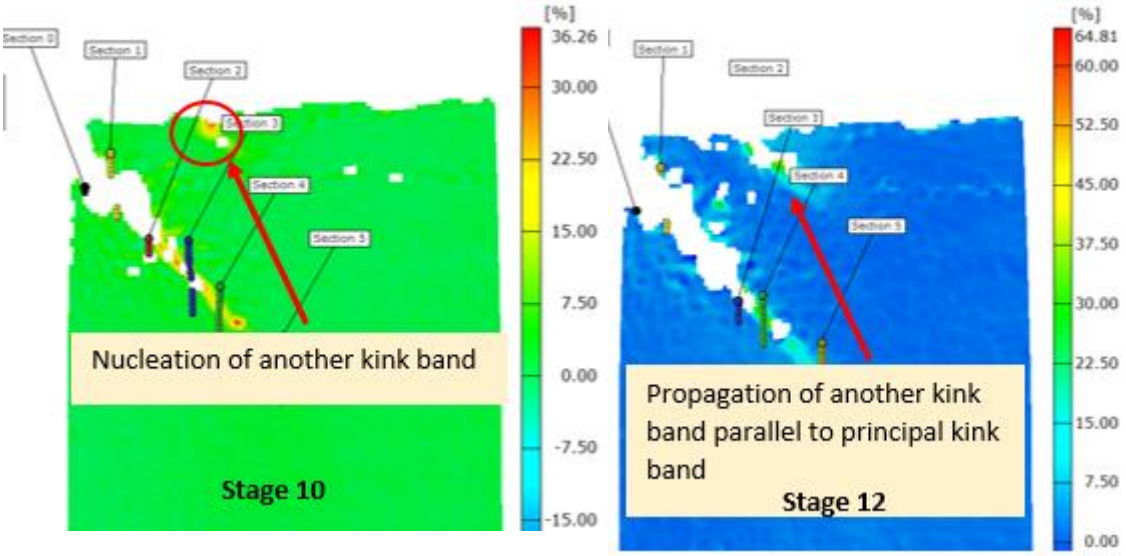

(a) (b)

Figure 67: (a) Nucleation of Another Kink Band Parallel to Principal/Parent Kink Band (b) Propagation of Another Kink Band Parallel to Principal/Parent Kink Band.

The above description shows the presence of kink band during sample deformation under bending as triggered by plastic microbuckling. Note that, close to the peak load in stage 6, the band has already been nucleated and it propagates from the compression to the tensile side of the beam, referring to stages 6 through 9. This supports the hypothesis that the nucleation event of kink band occurs close to the peak load that is a result of plastic microbuckling and hence the localization of these principal strains inside the band are indirect evidence of microbuckling.

The aforementioned study between two different materials indicates distinct behavior in terms of toughness and stiffness. The Dyneema HB80, with thinner plies is tougher than the Spectrashield. This also depends on the strong and weak interface. It is

indicative that the composite with strong interface and stiffer plies has more bending resistance and hence more fracture energy.

5.2 Optical Microscopy

Figure 68 shows micrographs of a Dyneema HB80 sample. The difference between 0° and 90° plies is clearly visible. The image on the right shows a magnified view of 0° and 90° plies. Note that the plies with fibers coming out of the plane are the 90° plies. Figure 69 shows micrographs of a spectra shield sample.

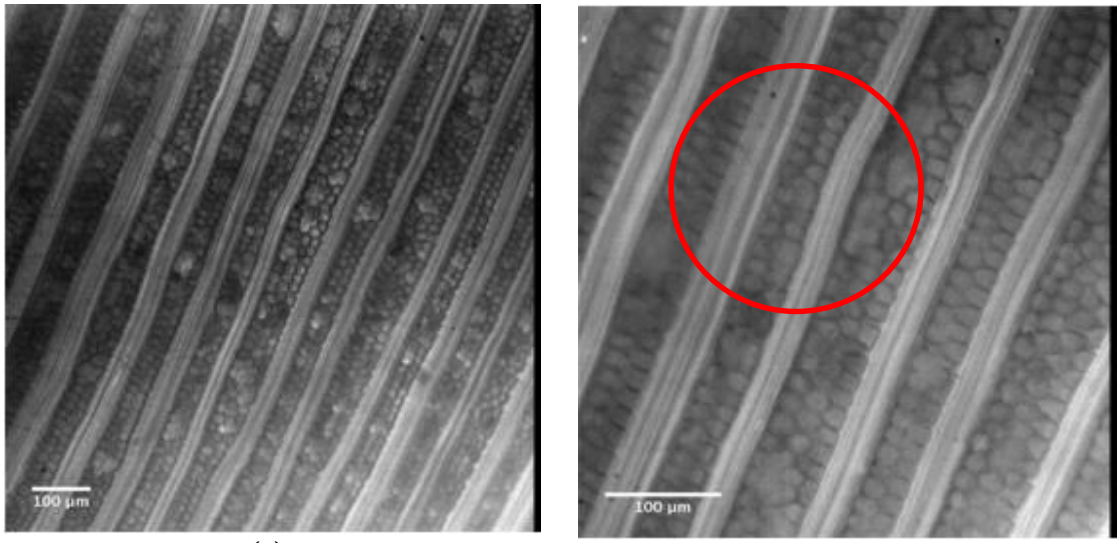

(a) (b)

Figure 68: Micrographs of a Dyneema HB80 Sample (a) Plies with Low Magnification (b) Plies with High Magnification, the Red Circle Represents Defects (Misalignment and Non-Uniform Spacing between Plies).

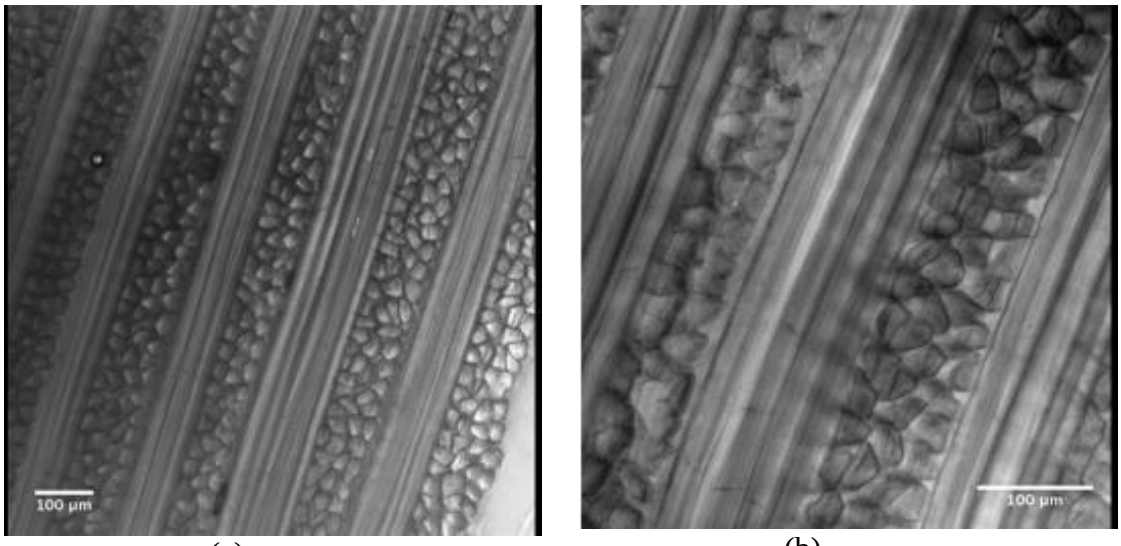

(a) (b)

Figure 69: Micrographs of a Spectra Shield Sample (a) Plies with Low Magnification (b) Plies with High Magnification.

There is a noticeable difference in microstructure between the two materials; in Spectra Shield the plies are thicker and the fiber cross-section is close to an ellipsoid, whereas Dyneema HB80 has thinner plies with defects, i.e., ply misalignment and non-uniform spacing between the plies, and fibers have circular cross-sections. Moreover, the fibers in the Spectra Shield are more densely packed than in Dyneema. However, the deformation localization mechanism (plastic microbuckling) and the corresponding localization of strains (DIC results) in the kink bands are similar under flexural test for the two materials as discussed in the preceding sections. Figure 70 shows transmission optical microscopy pictures from a deformed Dyneema specimen, with samples taken across the deformation band (figure 70a) and from the tip of the band where the sample failed (figure 70b). Figure 70a shows clearly that the Dyneema sample developed a kink band under 3

point bending, as the geometry of the plies across the band looks identical to the kink band schematic shown in figure 3. A kink band width of 560 μm was determined from the micrograph using Image J software.

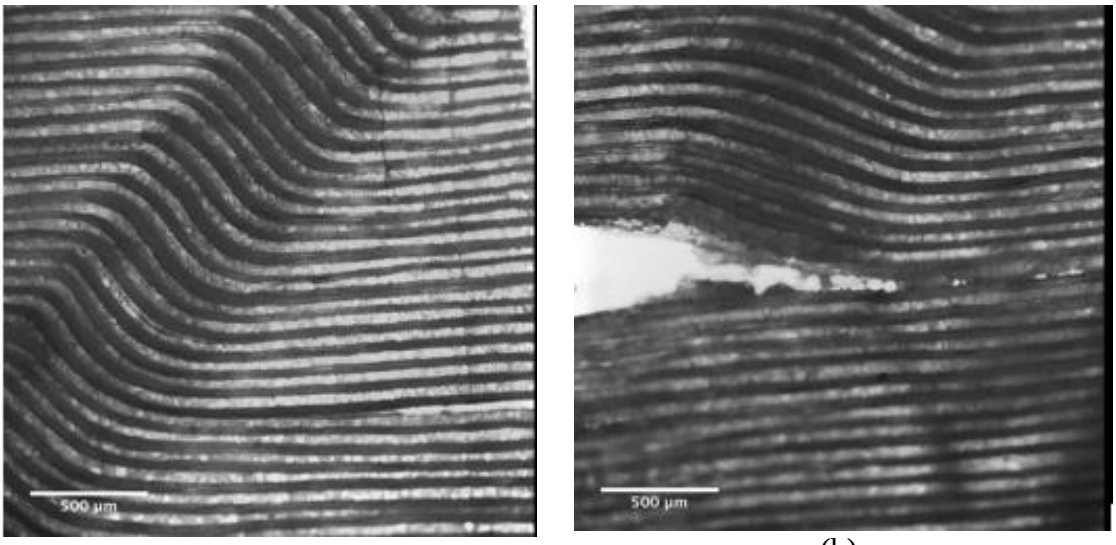

(a) (b)

Figure 70: Dyneema HB80 Sample After 3-Point Bend Test. (a) Kink Band Development. (b) Axial/Longitudinal Splitting of Fibers.

The results shown in figure 70b provide some insights on a failure mode, which is referred to as axial or longitudinal splitting along the fiber-matrix interface. This delamination failure is a culmination of other damage mechanisms, driven by plastic microbuckling during kink band evolution. In particular, this is an interaction of microbuckling with delamination failure. Failure may have occurred due to differential Poisson's contraction between the fiber and the matrix [34, 35] particularly for unidirectional composites and reduces ultimate strain at lamina level. This is very common in pure compression, but with an effect of stress-gradients during bending tests, the delamination failure is more localized because of the bending component. As the band

propagates and the effective bending cross-section of the beam changes, the load bearing capacity of 0° plies reduces. Consequently, the tensile strain perpendicular to the fibers exceeds the critical strain limit due to the maximum stress that were not carried by the net section this eventually triggers the global delamination. Poor interfacial bonding may lead to a reduction in the transverse tensile strength [37] or the matrix ultimate strain, which results in a reduction in the compressive strength. It has also been postulated that poor interfacial bond can effectively reduce the composite shear modulus and allow fiber microbuckling [2] at lower compressive strain level as indicated in references [38], [39] and [40]. The interfacial strength of composite is discussed in next section.

A similar technique was also applied to examine the macroscopic appearance of the failed spectra shield specimen. The figure 71a shows the developed kink band and figure 71b shows the axial/longitudinal splitting of the fibers.

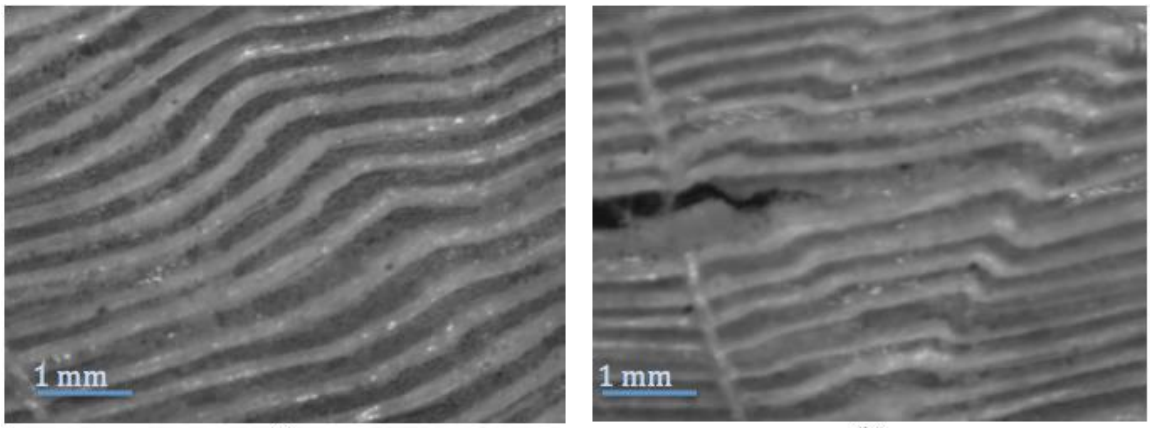

Figure 71: Spectra Shield Sample After 3-Point Bend Test. (a) Kink Band Development.
(b) Axial/Longitudinal Splitting of Fibers.

Note that, the macroscopic behavior for both the materials is similar. However, there is a noticeable difference in the length scale of the kink band. For example, the Spectra Shield has a wider (thick) kink band as compared to Dyneema HB80. This difference is likely a result of their difference in microstructure as in terms of ply thickness. Moreover, the curvature of the kink band is also shallow in case of Spectra Shield, as the kink band curvature is a function of the beam bending. The thicker plies offer more bending resistance to the beam curvature and hence this results in a shallow curvature of kink band. A kink band width of around 900 μm, approximately 1.5 times wider than the Dyneema HB80, was determined from the micrograph using Image J software.

5.3 Interfacial Strength of Composite

5.3.1 Mode I Delamination Fracture Toughness

Data were collected from interfacial strength tests at 75°F. The data for Dyneema HB80 and Spectra Shield were plotted together in Figure 72 to compare the mechanical behavior of these two UHMWPE composites. The magnitude of the mode I fracture toughness G_{IC} gives insight on the bonding strength of the fiber-matrix interface. The mode I fracture toughness G_{IC} was calculated as per the ASTM D5528-01 standard.

$$G_{IC} = \frac{3P\delta}{2wa} \tag{5.1}$$

Where P = load, δ = load-point displacement, w = specimen's width and a = delamination length

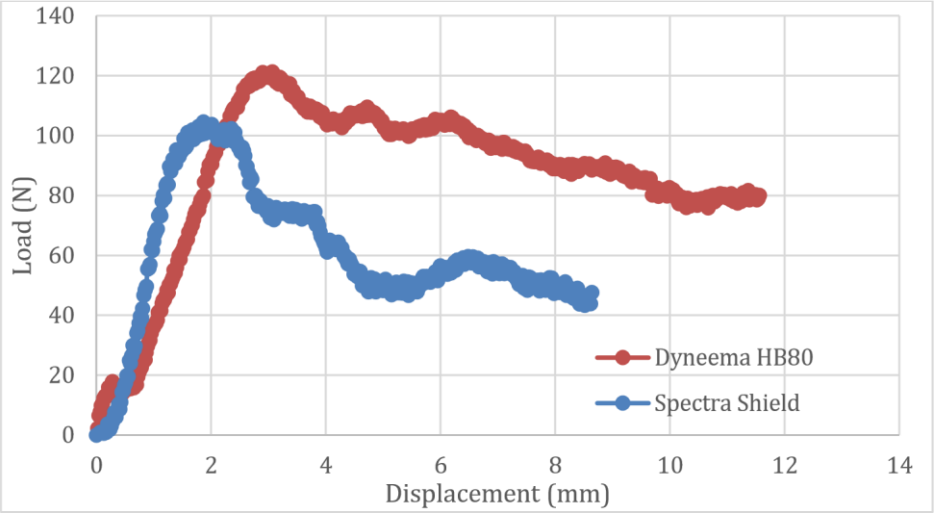

Figure 72: Load vs. Displacement diagram of UHMWPE Samples at 75° F.

Note from figure 72 that the mechanical response of mode I delamination fracture is different for the two composites. The load required to initiate fracture from the pre-crack is higher in Dyneema HB80. The calculated G_{Ic} values are provided in Table 2.

Table 2: Calculated Values of Mode I Fracture Toughness G_{IC} of Dyneema HB80 and Spectra Shield.

Sample tested at RT	**Mode I Fracture Toughness (G_{IC}) (kJ/m^2)**
Dyneema HB80	2.11±0.07
Spectra Shield	1.0±0.1

Note from Table 2 that Dyneema HB80 has higher interfacial strength at room temperature as compared to Spectra Shield; given that Mode I fracture toughness is related to the energy absorbed during delamination. The fairly smooth and linear part of the load-displacement curve corresponds to the elastic bending of two arms of the composite beam. Note that Dyneema HB80 with thinner plies, 132 plies in a half beam section offers more bending resistance as compared to the Spectra Shield that has 76 plies in a half beam section. The peak load, where the curve changes the slope from linear to non-linear corresponds to the maximum load, at which the separation of the plies occurs. In other words, this is the onset where the crack initiates and grows along the bond line. Note that the softening part of the load-displacement curve after separation has some oscillations. These oscillations are most likely the result of formation of kink bands during the bending of the loading arms during the complete delamination process.

Figure 72 also indicates that the area underneath the entire load-deflection curve, referred as fracture toughness, for Dyneema HB80 is higher than the Spectra Shield. This is indicative that the interface in Dyneema HB80 under tensile mode opening is almost 2 times stronger than the Spectra Shield, irrespective to the thickness and number of plies.

It has been postulated that tensile failure and elastic deformation are two major contributors to the energy absorption in ballistic composites. A third key factor is the kinetic energy of the moving part of the composite [36]. The majority of tensile failure occurs nearby the surrounding entry area, energy is then dissipated 360° radially, in plane through the composite. Thus, too strong of an interlaminar bond can become detrimental to ballistic protection performance because the planes cannot slide to absorb extra energy.

5.3.2 Mode II Delamination Fracture Toughness

Data were collected from the single lap shear test to determine the Mode II delamination fracture toughness. Figure 73 shows the load-displacement curves for the two materials. In several experiments it was noted that the peak load observed in the actual curves might not offer conclusive data to determine the Mode II fracture toughness value, because within the overlapped region there might be a ply or a set of plies that is actually continuous across the whole sample, so during loading, these plies will be in tension rather than under shear, leading to a possible rise in the peak load. So, to minimize the error and following the observation from the experiments, a peak value of 12 N/mm for Dyneema HB80 and 5 N/mm for Spectra Shield have been chosen from the flat linear horizontal profile shown as "area of interest" in the same figure 73.These corresponding values trigger the onset of sliding of the interface for respective materials. Referring to this flat region, a displacement of 0.25 mm is the effective region to examine to determine the cohesive peak strength. So, with an effective area of 0.25 mm x 5 mm (part of the effective width), the peak cohesive strength (τ) using the shear formula (as shown below) is approximately 2 MPa for Dyneema HB80 and 1 MPa for Spectra Shield.

$$\tau = \frac{F}{2A} \tag{5.2}$$

Where, τ = peak cohesive strength, F = peak load, A = effective shear area

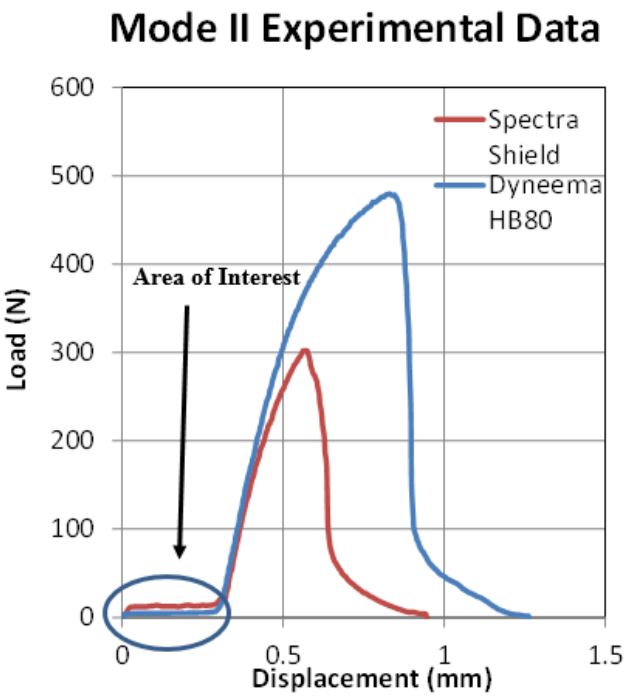

Figure 73: Load-Displacement Curves from a Single Lap Shear Test to Determine the Mode II Fracture Toughness Value.

With the same aforementioned approximation, the effective area underneath that curve corresponds to the Mode II fracture toughness. The values are shown in Table 3.

Table 3: Calculated Values of Mode II Fracture Toughness G_{IIC} of Dyneema HB80 and Spectra Shield.

Sample tested at RT	**Mode II Fracture Toughness (G_{IIC}) (kJ/m^2)**
Dyneema HB80	0.061±0.005
Spectra Shield	0.035±0.004

The aforementioned values do indicate that the interface in Mode II delamination in Dyneema HB80 is stronger in shear as compared to Spectra Shield.

The delamination tests have been simulated using FEM for calibration purposes. The interface properties for Mode I and Mode II are key to predict the microbuckling response as the plies are subjected to both bending and sliding under an effect of stress-gradients. Therefore, the calibration of Mode I and Mode II delamination is required to make the microbuckling model that allows to examine the behavior of multiple buckling events as formulated in the current hypothesis. All these models have been discussed in the next subsection.

5.4 Numerical Simulations

5.4.1 Modeling and Calibration of Mode I Delamination

The modeling parameters have been discussed in chapter 4. The peak stress σ_c=3 MPa and G_{IC} = 2.11 N/mm, measured experimentally, for Dyneema HB80 have been used as inputs for a cohesive zone model with a traction separation law using the maximum damage criterion in Abaqus^{TM}/Standard v6.13.3. Figure 74 shows a load-displacement profile, extracted from the Abaqus^{TM} output at the location where the displacement boundary conditions were applied. Note that the peak load, where the separation begins, matches quite well with the experiments, which is one of the primary objectives while calibrating a cohesive model. The softening part refers to the complete separation of plies. The load-oscillations observed in this softening region are already explained in the preceding section.

Figure 75 shows the delaminated portion during the fracture event, captured in the simulation. The red color shows the degradation of cohesive elements, which can be output as SDEG – scalar degradation parameter in Abaqus^{TM}. SDEG = 1 indicates the full degradation of cohesive elements. The degradation of cohesive elements represents the failing interface as a result of tensile mode opening.

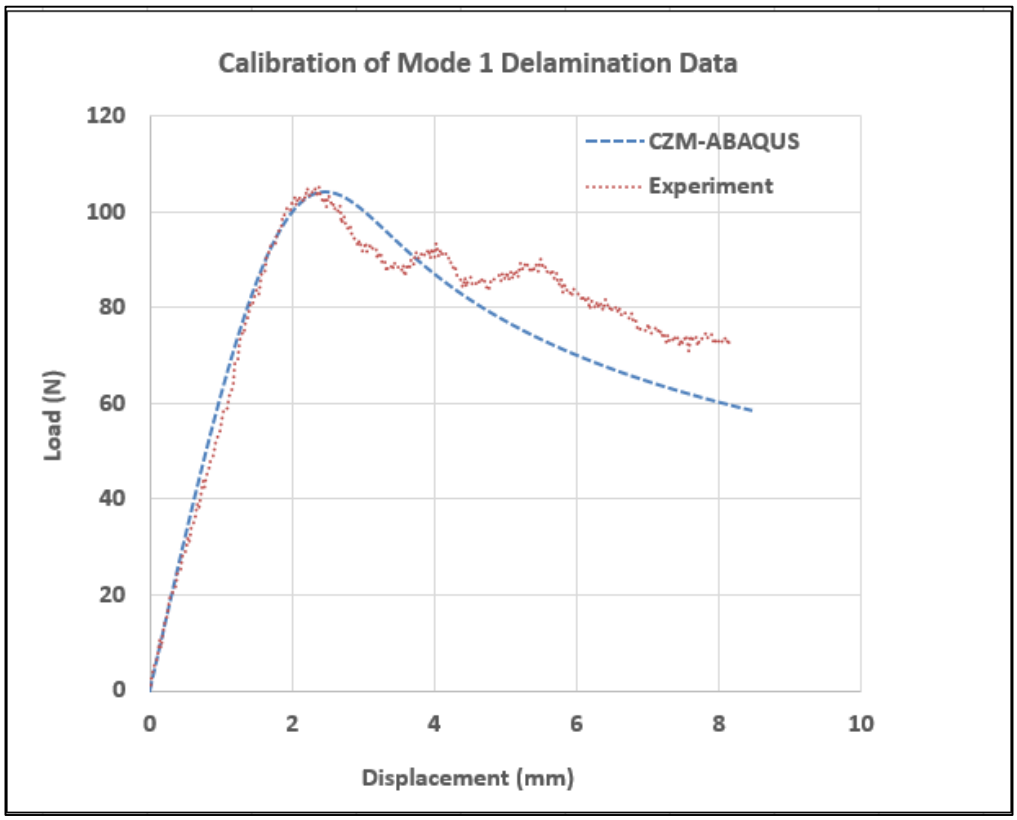

Figure 74: Calibration of Mode I Delamination Data (Dyneema HB80)

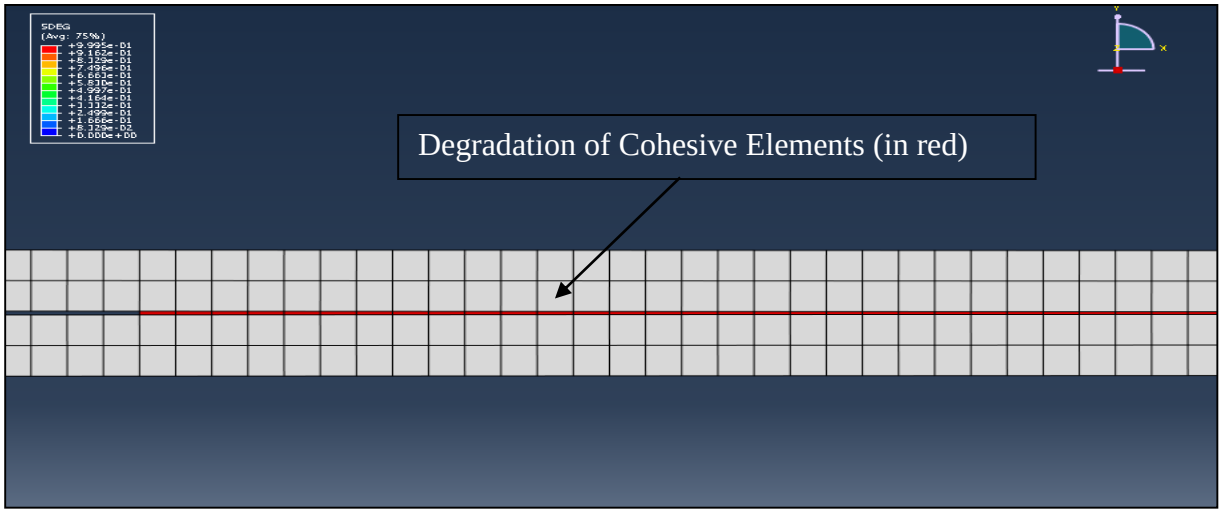

Figure 75: Degradation of Cohesive Elements During the Mode I delamination Fracture Simulation, SDEG=1

The values of peak stress and critical fracture energy were varied, with the constant modulus of elasticity E (obtained from the bending stiffness measured in the experiments) throughout the simulation until the peak load matches the experimental curve as shown in figure 74.

A similar approach was followed to calibrate the model for Spectra Shield as well.

5.4.2 Modeling of Mode II Delamination

A similar approach from Mode I delamination FE model has been implemented to get the traction-separation curve for both the Dyneema HB80 and Spectra Shield. The figure 76 shows the load-displacement (traction-separation) curves.

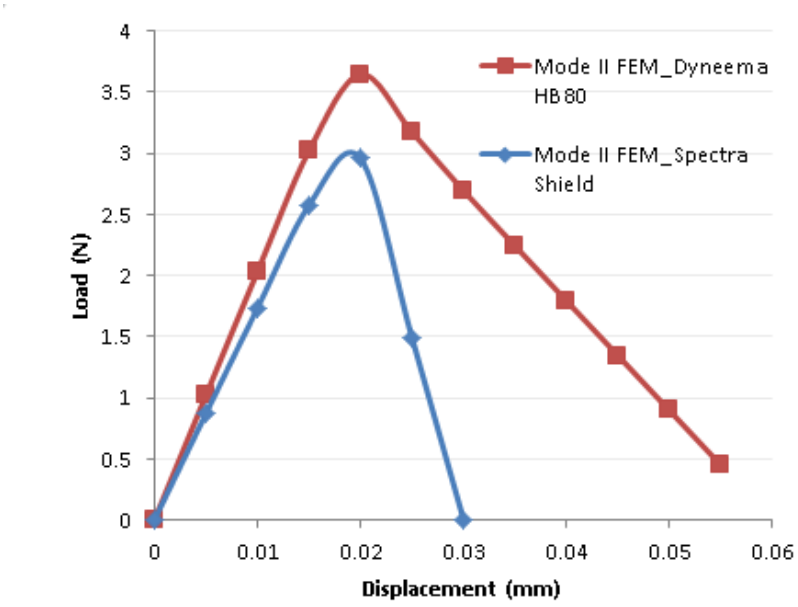

Figure 76: Load Displacement Curves for Mode II Delamination Fracture Toughness from FEM Model.

Note that the area under the curve for Dyneema HB80 is large as compared to Spectra Shield. The model yields a peak stress σ_c=2 MPa and G_{IIC} = 0.07 N/mm for Dyneema HB80 and σ_c=1 MPa and G_{IIC} = 0.03 N/mm for Spectra Shield.

5.4.3 Numerical Simulation of microbuckling model of UHMWPE composites

The formulation of a microbuckling model allows one to examine the behavior of possible deformation/failure mechanisms in UHMWPE composites. The present study focuses on the physics behind the kink band formation and how it interacts with other failure mechanisms under the effects of stress-gradients. In this case, a model has been created with fairly simple assumptions on material behavior; purely isotropic elastic material properties at the ply level and non-linearities (inelasticity) in the cohesive zones, as in terms of hardening-softening traction separation laws representing the strength of interfaces between plies. The geometry is similar to the dimensions of beam samples used in experiments, as explained in chapter 4. The simplified assumptions in material and geometry have been considered to show that the basic behavior observed in the experiment can be reproduced by the simulation as a proof of principle to support the hypothesis formulated in the preceding section to explain the overall behavior. In addition to the proof of principle (supporting the hypothesis), the same model has been used for parametric studies to understand the potential failure mechanisms that trigger kink band evolution under bending and the parameters that influence the morphology of kink band during its evolution.

In this regard, the first primary goal is to calibrate (only the first peak load where the kink band nucleates) the microstructurally explicit ply model to get the global response as it was observed during the 3-point bend test. The Dyneema HB80 has 264 plies in the beam section. But modeling with 264 plies in FEMs will be computationally expensive. Therefore, a model with 66 plies (one fourth), with the same aspect ratio of L/h~16, from the experiments has been accounted to simulate the global response Dyneema HB80. With this case, the calibrated mechanical properties of the plies and interface through several iterations in the finite element model are shown in Table 4 and 5 respectively.

Table 4: Mechanical Properties of 0° and 90° Plies for Dyneema HB80.

Particulars	Young's Modulus, E (MPa)	Poisson's Ratio, u
0° ply	19500	0.3
90° ply	2000	

Table 5: Mechanical Properties of Interface for Dyneema HB80

Delamination Modes	Peak Cohesive Strength, s_c (Mpa)	Interlaminar Fracture Toughness, G (N/mm)
Mode I (opening mode)	3	2
Mode II (shear mode)	2	0.07

The results for this calibrated microbuckling model in figure 77 show the exaggerated portion of microbuckling of plies (a set of 0° and 90°) in the form of kink band within the assigned imperfection region, as expected. Also note that there is a small

local delamination (red region) between each of the 0° and 90° plies within the kink band region. This indicates a poor interfacial bond. The SDEG = 1 indicates the complete degradation of cohesive elements within the cohesive zones. Note that the kink band morphology is similar to what was observed in the post mortem study (material characterization) of a failed Dyneema HB80 sample as shown in figure 70a.

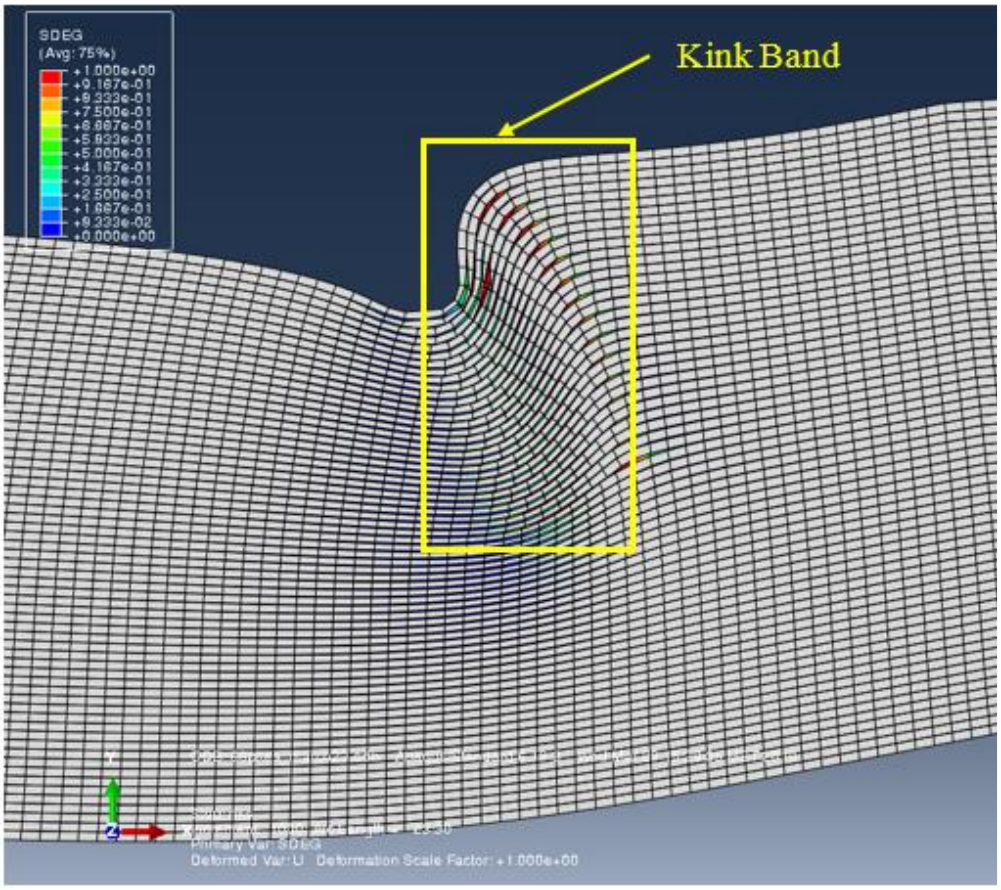

Figure 77: Microbuckling of Plies (Kink Band) in Dyneema HB80 Model, the Red Spots (SDEG=1) are local Delamination between Each of the 0° and 90° Plies.

The corresponding load-displacement profile (global response) extracted from this model is shown along with the experimental curve in figure 78.

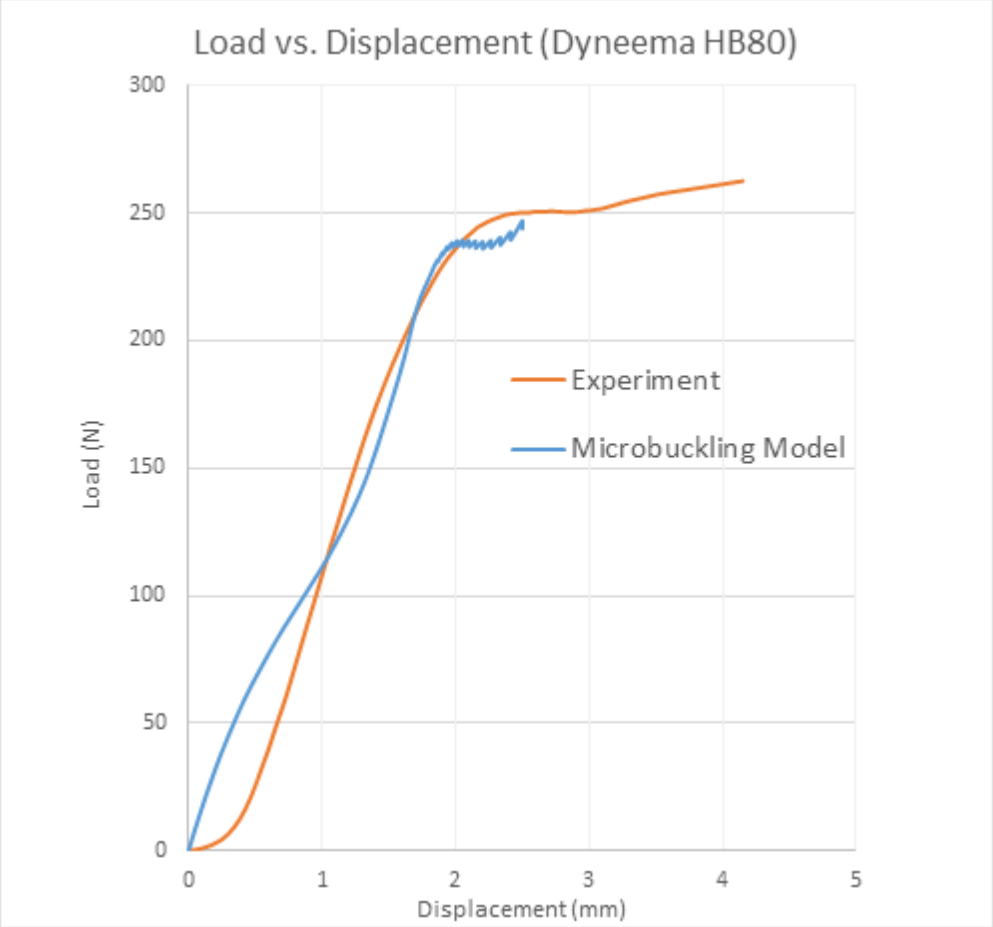

Figure 78: Load vs. Displacement of Dyneema HB80, Microbuckling Model (Blue) and Experiment (Orange).

Note that the global response shows a similar trend, i.e., peaks and drops, to that observed during the experiment. Moreover, the oscillations in the experiment are sparse as compared to the simulated response from microbuckling model as the sample deflection in the experiment is more than the simulation. These oscillations correspond to the onset of kink band nucleation and its propagation along with increasing beam displacement in vertical direction. The model has reproduced the complex physics behind the series of buckling events at the ply level. Note that, the initial portion of the load-displacement

curve is likely an indication of the elastic bending of the overall cross-ply laminate. The reason behind a small curve in the initial part corresponds to a stabilization of the response to elastic bending, coming from plies and interface. The smooth transition (near the first peak load), where the slope changes, (curve changing linear to non-linear) corresponds to the onset of kink band nucleation.

With respect to the microbuckling model shown in figure 78, at the first peak load, near to the transition of slope change, the first buckling event occurs due to the highly localized stresses near the vicinity of the point of load application that has been applied in terms of displacement boundary conditions. Upon the first buckling event, a set of two plies (a 0° ply and the next to it, which is 90° ply, lost their load bearing capacity, which directly reduces the inertia of the cross-section and results in the first load drop (see the corresponding drop in the figure 80) as observed in the simulation.

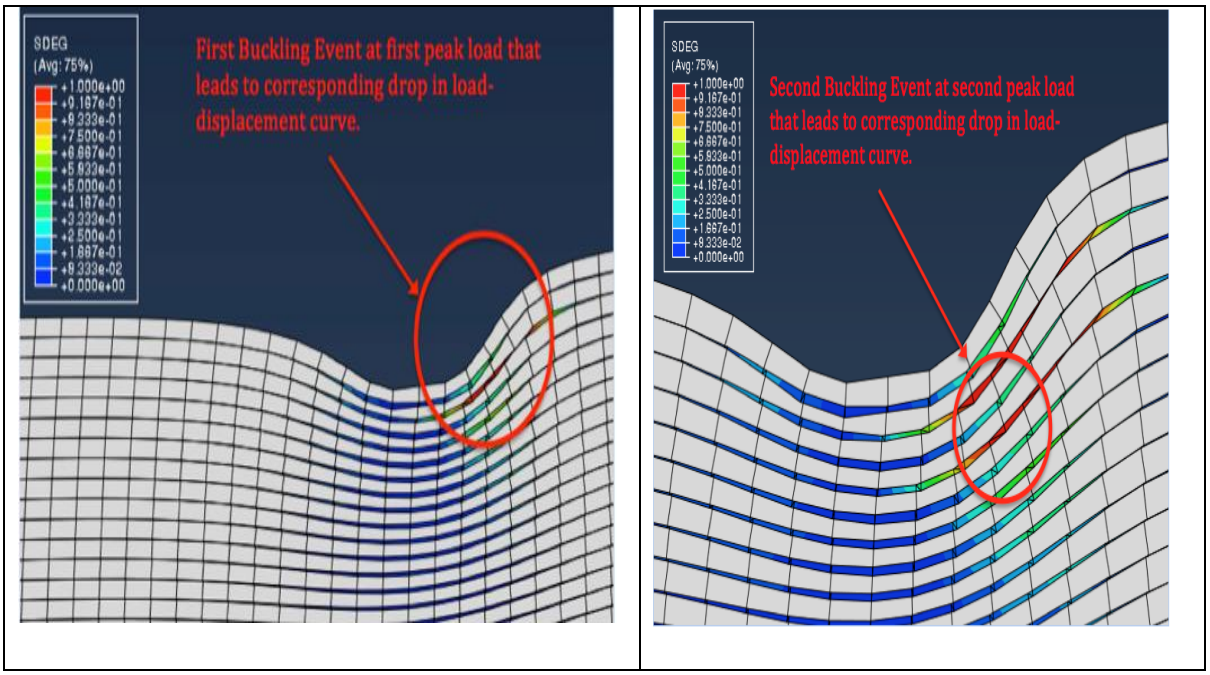

(a) (b)

Figure 79: (a) First Buckling Event of Two Plies (b) Second Buckling Event of Adjacent Two Plies

However, with an increased displacement and bending of the beam, the adjacent plies (intact) start to offer resistance to bending, which results in a rise of load as a subsequent peak is reached, leading to a new buckling event. At this second buckling event, the next adjacent set of two plies lost their load bearing capacity, similar to as it was observed during the first buckling event. This leads to further reduce the inertia of the beam cross-section and results in a rise of load as a second subsequent peak in the load-displacement curve. The corresponding buckling events have been shown in figure 79a and 79b respectively.

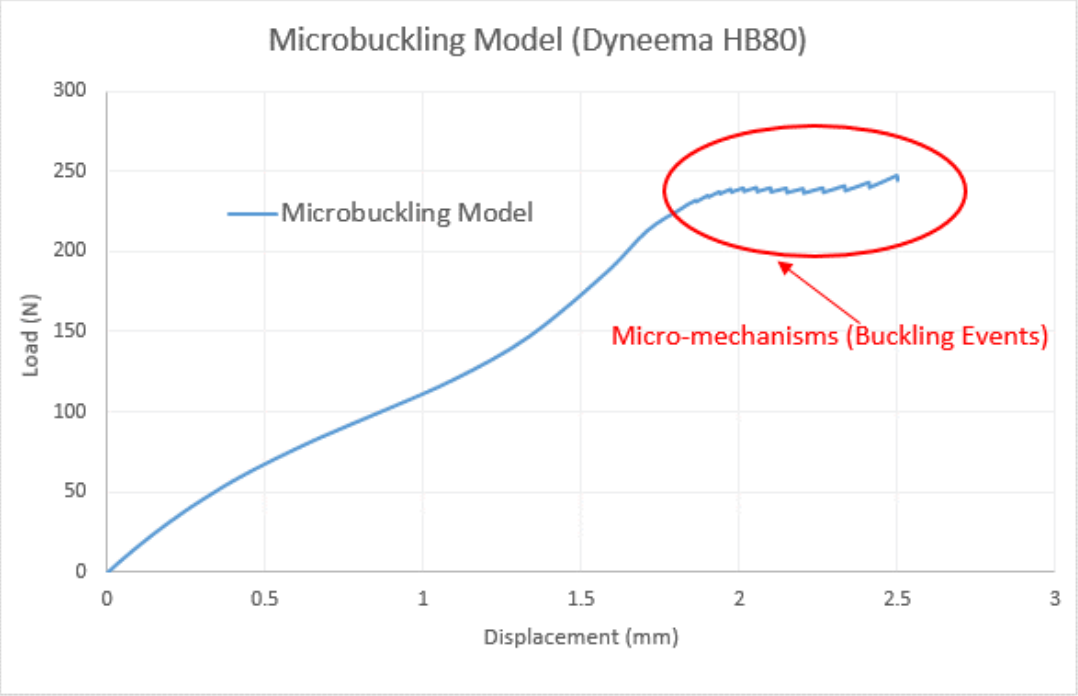

Figure 80: Exaggerated Portion of Oscillations (Micro-Mechanisms) from Microbuckling Model.

This continued process of buckling of several plies and microbuckling in particular leads to form a local bulge near the vicinity of the load point application similar to as it was observed in the experiment (see figure 81). The process of buckling and bulging of plies continued until the kink band leads to delamination (see figure 81), which is a result of complete loss of bending stiffness of the beam.

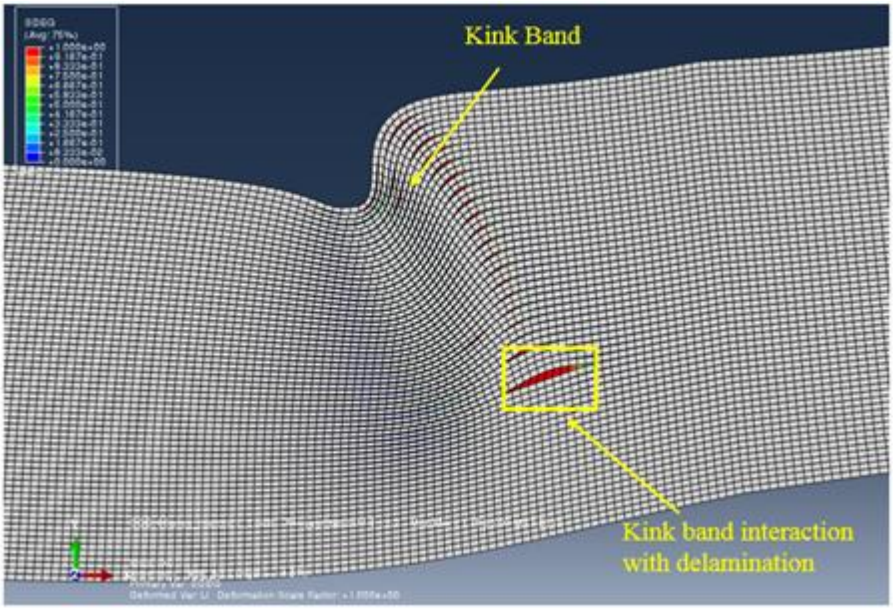

Figure 81: Model Prediction of Kink Band Leading to Delamination.

Microbuckling Response of Spectra Shield

In the case of Spectra Shield, that has 152 plies, the calibrated mechanical properties of the plies and interface, based on close to one fourth of the model, 42 plies has been used. All these calibrated properties through several iterations in the finite element model are shown in Tables 6 & 7.

Table 6: Mechanical Properties of 0° and 90° Plies for Spectra Shield.

Particulars	Young's Modulus, E (MPa)	Poisson's Ratio, u
0° ply	10000	0.3
90° ply	1000	

The interfacial properties for two primary modes are as follows:

Table 7: Mechanical Properties of Interface for Spectra Shield

Delamination Modes	Peak Cohesive Strength, s_c (Mpa)	Interlaminar Fracture Toughness, *G* (N/mm)
Mode I (opening mode)	3	1.85
Mode II (shear mode)	1	0.03

The results for this calibrated microbuckling model in figure 82 show the exaggerated portion of microbuckling of plies (a set of 0° and 90°) in the form of multiple kink bands (wedge shaped) within the assigned imperfection region. Also note that, there is a small local delamination (red region) between each of the 0° and 90° plies with in the kink band region. Note that, the angles of these wedge shaped kink bands are not the same. The band in the left portion is more inclined as compared to the right side band. This behavior is due to the thick and stiffer plies. Note that, the kink band in the case of microbuckling model of SpectraShield is thicker and more diffused as compared to the kink band in the microbuckling model of Dyneema HB80. This behavior is also a function of the thickness of the plies for the two different materials. Dyneema HB80, with thinner plies, has low inertia as compared to Spectrashield. So, upon the series of buckling events, the thicker plies do not localize (bend and rotate) in a similar trend to form the kink band(s) as it is in the case of Dyneema HB80. Many of the spectra shield samples in actual experiments showed multiple kink bands, nucleated from the tip similar to as it has been observed and analyzed in its microbuckling model.

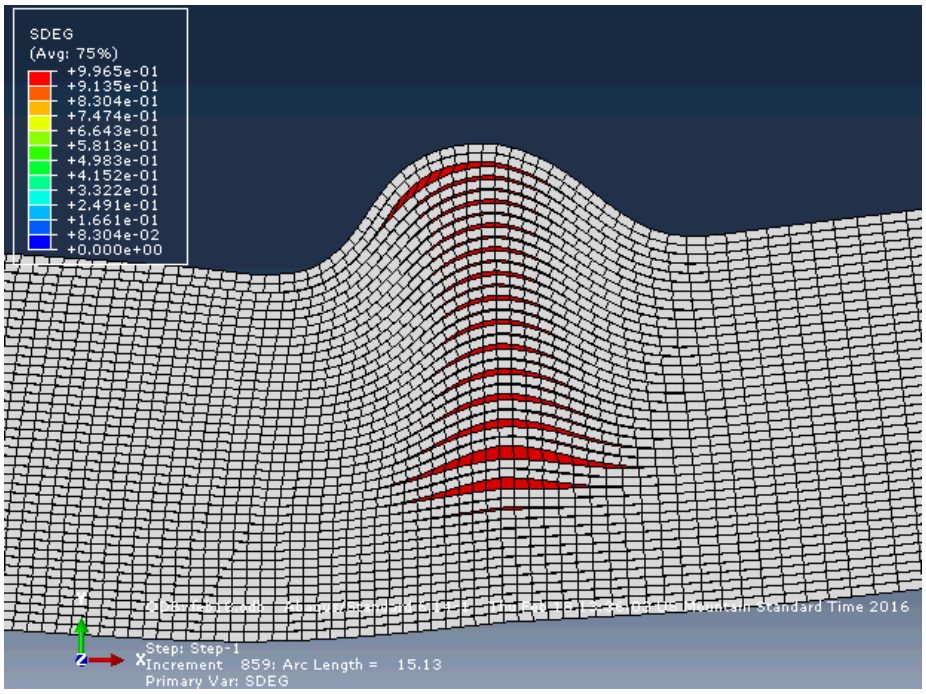

Figure 82: Microbuckling of Plies (Kink Band) in Spectrashield Model, the Red Spots (SDEG ≈ 1) are Local Delamination between Each of the 0° and 90° Plies and the One at the End (a Fairly Large Red Spot) is an Interaction of Kink Band with final (Total Stiffness Loss) Delamination

The SDEG = 0.9965 ≈ 1, indicates the close to complete degradation of cohesive elements within the cohesive zones. Note that the kink band morphology of one of the bands (inner structure) is similar to as it was observed in the post mortem study (material characterization) of failed Spectra Shield sample as shown in figure 71a in preceding section.

The corresponding load-displacement profile (global response) extracted from this model is shown along with the experimental curve in figure 83. Note that the global response shows similar trend, i.e. peaks and drops as it was observed during the experiment. The physical mechanisms of peaks and drops are similar to Dyneema HB80,

as it has been explained earlier. However, the difference between both the materials is the peak load where the kink band nucleates. The exaggerated micro-mechanisms are shown in figure 84.

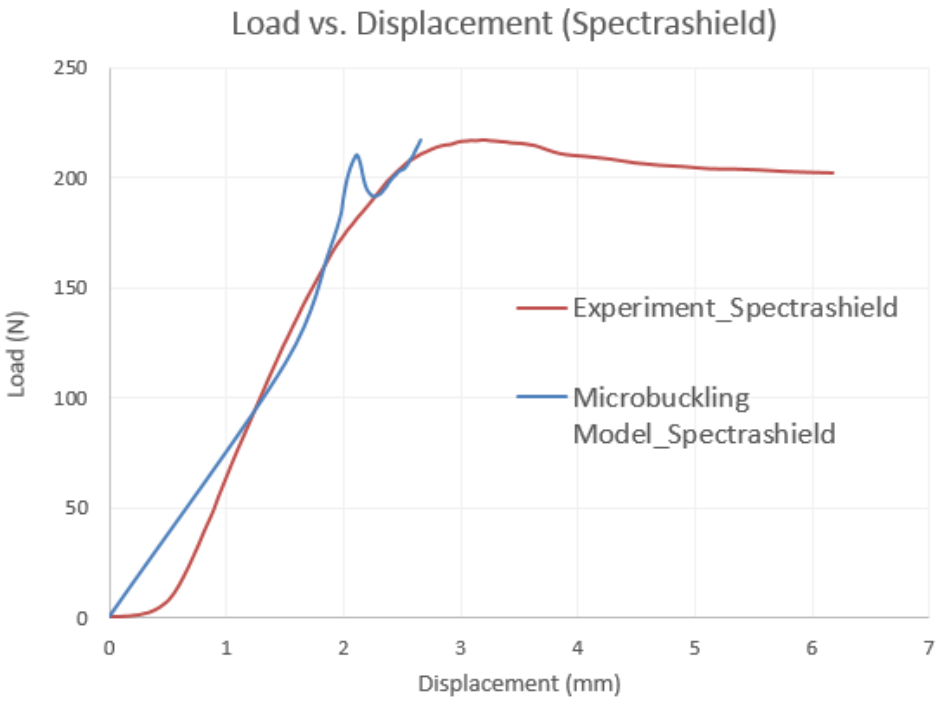

Figure 83: Load vs. Displacement of Spectrashield, Microbuckling Model (Blue) and Experiment (Orange).

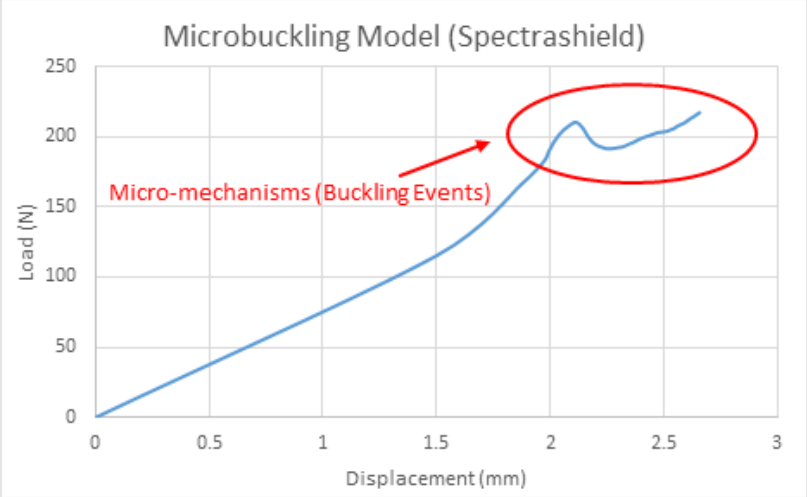

Figure 84: Exaggerated Micro-Mechanisms in Microbuckling Model of Spectra Shield.

With respect to the microbuckling response in Spectra Shield (see figure 84), there is a distinct load drop. This drop corresponds to buckling of more than two plies in this case. It is shown in figure 85a and 85b. The process continues and forms a bulge at the tip similar to it was observed during the experiment.

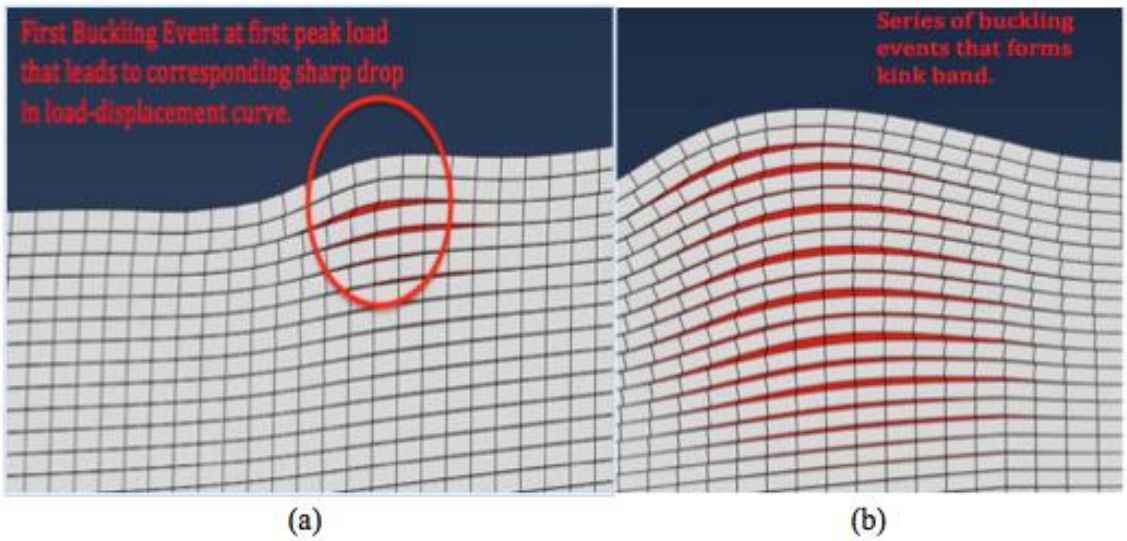

Figure 85: (a) First Buckling Event (b) Series of Buckling Event.

5.4.4 Comparison of Kink Band Morphology between Microbuckling Model and Experiments

The results in figure 86a show the kink band morphology of Dyneema HB80 that was observed through the postmortem study and figure 86b shows the similar morphology through microbuckling model. Note that the parameters such as kink band rotation angle (ply rotation angle), α, kink band inclination angle, β and kink band width, w, in the microbuckling model are in reasonably good agreement with the experimentally observed results, because the model has the same aspect ratio, L/h=16 as it was followed in flexure tests of these composites. All these angles were calculated from Image J software and the width has been calculated from number of localized elements to form the width of the band. In this case approximately 15-17 elements of 30 microns mesh size are within the band, which result in approximately 500 µm of kink band width.

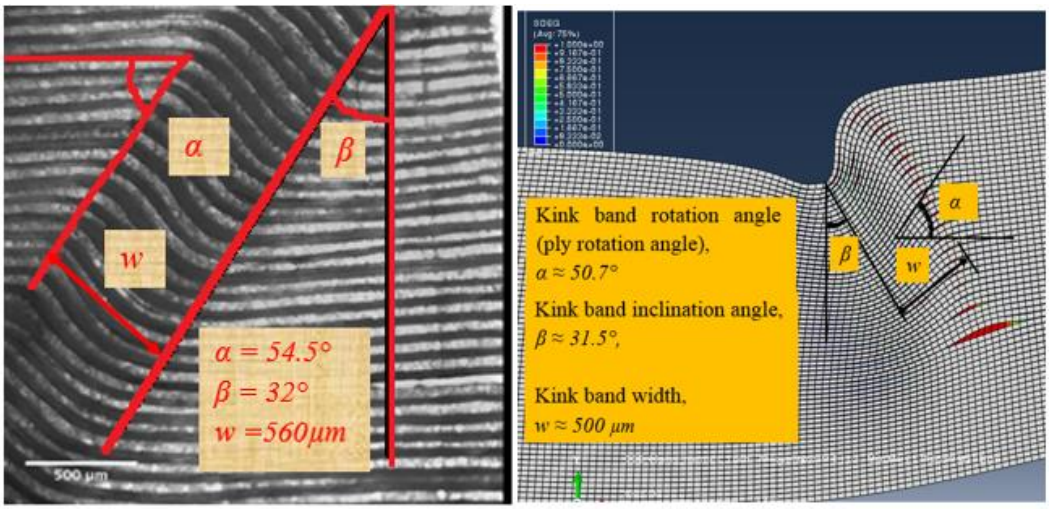

(a) (b)

Figure 86: (a) Kink Band Morphology in a Failed Dyneema HB80 Sample, (b) Kink Band Morphology in a Microbuckling Model of Dyneema HB80, Where, α = Kink Band Rotation Angle (Ply Rotation Angle), β = Kink Band Inclination Angle and w = Kink Band Width

Similar results for Spectra Shield are also shown in figure 87a and 87b. Note that the kink band morphology is similar to the experimental data. But as compared to Dyneema HB80, the Spectra Shield has wider kink bands as it has thicker plies.

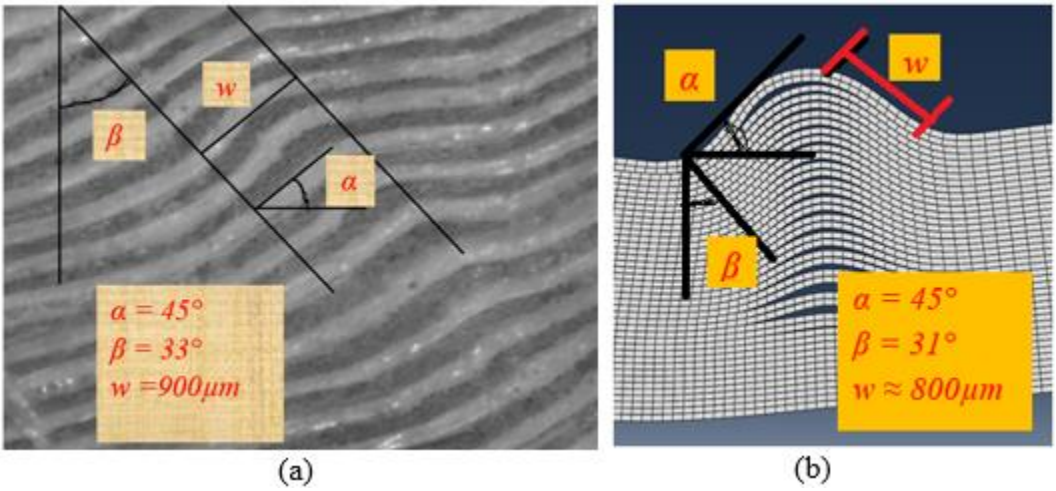

Figure 87: (a) Kink Band Morphology in a Failed Spectra Shield Sample, (b) Kink Band Morphology in a Microbuckling Model of SpectraShield, where, α = Kink Band Rotation Angle (Ply Rotation Angle), β = Kink Band Inclination Angle and w = Kink Band Width.

5.4.5 Comparison between Evaluation of DIC Results and FE Analysis

The DIC results (major principal, normal strains in x and y directions and shear strain across the different sections) indicate that a kink band in both the UHMWPE composites carries a mixture of large normal and shear strains, approximately 33% maximum principal strain during its evolution under bending. It is known from [73] that the DIC method measures the average strain based on the displacements of speckle dots and maps the deformation from deformed to undeformed stages. Therefore, the strain extracted from sample's side surface within the kink band (during its deformation) through

DIC is the overall composite's response rather than a response from a single ply. On the other side, the microstructurally explicit microbuckling model captures the buckling events at the ply level and hence the strains inside the kink band upon the buckling events may not be compared directly with DIC results. However, the deformation gradient [F], extracted through all nodal displacements at the kink band sides may give a means for comparison of the deformation inside the kink band bewteen model and experiment. An alternative way to make a meaningful comparison with DIC results is to extract the displacement jumps across the kink band to understand the bending and sliding nature of interfaces within the kink band during its evolution. The displacement jumps across the kink band are shown in figure 88 for Dyneema HB80.

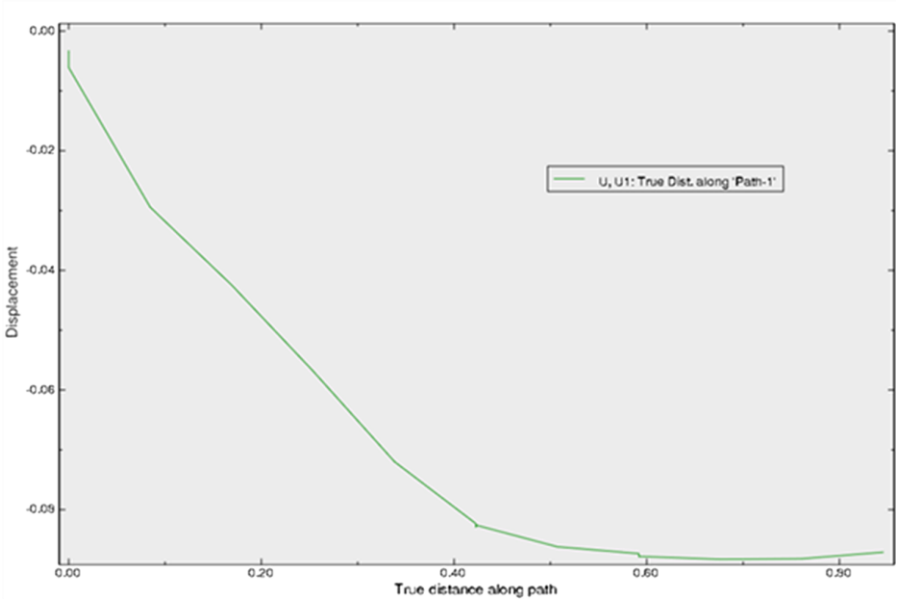

(a)

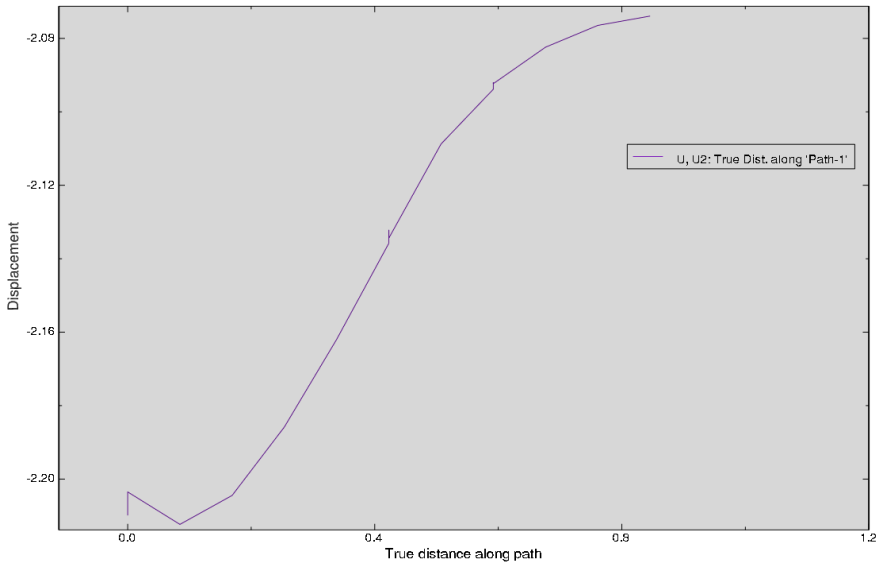

(b)

Figure 88: (a) Displacement Jump – x Direction (b) y-Direction

Note that, the trend of the displacement jumps in x and y directions from microbuckling model are similar to the results obtained in DIC. The displacement in y-direction increases as the sample displaces with further bending and the displacement jumps in x-direction corresponds to shear component. The similar trend has been observed in both microbuckling models (Dyneema and Spectrashield).

Comparison of Radius of Curvature in Kink Band Morphology Between Experiments and FEMs

The radius of curvature was measured macroscopically through Image J software on the deformed beam sample of Dyneema HB80. An example of a trace of kink band curvature created in Image J is shown in figure 89.

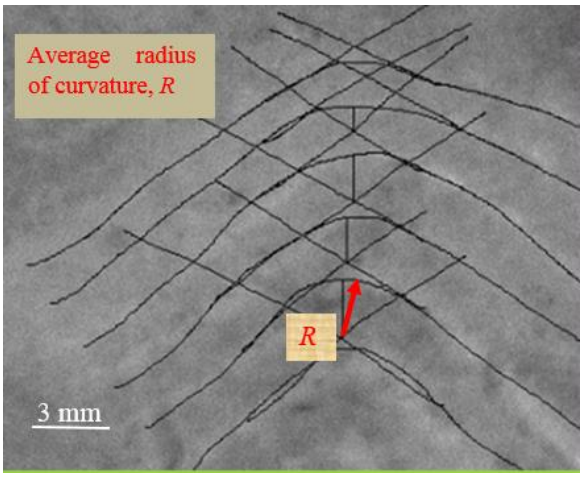

Figure 89: Calculation of Radius of Curvature from Image J Software.

Note that, how the center of the curvature has been identified and the curvature is measured through each point and taken as an average of all. Results are shown in Table 8.

Table 8: Measurement of Radius of Curvature, Macrosopic and FEM

Method of Measurement	Radius of curvature of kink band (microns)
Macroscopic (on sample surface) with ImageJ	210-220 or 0.21 - 0.22 mm
FEM – Mathematical Approach	190-220 or 0.19 – 0.23 mm

The radius of curvature of the kink band was measured using the Equation 4.5 mentioned in the methodology section. Once the curvature is determined, the normal strain within the band can be estimated by $\varepsilon_{xx} = -y/\rho$.

5.5 Paramatric Study of Microbuckling Models

The aforementioned simulations give insight about the physical mechanisms in both the UHMWPE composites that were observed during the flexure tests. In additon to reproduce the global response and corresponding micro-mechanisms, additonal simulations have been analyzed to study the parameters that influence the kink band morphology.

The study was carried out for two different models with 33 and 66 plies respectively, in the same beam height. The primary aspect of this study is to identify the sensitivity response in microbuckling model. Therefore, the same calibrated mechanical properties of 0° and 90° plies, but with different interfacial properties (other than calibrated) from Dyneema HB80 material card (Tables 4 & 5) have been considered. Figure 90a below shows the kink band morphology for 33 plies that has a weak interface and figure 90b shows the 33 plies with strong interface.

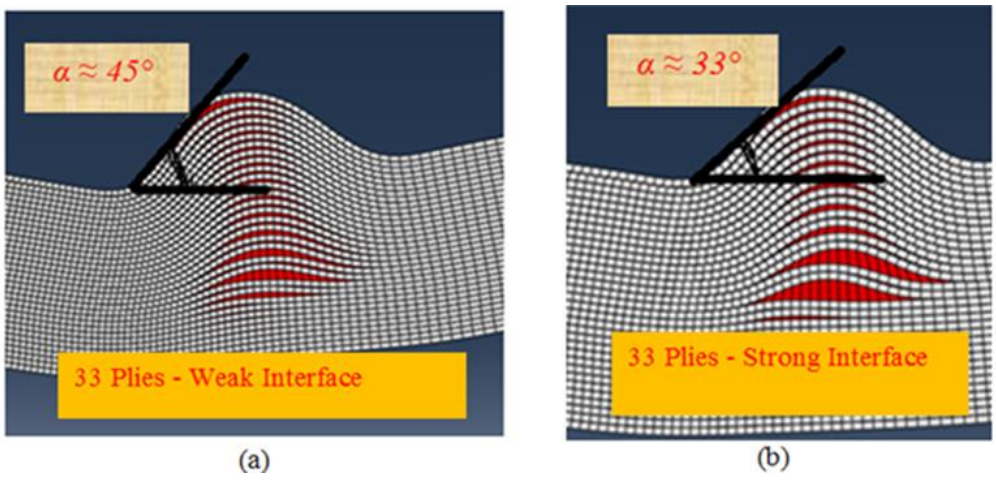

Figure 90: (a) 33 Plies with Weak Interface (b) 33 Plies with Strong Interface (Dyneema HB80).

The weak interface corresponds to the values of G_{Ic} = 1 N/mm and G_{IIc} = 0.03 N/mm and the strong interface corresponds to the values of G_{Ic} = 3 N/mm and G_{IIc} = 0.1 N/mm. Note that, the weak interface induces relatively more inclined bands (see figure 90a) as the fracture energy to separate the plies under shear is low. In other words, the plies slide past each other with a low driving force that separates them. Moreover, the microbuckled plies in the stronger model have not propagated fully as compared to the model with a weak interface. The red region in both the model shows the local delamination between the plies. Note that, the opening of delaminated area in 90b is larger than 90a. This indicates that the separation in opening (Mode I) requires relatively high fracture energy as compared to the model with weak interface. This can offer more bending and shear resistance and hence a rise in load-displacement curve. On the other side, the composite with a low opening and shear properties of interface leads to form a kink band with much lower peak load as compared to the stiffer beam. In a nutshell, the composite with strong interface and stiffer plies can behave like a beam with more displacement and hence gives a rise to the first peak load. This particular case may produce bigger and sparse load-oscillations, which is the case of Dyneema HB80.

With respect to the parameter of imperfection angle ϕ, the microbuckling response is relatively sensitive in terms of global response. For example, increasing ϕ = 3° to 5° in the same 33 ply model with a strong interface increases the first peak load by 15%, where the kink band nucleation begins. Figure 91 shows the microbuckling response for two different imperfection angles. This behavior is due to the shear and bending resistance offered by more inclined interfaces within the imperfection region. The critical force

required to separate the plies increases by increasing the imperfection angle from 3° to 5°. The test cases for imperfection angles 3° and 5° have been chosen such that it follows the misalignment angles observed in micrographs of Dyneema HB80.

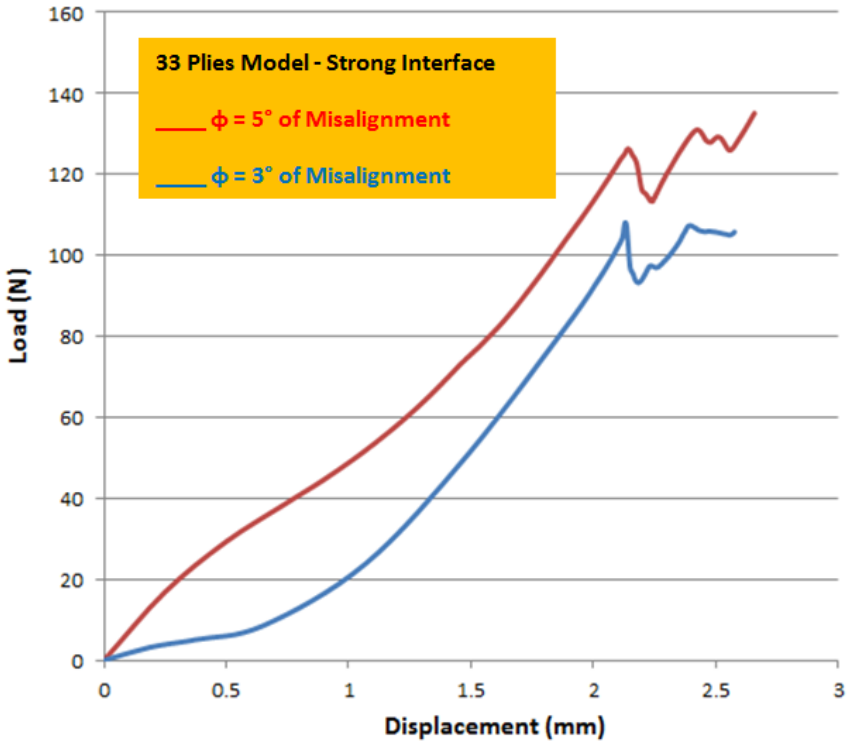

Figure 91: Load Displacement Curves for Two Different Imperfection Angles within the Imperfection Region λ.

In addition to study the effect of imperfection angle on microbuckling response, the effect of the length of the imperfection region, λ, has also been studied, such that $\lambda = 2h$ or $\lambda = h$, where h is the height of the beam. It has been noticed that the microbuckling response is insensitive to the area of the imperfection region. In both the cases, the kink band has been formed and propagated within the imperfection region without any change in the global response.

In addition to the 33 plies model, the comparison has been done between 42 plies and 66 plies to examine the behavior of kink band morphology. This particular comparison sheds light on kink band width and the radius of curvature of the band with increasing the number of the plies in the same beam height. It has been analyzed that the model with 42 plies induces two wedge shaped diffused and wider kink bands starting from the tip (compression side) of the beam. On the other side, the 66 plies model induces only one, but relatively narrower kink band as compared to the 42 ply model. This difference is a direct function of ply thickness. The thicker plies have considerably higher inertia as compared to thin plies. Therefore, the rotation of the plies during microbuckling is relatively smaller vs. that of thin plies. This also tends to form a shallow curvature in the kink band as the beam with thicker plies offer more resistance to bending.

Figure 92 shows different morphologies of kink bands in the models consisting of 42 and 66 plies respectively. Note that the width of the kink band, *w*, is localized in 7 to 9 elements for the 66 ply case vs. 14 to 18 elements for 42 plies. All these measurements have been taken before the onset development of delamination induced by plastic microbuckling. Both models have uniform mesh size of 0.05 mm within the kink band region. Strain relieving mechanisms are likely responsible for the formation of multiple kink bands in the 42 ply case, i.e., only one principal/parent band is not capable enough to carry such the strains required. Consequently, it induces multiple kink bands. This way it does not interact with delamination in earlier stages. The global delamination is interacted when the beam loses its complete bending stiffness.

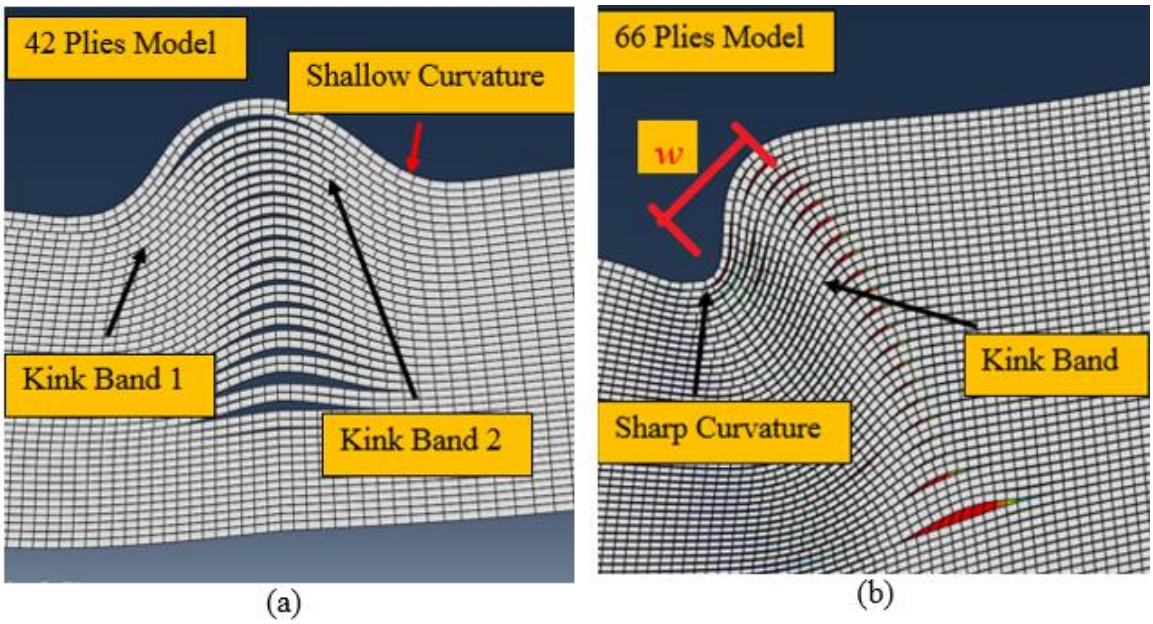

Figure 92: (a) Kink Band Morphology with 42 Plies (Spectrashield) (b) Kink Band Morphology with 66 plies (Dyneema HB80).

As a part of summary on the parametric study, figured 93 and 94 give insight on the kink band morphology with increasing number of plies.

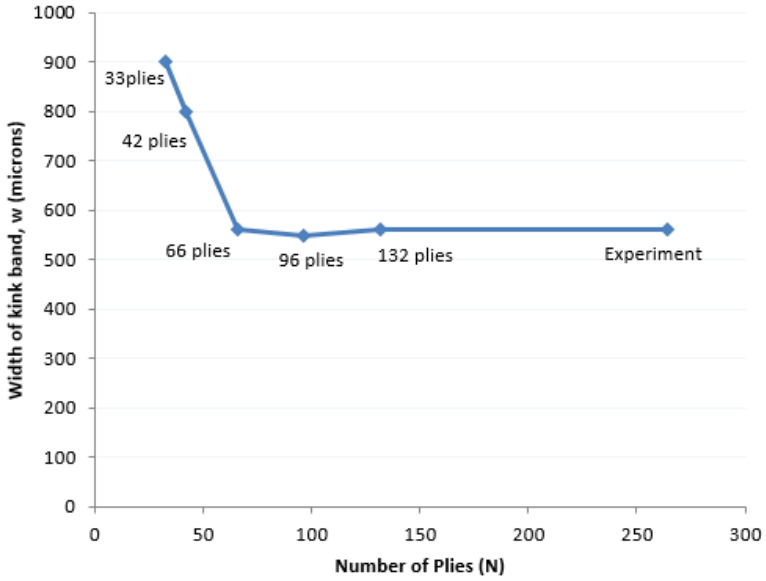

Figure 93: Kink Band Width (w) vs. Number of Plies (N) in Same Beam Height, h

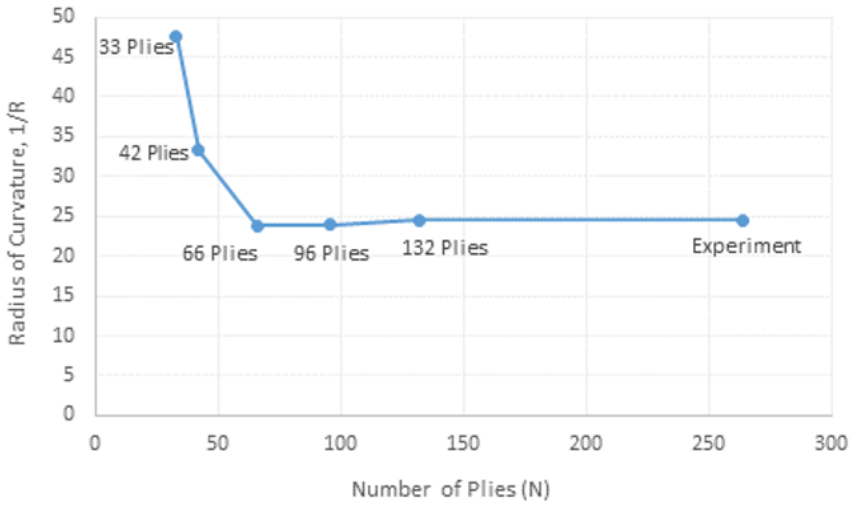

Figure 94: Radius of Curvature vs. Number of Plies

Figure 93 shows that the width of the kink band decreases with increasing number of plies and the figure 94 shows that the radius of curvature/sharpness of the kink band is a direct function of the beam bending. The sharpness increases and hence the 1/R decreases with increasing number of plies, provided that the aspect ratio of L/h=16 has been followed in all the simulations with the same beam height. Both the curves shed light on prediction of response closer to the experimental data. For example, in both figures, the model with 132 plies starts converging (leads to flat curve) to the experimental data. All these measurements have been taken before the onset development of delamination induced by plastic microbuckling.

5.6 Modeling Challenges and Predictions

All the present models capture the physics of different micro-mechanisms involved during the load-oscillations as they were observed in the experiments. The parametric study has elucidated the details about the parameters that influence the kink band morphology. Note that the microbuckling models capture the load oscillations but not to the same extent as the experimental curve. Therefore, to get closer to the experimental data, a microbuckling model requires a beam section with more height, with keeping the same aspect ratio and 264 plies of 40 microns ply thickness to meet the length scale for Dyneema HB80 and 152 plies of 70 microns ply thickness in the case of Spectra Shield that can offer high bending resistance. The implementation of this strategy in microbuckling model should commensurate the similar global response and duplication of the deformation/failure mechanisms that were observed in the experiments. An example of the model with 200 plies in the same beam height used for the calibrated model is shown in the figure 95.

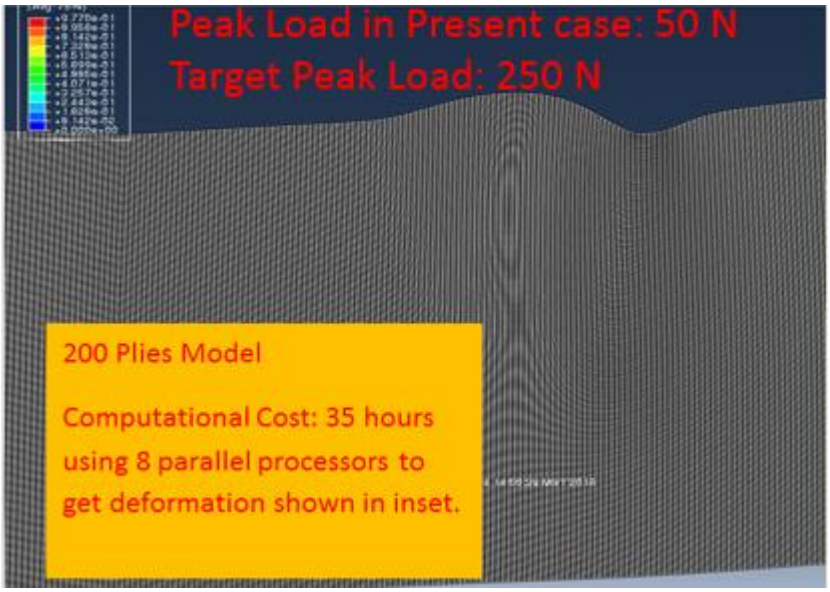

Figure 95: 200 Ply Model to Predict the Microbuckling Response in Dyneema HB80.

The aforementioned consideration gives a length scale of approximately of 5 microns ply thickness, a well below the 40 microns that has been confirmed from optical microscopy in case of Dyneema HB80. So, even with an input of the same calibrated mechanical properties in table 4 and 5 for Dyneema HB80 does not allow the microbuckling response, in particular the first peak load closer to the experimental data. This motivates to increase the beam height with a same aspect ratio (L/h = 16) and incorporating more number of plies. However, implementation of such FEMs would require more elements and hence more computational time. The model shown in figure 95 that has a weak interface (G_{IIc} = 0.003 KJ/$m^{2)}$ tries to capture the bulge (only a certain portion) similar to the experiments, but it has taken 35 hours using 8 parallel processors on a Linux computer. This run was a test case to see how much computational power it requires to converge the certain portion of experimental data. But, the peak load upon the

first buckling event was noticed as 50 N due to an input of very weak interface properties. The peak load is one fifth of that was observed for Dyneema HB80 as shown in figure 96.

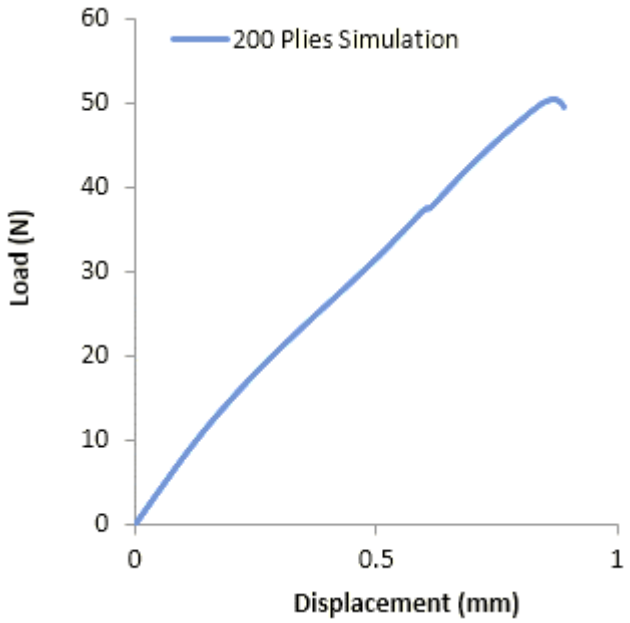

Figure 96: Load vs. Displacement Curve for 200 Plies Model (Test Case).

The replication of the global response close to experiments in both the UHMWPE composites is possible even with the aforementioned modeling challenge and more particularly the simulation costs. Running the models for longer time would possibly fit the experimental data or get closer to it by an input of calibrated properties as mentioned respectively in tables 4 to 7 for both the composites.

6. CONCLUSIONS

Load-displacement curves collected in-situ during loading and through microbuckling models, supports (indirect evidence) the hypothesis of the presence of kink bands triggered by plastic microbuckling. The DIC results indicate that the bands in both the UHMWPE composites nucleate at the compression side and propagate into the sample carrying a mixture of large shear and normal strains, while also decreasing its bending stiffness. Note, that the strains in all stages increases as the band evolves with further beam displacement. This is because with further bending, the plies rotate (ply rotation angle dominates) cooperatively near the vicinity of the load point application and forms sharp bulge that results in more localization of strains within the same section. With progressive buckling of plies, at the end, the overall failure in both Dyneema HB80 and SpectraShield was produced by a combination of plastic microbuckling and axial splitting.

The microstructure of the kink bands in both the samples provides direct evidence of microbuckled plies (plastic microbuckling). There is a noticeable difference in the kink band morphology of Dyneema HB80 and Spectra Shield. Dyneema HB80 has a kink band with a width of approximately 560 μm, whereas the SpectraShield has a kink band width of approximately 900 μm. This also supports the hypothesis of their difference in microstructure and the corresponding influence on the microbuckling response. Note that, the kink band in the case of microbuckling model of Spectra Shield is thicker and more diffused as compared to the kink band in the microbuckling model of Dyneema HB80. This behavior is also a function of the thickness of the plies for the two different materials. Dyneema HB80, with thinner plies, has low inertia as compared to SpectraShield. So, upon

the series of buckling events, the thicker plies do not localize (bend and rotate) in a similar trend to form the kink band(s) as it is in the case of Dyneema HB80. Many of the spectra shield samples in actual experiments showed multiple kink bands, nucleated from the tip similar to as it has been observed and analyzed in its microbuckling model.

A study on length scale of the kink bands as related to microstructure has been performed using a microstructurally explicit finite element model (FEM) to examine microbuckling behavior during kink band evolution, using cohesive zone elements to represent the interfaces between plies. The explanation behind the load-oscillations (global response) supports the formulated hypothesis, based on the experimental observations. The microbuckling model is capable enough to reproduce the physical mechanisms that nucleate the kink bands and their interaction with global delamination. Looking in to the sequential events, at the first peak load, near to the transition of slope change, the first buckling event occurs due to the highly localized stresses near the vicinity of the point of load application that has been applied in terms of displacement boundary conditions. Upon the first buckling event, a set of two plies (a 0° ply and the next to it, which is 90° ply), losses their load bearing capacity, which directly reduces the inertia of the cross-section and results in the first load drop. The process of these buckling events continues and forms a bulge at the tip. The kink band continues to evolve until it induces the delamination failure. This is due to reduction in effective cross section that offers bending resistance. At this particular stage, the progressive buckling of plies culminates and triggers delamination failure. The delamination process is analogous to delamination failure around the hole when subjected to compression [82].

The modeling results show that the band morphology is sensitive to the shear and opening properties of the interfaces between the plies. It has been observed from the parametric study that the weak interface induces relatively more inclined bands as the fracture energy to separate the plies under shear is low. In other words, the plies slide past each other with a low driving force that separates them. Moreover, the microbuckled plies in the model with a strong interface have not propagated fully as compared to the model with a weak interface. This indicates that the separation in opening (mode I) requires relatively high fracture energy as compared to the model with weak interface. This can offer more bending and shear resistance and hence a rise in load-displacement curve. On the other side, the composite with a low opening and shear properties of interface leads to form a kink band with much lower peak load as compared to the stiffer beam. In a nutshell, the composite with strong interface and stiffer plies can behave like a beam with more displacement and hence gives a rise to the first peak load. This particular case may produce bigger and sparse load-oscillations, which is the case of Dyneema HB80.The width of the kink band and the radius of curvature is also a function of the number of plies in the beam with a same height. Both the width and radius of curvature decreases with some extent with increasing number of plies. With a further increase in number of plies in the same height, both the curves starts converging to the experimental data. The analogy of behavior of thin and thick plies in terms of their corresponding inertia against bending and rotation explained earlier in microbuckling models, is also applicable here in case of width of the band and radius of curvature. In case of thin plies, it offers less resistance in forming the

bending curvature and that results in sharp curvature and hence narrower kink band width as compared to thicker plies.

Future Work:

The present work has elucidated the details about kink band evolution under stress gradients in PMCs. During evolution of the kink bands in both the UHMWPE composites, there were multiple kink bands induced as a part of strain relieving mechanism. The understanding of physics behind the formation of multiple kink bands in other directions opens up a new opportunity as a future work.

Moreover, the current FEA models do capture the physics behind the load-oscillations, however the load-deflection curves do not match quite well as they have been observed in the flexure tests. Therefore, it motivates to make more refinement in FEMs by making fully microstructurally explicit models that meets the length scale of the ply level and allows reproducing the exact (closer) global response observed in experiments.

The present study has been carried out in a quasi-static loading conditions. It can be extended to dynamic loading and hence consideration of high strain rates. This will be helpful in full understanding of dynamic behavior of PMCs under high strain rates by developing rate dependent constitutive models.

REFERENCES

[1] Sohi, M. M., H. T. Hahn and J. G. Williams, The Effect of Resin Toughness and Modulus on Compressive Failure Modes of Quasi-Isotropic Graphite/Epoxy Laminates, in Toughened Composites, ASTM STP 937, N. J. Johnston, ed., Philadelphia, PA: American Society for Testing and Materials, pp. 37-60, 1987.

[2] Soutis, C, Measurements of the Static Compressive Strength of Carbon Fiber-Epoxy Laminates, Comp. Sci. Tech., Vol. 42, No. 4, pp. 373-392, 1991.

[3] Waas, A. M., and Schultheisz, C. R., Compressive failure in Composites, Part II, Progress in Aerospace Science, Vol.32, pg. 43-78, 1995.

[4] N.A.Fleck, Compressive failure of fiber composites, Advances in Applied Mechanics, Vol. 33, 1997.

[5] Budiansky, B., and N. A. Fleck, Compressive failure of fiber composites, Journal of the Mechanics and Physics of Solids, 41 (1), 183–211, 1993.

[6] Sun, C. T., and A. W. Jun, Compressive strength of unidirectional fiber composites with matrix non-linearity, Composites Science and Technology, 52(4), 577– 587, 1994.

[7] Schapery, R. A., Prediction of compressive strength and kink bands in composites using a work potential, International Journal of Solids and Structures, 32 (6-7), 739–765, 1995.

[8] Kyriakides, S., R. Arseculeratne, E. J. Perry, and K. M. Liechti, On the compressive failure of fiber-reinforced composites, International Journal of Solids and Structures, 32(6-7), 689– 738, 1995.

[9] Swanson, S. R., A Micro-Mechanics Model for In-Situ Compression Strength of Fiber Composite Laminates. Journal of Engineering Materials and Technology-Transactions of the ASME 114 (1), 8-12, 1992.

[10] Drapier, S., Grandidier, J.C. and Poitier-Ferry, M., A nonlinear numerical approach to the analysis of microbuckling. Composites Science and Technology, 58, 785–790, 1998.

[11] Narayan, S. & Schadler, L., Mechanisms of kink band formation in graphite epoxy composites: a micromechanical experimental study, Volume 59, Issue 15, November 1999, pp. 2201-2213.

[12] Evans, A. G., Adler, W. F., Kinking as a Mode of Structural Degradation in Carbon Fiber Composites. Acta Metallurgica 26, 725-738, 1978.

[13] Chatterjee, S. N. and McLaughlin, P. V. Inelastic shear instability in composite materials under compression. Proc. 3rd AXE Engng Mech. Div. Specialty Conf. Sept. 17-19, pp. 6499652. University of Texas at Austin, 1979.

[14] A.S. Argon, Fracture of composites, Treatise on Materials Science and Technology, Academy Press, New York 1972.

[15] B.W. Rosen, Mechanics of composite strengthening, Fibre Composite Materials, American Society of Materials, Metals Park, Ohio (1965).

[16] Jelf, P. M., Fleck, N. A., Compression Failure Mechanisms in Unidirectional Composites. Journal of Composite Materials 26 (18), 2706-2726, 1992.

[17] Chaplin, R. C., Compressive Fracture in Unidirectional Glass-reinforced Plastics. Journal of Materials Science 12, 347-352, 1977.

[18] Wilkinson, E., Parry, T. V., & Wronski, A. S., Comp Sci Tech 26, 17-29, 1986.

[19] P.S.Steif, A model for kinking in fiber composites - I. Fiber breakage via micro-buckling. International Journal of Solids and Structures, Vol. 26 (1990).

[20] Moran P.M., Liu X.H., Shih C.F., Kink band formation and band broadening in fibre composites under compressive loading. Acta Met. Et Mater. 43 (8), 2943–2958, 1995.

[21] Davila, C. G., Jaunky, N., Goswami, S., Failure criteria for FRP laminates in plane stress. 44th SDM Conference, AIAA, Norfolk, 2003.

[22] T.J.Vogler, S.Kyriakides, On the initiation and growth of kink bands in fiber composites. Part I: experiments. International Journal of Solids and Structures 38, 2001.

[23] Vogler, T. J., Kyriakides, S., On the Axial Propagation of Kink Bands in Fiber Composites: Part I Experiments. International Journal of Solids and Structures 36, 557-574, 1999.

[24] Hahn, T. H., Williams, J. G., 1986. Compression Failure Mechanisms in Unidirectional Composites. Composite Materials: Testing and Damage (7th Conf.) ASTM STP 893, 115139.

[25] Pimenta, S., R. Gutkin, S. T. Pinho, and P. Robinson, A micromechanical model for kinkband formation: Part i experimental study and numerical modeling, Composites Science and Technology, 69, 948–955, 2009a.

[26] Pimenta, S., R. Gutkin, S. T. Pinho, and P. Robinson, A micromechanical model for kinkband formation: Part ii analytical modeling, Composites Science and Technology, 69, 956– 964, 2009b.

[27] G Liu, M D Thouless, V S Deshpande and N A Fleck, Collapse of a composite beam made from ultra-high molecular-weight polyethylene fibres, Master's Thesis, Cambridge University, 2013.

[28] Prabhakar, P., Failure mode interaction in fiber reinforced laminated composites, Doctorate Thesis, The University of Michigan, 2013.

[29] M. Alfano, F. Furgiuele, A. Leonardi, C. Maletta and G. H. Paulino, Cohesive Zone Modeling of Mode I Fracture in Adhesive Bonded Joints, Key Engineering Materials Vols. 348-349, pp. 13-16, 2007.

[30] Sutcliffe M.P.F. and Fleck, N.A., Microbuckle Propagation in Carbon Fibre-Epoxy Composites, Acta metal. Mater., vol. 42, No. 7, pp. 2219-2231, 1994.

[31] Bower, A. F., Applied Mechanics of Solids, 2012.

[32] Mase Thomas, Mase G., Continuum Mechanics for Engineers, 2nd Edition, CRC Press, ISBN 0-8493-1855-6.

[33] S.S Morye, P.J Hine, R.A Duckett, D.J Carr, I.M Ward, Modeling of the energy absorption by polymer composites upon ballistic impact, Composites Science and Technology, Volume 60, Issue 14, November 2000, Pages 2631-2642, ISSN 0266-3538.

[34] Greszczuk, L.B., Prediction of Transverse Strength and Scatter in Test Data for Unidirectional Composites, American Society for Testing and Materials, pp. 311-316, 1974.

[35] Greszczuk, L.B., On failure Modes of Unidirectional Composites under Compressive Loading, Symposium on Fracture of Composite Materials, G.C. Shih and U. P. Tamuze, eds., Boston, MA: Martimus Nijhoff Publishers, pp. 231-244, 1982.

[36] S.S Morye, P.J Hine, R.A Duckett, D.J Carr, I.M Ward, Modeling of the energy absorption by polymer composites upon ballistic impact, Composites Science and Technology, Volume 60, Issue 14, November 2000, Pages 2631-2642, ISSN 0266-3538.

[37] Landro, L.D. and M. Pegoraro, Carbon Fibre-thermoplastic Matrix Adhesion, Journal of Material Science, 22:1980-1986.

[38] Greszczuk, L.B., Interfiber Stresses in Filamentary Composites, AIAA Journal, 9:1274-1280, 1971.

[39] Kurashige, M., Compressive Strength of a Laminated Fiber-Reinforced Material, Bulletin of Japanese Society of Mechanical Engineering, Volume 27, pp. 2694-2697, 1984.

[40] Chang, F.K. and L. Lessard, Effect of Load Distribution of the Fiber Buckling Strength of Unidirectional Composites, Journal of Composite Materials.

[41] Lefebvre, A. H., Atomization and Sprays, Chapter 6, 1989.

[42] C. Wang, C. T. Sun and T. S. Gates, Elastic/Viscoplastic Behavior of Fiber-Reinforced Thermoplastic Composites, Journal of Reinforced Plastics and Composites 1996 15: 360.

[43] Guedes RM, de Moura MFSF, Ferreira FJ. Failure analysis of quasi-isotropic CFRP laminates under high strain rate compression loading. Compos Struct 2008; 84(4): 362–8.

[44] Dugdale, D., *Yielding of steel sheets containing slits.* Journal of the Mechanics and Physics of Solids, 1960. **8**: p. 100-104.

[45] Barenblatt, G., *The mathematical theory of equilibrium cracks in brittle fracture.* Advances in Applied Mechanics, 1962. **7**: p. 55-129.

[46] Wisnom, M.R., Size effects in the testing of fiber-composite materials, Composite Science Technology, 1999, pp. 1937–1957

[47] Hsu, S. Y, Vogler, T.T, Kyriakides, S. , Inelastic behavior of an AS4/PEEK composite under combined transverse compression and shear.Part II: modeling, International Journal of Plasticity, 1999, Volume 5, Issue 8, p. 807-836.

[48] ASTM D7264/D7264M - 07: "Standard Test Methods for Flexural Properties of Polymer Matrix Composite Materials."

[49] ASTM Standard 6671A:"Standard Test Methods for Mode-1 Inter-laminar fracture toughness of Polymer Matrix Composite Materials."

[50] Russell, B.P., Karthikeyan, K., Deshpande, V.S., Fleck, N.A., 2013. The high strain rate response of ultra-high molecular-weight polyethylene: from fibre to laminate. Int. J. Impact Eng. 60, 1–9.

[51] Smith, P., Lemstra, P.J., 1980. Ultra-high-strength polyethylene filaments by solution spinning/drawing. J. Mater. Sci. 15, 505–514.

[52] Smith, P., Lemstra, P.J., Kalb, B., Pennings, A.J., 1979. Ultra-high-strength polyethylene filaments by solution spinning and hot drawing. Polym. Bull. 1,733–736.

[53] J.P. Attwood , S.N. Khaderi K. Karthikeyan N.A. Fleck, M.R. O'Masta H.N.G.Wadley , V.S. Deshpande, The out-of-plane compressive response of Dyneema composites, Journal of Mechanics and Physics of Solids 70 (2014), 200-226.

[54] C.G. Dávila, P.P. Camanho, and C.A. Rose. Failure criteria for FRP laminates. Journal of Composite Materials, 39(4):323, 2005.

[55] S.T. Pinho, C.G. Dávila, P.P. Camanho, L. Iannucci, and P. Robinson. Failure models and criteria for FRP under in-plane or three-dimensional stress states including shear nonlinearity. NASA Technical Memorandum, 213530, 2005.

[56] S.T. Pinho, R. Darvizeh, P. Robinson, C. Schuecker, and P.P. Camanho. Material and structural response of polymer-matrix fibre-reinforced composites. Composites Science and Technology, Accepted for publication :(Special issue on Second World Wide Failure Exercise), 2008.

[57] J.L. Chaboche, S. Kruch, J.F. Maire, and T. Pottier. Towards a micromechanics based inelastic and damage modeling of composites. International Journal of Plasticity, 17(4):411– 439, 2001.

[58] M.L. Boubakar, L. Vang, F. Trivaudey, and D. Perreux. A meso-macro finite element modelling of laminate structures: Part ii: time-dependent behavior. Composite structures, 60(3):275–305, 2003.

[59] G.M. Vyasa, S.T. Pinhoa, P. Robinson, Constitutive modelling of fibre-reinforced composites with unidirectional plies using a plasticity-based approach, 2011.

[60] Ever J. Barbero, Finite Element Analysis of Composites Materials using ABAQUS^{TM}, CRC Press, 2013.

[61] ASTM D3165 - Standard Test Method for Strength Properties of Adhesives in Shear by Tension Loading of Single-Lap-Joint Laminated Assemblies.

[62] Min Jung Lee, , Tae Min Cho, Won Seock Kim, Byung Chai Lee, Jung Ju Lee, Determination of cohesive parameters for a mixed-mode cohesive zone model, International Journal of and Adhesion and Adhesives, Vol. 30, 5, July 2010, pp. 322-328.

[63] G. Liu, Modelling microbuckling failure of a composite cantilever beam made from ultra-high molecular-weight polyethylene fibres, Acta Mech 226, pp. 1255–1266, 2015.

[64] L. Warnet and R. Akkerman, Classical Lamination Theory, Composites course 2008-2009, University of Twente, Engineering and Technology.

[65] Mallick, P.K., Fiber-Reinforced Composites, Second Edition, 1993.

[66] Reddy, J. N., Mechanics of Laminated Composite Plates, 1997.

[67] B. Agarwal, L. Broutman and K. Chandrashekhara, Analysis and Performance of Fiber Composites, Third Edition, 2006.

[68] Wisnom, M.R., The effect of fibre waviness on the relationship between compressive and flexural strengths of unidirectional composites, Journal of Composite Materials, 28, pp. 66-76, 1994.

[69] Wisnom, M.R. and J.W. Atkinson, Constrained buckling tests show increasing compressive strain to failure with increasing strain gradient, Journal of Composites, 28A, pp. 959-964, 1997.

[70] Wisnom, M.R., The effect of specimen size on flexural strength of unidirectional carbon fibre-epoxy, Composite Structures, 18, pp. 47-63, 1991.

[71] Swanson S.R., Constraint effects in compression failure of fiber composites, Proc. ICCM10, Vol. I, pp. 739–746, 1995.

[72] S. Drapier, C. Gardin, J.C. Grandidier, M. Potier-Ferry, Structure effect and microbuckling**,** Composites Science and Technology, 56, pp. 861–867, 1996.

[73] ARAMIS^{TM} Reference Manual, v6.1.

[74] Pagano, N. J., Interlaminar Response of Composite Materials, Composite Materials Series, Vol. 5, 1989.

[75] ABAQUS reference manual, v6.13

[76] Sun E., Shear locking and hourglassing in MSC Nastran, ABAQUS and ANSYS.

[77] Logan, D. L., A First Course in the Finite Element Method, 2nd edition, 1992.

[78] Lt. Brown, J., Characterization of MSC/NASTRAN & MSC/ABAQUS Elements for Turbine Engine Blade Frequency Analysis, Air Force Research Lab, Turbine Engine Division.

[79] Cook, R. D., Malkus, D., and Plesha, M., Concepts and Applications of Finite Element Analysis, 3rd ed., John Wiley & Sons, 1989.

[80] Simo, J. C., and M. S. Rafai, A Class of Assumed Strain Method and Incompatible Modes, J. Numerical Methods in Engineering, Vol. 29, pp. 1595-1638, 1990.

[81] Wilson, E. L. and A. Ibrahimbegovic, Use of Incompatible Displacement Modes for the Calculation of Element Stiffnesses and Stresses, Finite Elements in Analysis and Design, Vol. 7, pp. 229-241, 1990.

[82] Soutis, C., Fleck, N.A., Curtis, P., Hole –hole Interaction in carbon fiber/epoxy Laminates under Uniaxial Compression, Journal of Composites., January 1991.

[83] Greenhalgh, E., Failure Analysis and Fractography of Polymer Composites, Woodhead Publishing, 2009.

[84] Meyers, M., and Chawla, K., Mechanical Behavior of Materials, 2nd edition, 2008.

[85] Meyers, M., Dynamic Behavior of Materials, 1st edition, 1994.